DESIGN AND ANALYSIS OF A MICROMECHANICAL TUNING FORK GYROSCOPE

by

David W. King

B.S. Mechanical Engineering, Lehigh University
(1987)

SUBMITTED TO THE DEPARTMENT OF AERONAUTICS AND ASTRONAUTICS
IN PARTIAL FULFILLMENT OF THE REQUIREMENTS FOR THE DEGREE OF

MASTER OF SCIENCE IN
AERONAUTICS AND ASTRONAUTICS

at the

© MASSACHUSETTS INSTITUTE OF TECHNOLOGY

May, 1989

Signature of Author _____

Department of Aeronautics and Astronautics
May, 1989

Approved by _____

Burton Boxenhorn
Technical Supervisor, CSDL

Certified by _____

Professor Walter M. Hollister
Thesis Supervisor

Accepted by _____

Professor Harold Y. Wachman
Chairman, Departmental Graduate Committee

i

DESIGN AND ANALYSIS OF A MICROMECHANICAL TUNING FORK GYROSCOPE

by

David W. King

Submitted to the Department of Aeronautics and Astronautics on May 12, 1989 in partial fulfillment of the requirements for the degree of Master of Science in Aeronautics and Astronautics

ABSTRACT

This thesis investigates the feasibility of a micromechanical tuning fork as an angular rate sensor. The gyroscopic effect of a tuning fork, which is caused by the oscillating mass moment of inertia due to the vibrating tines, is described and demonstrated by a simple model. The gyroscopic response to an input rate about the longitudinal axis between the tines is described by a second order, linear periodic (LP) differential equation which is derived by Hamilton's variational method. If the periodic terms in the equation of motion are neglected, the gyroscopic output is shown to be oscillatory in phase with the vibrating tines · and linearly related to the input rate, the system quality factor, and the mechanical gain of the gyroscope. The mechanical gain is the ratio of the oscillating component of the mass moment of inertia about the input axis to the nominal component.

The periodic terms in the equation of motion are not negligable for a lightly damped, high frequency micromechanical system. A sufficient condition for stability of the LP system is derived from the properties of the Mathieu Equation. The stability condition is specified in terms of the product of the system quality factor and the mechanical gain, and it is checked by applying Floquet Theory. The response of the gyroscopically forced LP equation is solved numerically and also estimated by a Fourier Series solution. Both of these solutions correspond with the estimated linear response within the stability region.

Mathematical models are derived for the electrostatic driving force between the two fork tines, the variable capacitance sensing of the gyroscopic rotation, the stiffness properties of the structure, and the air damping torque. In addition, possible error sources are analyzed including cross-axis sensitivity, external forces and vibration, unbalance torques, motor-sensor coupling, amplifier noise, and Brownian Noise. The system mathematical model is implemented into a computer program and a baseline design configuration is obtained which is compatible with micromachining processes. The predicted performance of the baseline design is shown to be competitive with the double gimbal micromechanical gyroscope currently being developed.

Thesis Supervisor: Dr. Walter M. Hollister
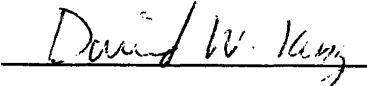Title: Professor of Aeronautics and Astronautics

ACKNOWLEDGEMENTS

TABLE OF CONTENTS

LIST OF SYMBOLS

I_y	principal mass moment of inertia about sensitive axis
I_0	nominal (non-oscillating) component of I_y
I_1	oscillating component of I_y
θ	rotation angle of the fork relative to its base
k_t	linear stiffness coefficient of torsional spring
b_t	linear damping coefficient of torsional system
Ω	applied angular rate about sensitive axis
W_x (Ch.2)	applied angular rate about x-axis
W_z (Ch.2)	applied angular rate about z-axis
ω_d	motor (tines) driving frequency
ω_n	natural frequency of torsional system
ω	system frequency when ω_d is tuned to ω_n
$\underline{\omega}_{bi}$	angular velocity vector of fork base with respect to inertial space
$\underline{\omega}_{fb}$	angular velocity vector of fork with respect to its base
$\underline{\omega}_{fi}$	angular velocity vector of fork with respect to inertial space
I	inertia tensor
I_x	principal mass moment of inertia about x-axis
I_z	principal mass moment of inertia about z-axis
Δ_{Iz}	oscillating component of I_z
$\underline{i}_x, \underline{i}_y, \underline{i}_z$	unit vectors corresponding to fork axes
$\underline{i}_{x'}, \underline{i}_{y'}, \underline{i}_{z'}$	unit vectors corresponding to fork base axes
E	modulus of elasticity for silicon
G	torsional modulus of elasticity for silicon
L (L_t, l)	length of tines (y-dim)
h	height of tines (z-dim)
w	width of tines (x-dim)
l_f, f_y	length of flexures
f_z (2b)	thickness of flexures
f_x (2a)	width of flexures
m_f	mass of each flexure
m_w	mass of each wing
m_p	mass of each inertial proof mass
m_t	mass of each tine

W_x, W_y, W_z	x,y,z dimensions of each wing, respectively
Q	system quality factor
ε	gyroscope mechanical gain
a,q	Mathieu Equation parameters
$a(t)$	second derivative term coefficient to 2nd order LP equation
$b(t)$	first derivative term coefficient to 2nd order LP equation
$c(t)$	first order term coefficient to 2nd order LP equation
$d(t)$	forcing function term for 2nd order LP equation
$G(t)$	system plant matrix
$B(t)$	system forcing matrix
a_n	Fourier sine coefficients
b_n	Fourier cosine coefficients
$\underline{\Phi}$	state transition matrix
x	second order system state vector
F_1	parallel electric flux motor force
F_2	fringing electric flux motor force
F_0	total motor force
ε_0	permittivity constant
d	nominal distance between tines
g	nominal distance between wing and bridge electrode
V_d	differential driving voltage
V_0	voltage with respect to ground applied on each tine
$w(z)$	conformal transformation function
$K(k)$	complete elliptic integral of first kind
$E(k)$	complete elliptic integral of second kind
$sn(x)$	Jacobi's elliptic sine function
r_{0m}	nominal distance between inertial mass center and sensitive axis
r_{0t}	nominal distance between tine center and sensitive axis
x_1	distance from sensitive axis to front edge of sensor plate
x_2	distance from sensitive axis to back edge of sensor plate
C_i	amount of sensor capacitance increase due to rotation
C_d	amount of sensor capacitance decrease due to rotation
C_0	nominal capacitance of each pair of sensor plates
ΔC	net change in capacitance output signal
C_{fb}	output amplifier feedback capacitance
R_{fb}	output amplifier feedback resistance

E_x	sensor excitation voltage
ω_x	sensor excitation frequency
B	bandwidth of output signal filter
e_{out}	output voltage
b_x, b_y, b_z	x,y,z dimensions of strain beam slot, respectively
β	boron-silicon misfit factor
μ_{si}	Poisson's ratio for silicon
σ_0	axial prestress on flexures
U_∞	maximum free stream air velocity normal to wings
μ	viscosity of air flow over wings
Q_f	volumetric flow rate through sensor channel
Q_f'	profile flow rate through sensor channel
F_f	damping force due to flow impingement
F_p	damping force due to pumping effect
x_m	amplitude of tine vibration at tine midpoint
Δz	z-direction misalignment of proof masses
A_B	amplitude of white Brownian Noise
A_a	amplitude of white amplifier noise
$a\ (BW)$	system bandwidth
b	dynamics constant ($I_0\,\omega$)
K_e	electronics constant
K_B	Boltzmann's constant
K_θ	capacitance constant
$\sigma_{ss,B}$	output standard deviation due to Brownian Noise
$\sigma_{ss,a}$	output standard deviation due to amplifier noise
K_1	sensor excitation constant
m_x, m_y, m_z	x,y,z dimensions of each proof mass, respectively
u_2	ratio of tine vibration amplitude to its maximum limit
θ_{quad}	output oscillation amplitude in quadrature due to unbalance

INTRODUCTION

During the past several years, rapid advancements have been made in the fields of integrated circuits and microchip processing. The efficiency and accuracy in which silicon can be etched into tiny structures with dimensions in microns has led scientists to pursue the possibility of producing mechanical elements on the microchip level. Devices such as accelerometers, pressure transducers, flow sensors, force transducers, electrostatic actuators, and miniature microphones have already been developed and are beginning to become commercially available. The advantages of micromechanical elements are obvious. The small size of the devices open up areas of application previously deemed unrealistic. For example, micromechanical sensors are sought after for various biomedical purposes in which conventional sensors are ineffective due to size restrictions. Also, the semiconductor batch processing techniques applied to mechanical structures greatly reduces the cost for mass production. It has now become vital for sophisticated sensors to become available cheaper in order to keep in pace with the rapidly decreasing cost of microprocessors. The two fundamental properties of silicon make it an excellent material for sensing instruments. Its semiconductor electrical properties allow easy integration with system electronics, and its strong mechanical properties allow micromechanical instruments to be safely operated in high impact or acceleration environments.

Following this trend, in 1983 the Charles Stark Draper Laboratory, Inc. initiated the design and development of a novel micromechanical gyroscope. This represented the first development of its kind and led to a full scale project with the final goal being a complete three axis micromechanical inertial guidance system. It has been forecast that the system will be operated in a strapdown mode with on-chip electronics, and only consist of one square inch flatpack. The gyroscope, designed by B. Boxenhorn [1,2] is planar, etched from a silicon wafer, and uses an oscillating angular momentum vector to sense angular rate about the axis normal to the gyro plane. A vibrating outer gimbal, supported by torsional pivots,

vibrates sinusoidally driven by electrostatic torquers. The oscillating angular momentum vector, combined with the angular rate, produces a gyroscopic torque on an inner gimbal causing it to vibrate about the other planar axis at the driving frequency. The inner gimbal has a vertical bar mounted on it to add inertia to the gyroscopic element. The amplitude of the inner gimbal vibration is proportional to the applied angular rate and is sensed by ultrasensitive variable capacitance plates. The driving and sensing of the device is done by fixing electrodes above the gimbals and applying appropriate voltages.

The gyroscope has been extensively modeled, built, and tested. On 1 September 1987, The first ever micromechanical gyroscope was shown to produce gyroscopic action. Since that important milestone rapid improvements have been made on the device including the design of a closed loop rebalance system, improvements in fabrication techniques making possible a monolithic structure with buried electrodes, and analytical models of the noise sources. The most recent test results, operated closed loop, show a gyro sensitivity of 3.13 mV/rad/sec with a noise level equivalent to 2500 degrees per hour. The gyro is projected to achieve angular rate sensing accuracy within 10 degrees per hour upon completion of the development program. At that point the device is expected to be useful in applications such as small projectile guidance, kinetic energy weapon guidance and control, land vehicle guidance and control, flight vehicle structure control and sensor stabilization, and robotics. These applications exploit the micromechanical gyroscope's qualities not present in conventional gyros such as small size, low cost, and ruggedness.

The idea of a vibratory gyroscope is not new. In the 1950's extensive research was performed on vibratory angular rate sensors. The most popular configuration analyzed was that of a tuning fork, where the two fork tines are forced to vibrate aganinst each other to give an oscillating mass moment of inertia about the input axis. This, in turn, produces an oscillating torque about the axis of the fork stem proportional to an applied angular about the same axis. The Sperry Gyroscope Company designed and produced a class of these instruments labeled the "Gyrotron Angular Rate Tachometer" [3]. Sperry envisioned that the

Gyrotron would become a high performance gyro suitable for long range navigation applications. The Gyrotron, they believed, would acquire very high accuracy through continued research on eliminating the zero rate error and further modification of the angular displacement sensing technique. A decade of research continued, but, as seen retrospectively thirty years later, the tuning fork gyro proved unsuccessful and its development was terminated.

However, it has become desirable to investigate the potential of a tuning fork configuration on a micromechanical level, and that is the basis of this thesis. Several factors inspired the study of an alternate configuration micromechanical gyroscope, and they are listed below:

1) An investigation of the feasibility of producing a micromechanical gyroscope with an input axis on the same plane as the gyro. A combination of two of these gyros with the current gyro would enable three gyros on a chip to sense angular rates about all three axes.

2) A thorough analysis of the tuning fork dynamics. The previous analysis of tuning fork gyros neglects the time variant terms that appear in the equations of motion. On a micromechanical level these terms become significant since it is a lightly damped system of high frequency. It is thus necessary to determine the effect of these terms on the gyro response and if they lead to regions of instability and poorly behaved output.

3) A simple but adequate design of a micromechanical tuning fork gyroscope. This would make it possible to determine the performance characteristics of the gyro including its response, mechanical properties, electrical properties, and noise levels.

3

4) A comparison of the open loop performance capabilities between the current configuration and a tuning fork.

5) A conclusion on whether a tuning fork gyro could be successful on a micromechanical level even though all previous development efforts failed.

The thesis begins with a description of the gyroscopic properties of a tuning fork and the micromechanical gyro model to be studied. The equations of motion for the instrument are then determined rigorously by Hamilton's variational methods. This approach to the dynamics has not been attempted in the literature and will give greater insight into the system and the various small order terms neglected in the literature [3,4,5]. The next section of the thesis analyzes the full equations of motion. Due to the time variant terms in the equations no closed form solution is possible, and approximation methods are used. First, the homogeneous equation is transformed into Mathieu's Equation which makes it possible to approximate the system stability characteristics. The approximated stability region is then checked by Floquet theory. An approximate infinite series harmonic solution is obtained for the forced equation of motion to evaluate the various harmonic components as a function of the system parameters. The approximate system responses are reinforced by a thorough numerical simulation of the system. The last part of the paper gives design parameters of a micromechanical tuning fork gyro and calculates a set of perfomance characteristics based on a thorough mathematical model of the system. The design is done such that the device can be built using microfabrication techniques, the response is open loop stable with maximized sensitivity, and the identified noise levels are kept to a minimum. The thesis ends by drawing conclusions on the feasibility of a micromechanical tuning fork gyroscope as an angular rate sensor.

1 GYROSCOPE DESCRIPTION AND SYSTEM MODEL

1.1 Tuning Fork Gyroscopic Effect

The operating principles of the tuning fork gyroscope are straight forward. It is possible to explain the gyroscopic torque of the device using Newton's laws, a freshman physics background, and referring to the generic schematic of a tuning fork given in Figure 1.1. This description of the gyroscope is not adequate for analytical purposes, but it should give the reader a clear understanding of the operating principles.

The two fork tines are forced to vibrate 180 degrees out of phase with each other at the same frequency, ω_d. The vibration causes the structure to have an oscillating mass moment of inertia about the y-axis, which is the fork axis of symmetry and will hereafter be labeled the *sensitive axis*. The principal inertia about this axis can then be written as the sum of a constant term and an oscillating term,

$$I_y = I_0 + I_1 \sin \omega t. \tag{1.1-1}$$

In addition to the forced tine vibration, assume that the tuning fork has only one degree of freedom which is rotation about the torsional fork stem. The stem acts like a linear torsional spring with stiffness k_t. Further assume that the system is damped linearly, and let the damping coefficient be labeled b_t. The spring and damping act as restraining torques such that

$$\Sigma T_y = -k_t \theta - b_t \dot{\theta}. \tag{1.1-2}$$

Let the base of the fork be fixed to a specific object which is being rotated with respect to an inertial reference frame, such that the component of the rotation vector along the fork sensitive axis is denoted by Ω. From Newton's laws the sum of the torques about the sensitive axis equals the time rate of change of the angular momentum component such that

$$\Sigma T_y = \frac{d}{dt}(H_y) \Rightarrow$$

$$-k_t \theta - b_t \dot{\theta} = \frac{d}{dt}[(I_0 + I_1 \sin \omega_d t)(\theta + \Omega)] \tag{1.1-3}$$

5

Differentiating the right hand side and neglecting the Ω terms, the fork equation of motion becomes

$$(1 + \frac{I_1}{I_0}\sin \omega_d t)\,\ddot{\theta} + (\frac{b_t}{I_0} + \frac{I_1\omega_d}{I_0}\cos \omega_d t)\,\dot{\theta} + \omega_n^2\,\theta \;=\; \frac{-I_1\omega_d}{I_0}\Omega \cos \omega_d t \qquad (1.1\text{-}4)$$

where ω_n is the torsional natural frequency of the fork,
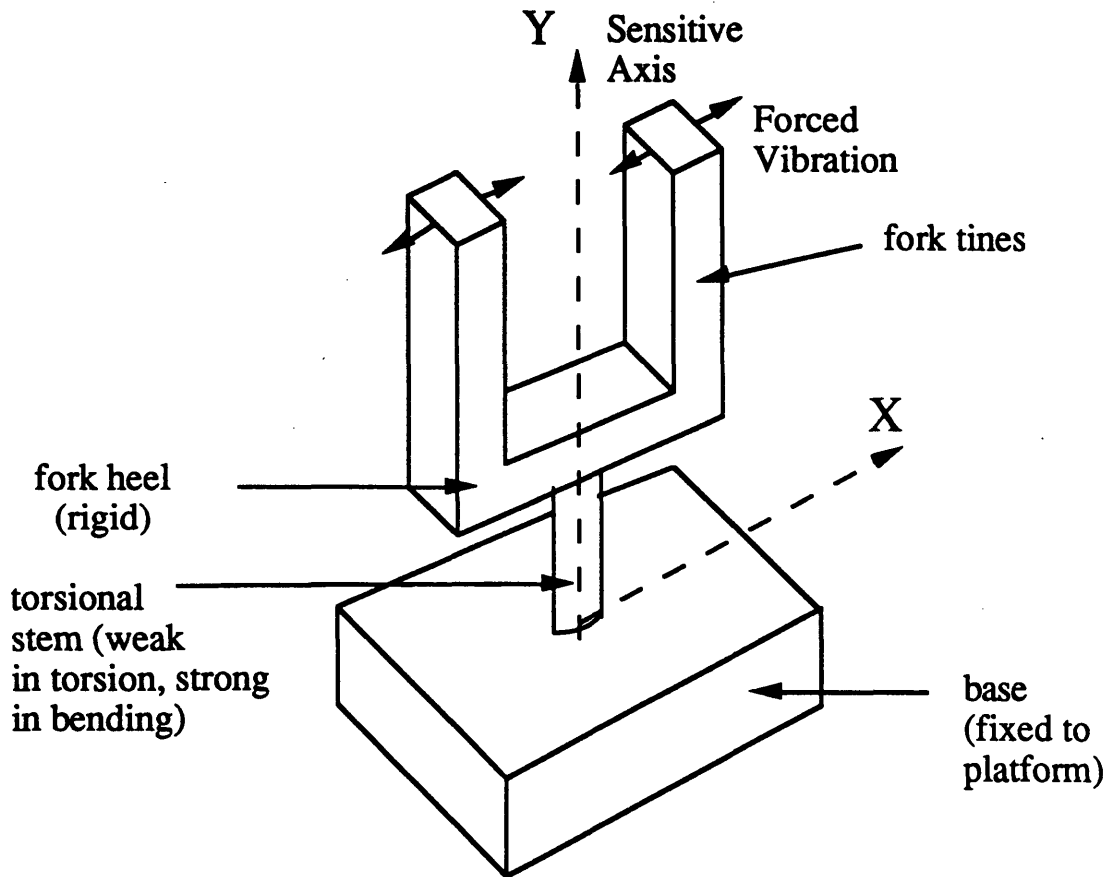
$$\omega_n^2 = \frac{k_t}{I_0}$$

Figure 1.1   Tuning Fork Schematic

A rigorous derivation that includes an analysis of the neglected terms of Equation (1.1-4) is the basis of Chapter 2. However, this simple derivation gives insight into the physics of the tuning fork gyroscope. For instance, it is clear that the gyroscopic torque term, $\frac{I_1\omega_d}{I_0}\Omega$,

6

comes from the oscillating angular momentum about the sensitive axis and is proportional to the magnitude of the angular rate component about the sensitive axis. It is also evident that the gyroscopic torque is oscillatory at the same frequency as the vibrating tines yet in quadrature with it. It appears that an instrument can be designed that transforms the oscillating gyroscopic torque into an output signal. This is accomplished by measuring the magnitude of an oscillating angular displacement of a torsional spring. The measurement signal can then demodulated to determine the applied rate direction, and filtered to eliminate sensitivity to lower frequency torques.

Obviously, the tuning fork instrument has little resemblence to the conventional rotated wheel gyroscope. Conventional gyroscopes are best characterized by an angular momentum vector produced by a spinning member which tends to remain fixed in space. Conventional gyroscopes detect angular rate about a particular axis by measuring the displacement of the spinning axis relative to a gimbal axis. The magnitude of the displacement is proportional to the applied rate about a sensitive axis. On the other hand, the tuning fork instrument has an oscillating angular momentum vector, and yields an AC signal, which has its magnitude at a specified driving frequency proportional to the applied rate about a sensitive axis. Previous papers avoided the label *gyroscope* in describing the tuning fork angular rate sensor. This was meant to keep the reader from thinking of the tuning fork gyroscopic reaction as produced by some fixed angular momentum vector. In this paper, however, the label *gyroscope* is used to describe the micromechanical tuning fork instrument. The reason is simple. The famous French physicist Jean Bernard Foucalt coined the term from its Latin translation *to view rotation*. The prefix *gyro* thus stems from the sensed angular rate, and not the instrument's rotating member.

Throughout the years, many people have had difficulty obtaining a physical *feel* for the action of a conventional gyroscope. With the exception of the spinning top toy, objects with a spinning member are generally not free to be rotated. Therefore, the gyroscopic reaction is not often observed in nature. However, there are several cases in nature where an

oscillating body is rotated. For one example, consider a child playing on a swing set. The child, standing on the swing, is set in motion by a friend pushing him, which is the same as an external torque applied to a rotational system. Slowly, but surely, the swing motion will damp out and the child's ride will end. But , as discovered by many ten year old experimentalists, if the child begins to squat up and down on the swing at the proper frequency, the swing will remain in motion. The squatting produces a periodic variation in the system mass moment of inertia, and hence causes an oscillating torque if it is in phase with the swing oscillation. This torque is proportional to the swing's angular velocity which is analogous to the tuning fork gyroscopic torque.

1.2 Demonstration Model

Even though it is likely that many people, at one time or another, have squatted up and down to force a swing, the reader may remain unconvinced that a tuning fork can sense angular rate. This leads to the first goal in the development of a micromechanical tuning fork gyroscope: to physically demonstrate that a tuning fork can produce a measurable displacement which is proportional to an applied angular rate. To show this, a large scale model was designed to serve the function of a *classroom demonstration model* . It is intended to give greater insight into the physical properties of the device.

The model is shown with dimensions in Figure 1.2. The structure may not look much like a tuning fork, but it has the same basic characteristics. The model consists of a structure closed at both ends containing only a single tine. A closed fork is preferred to an open-ended structure to provide structural integrity and symmetry. For practical purposes a single tine is not desirable since it produces an inertia function which is unsymmetric about the sensitive axis. Unsymmetry leads to unbalance torques and cross-axis sensitivity. However, the demonstration model is operated by simply exciting the tines at their

fundamental frequency. A double tine structure is not feasible since it would require an identical tuning of both tines.

For the single tine the inertia function becomes

$$I_y = \left(I_0 + \frac{I_1}{2}\right) + \frac{I_1}{2} \sin 2\omega_d t \tag{1.1-5}$$

where $I_1 = I_{max} - I_0$, and ω_d = driving frequency (tine fundamental frequency). This differs from the double tine symmetric inertia function given in Eqn. (1.1-1) for two tines. For the single tine, the gyroscopic torque will be vibratory at twice the driving frequency and proportional to half of the oscillating inertia component.

The model was fabricated using beryllium copper sheets, aluminum, bronze, and wood. The single copper tine is fixed at both ends by a sandwich joint between aluminum blocks. Attached at the midpoint of the tine is a bronze block which acts as the high density inertial proof mass. There are two torsional flexures at each end of the device, along the sensitive axis, made from thin rectangular copper tabs which are sandwiched into the aluminum wings and secured to the frame. The frame is attached such that the tension in the tine, and the length of the flexures, can be easily altered. This flexibility is necessary to accurately tune the device since for any appreciable gyroscopic torsional vibration the model must be operated at resonance. This means that the torsional resonant frequency of the flexures must be twice the fundamental frequency of the tine as seen from Eqn. (1.1-5).

The model was designed such that the tine and flexures were stiff enough to hold sufficient energy to reduce damping, yet flexible enough to yield a visible frequency. The flexure torsional stiffness was assumed to follow the equation,

$$K_t = \frac{G}{L} ab^3 [\frac{16}{3} - 3.36\frac{b}{a} + 0.28(\frac{b}{a})^5] \quad \text{where,}$$

G = torsional modulus of elasticity

L = flexure length

$a = \frac{1}{2}$ flexure width

$$\tag{1.1-6}$$

9

$$b = \frac{1}{2} \text{flexure thickness}$$

which is given by Roark and Young [7]. The fundamental frequency of the tine was determined by assuming a fixed-fixed beam, and using Dunkerley's equation [8] to accomodate the effect of the inertial mass, so that,

$$\omega_b{}^2 = \frac{\omega_{11}{}^2 \, \omega_{22}{}^2}{\omega_{11}{}^2 + \omega_{22}{}^2} \qquad \text{where,}$$

$$\omega_{11}{}^2 = 24.7 \left(\frac{EI}{m_b L^3} \right) \quad \text{and} \quad \omega_{22}{}^2 = 6 \left(\frac{EI}{m_m L^3} \right) \qquad (1.1\text{-}7)$$

ω_b = tine fundamental frequency

ω_{11} = fundamental frequency of beam by itself

ω_{22} = fundamental frequency of proof mass on a massless beam\

m_b = mass of tine

m_m = mass of proof mass

L = tine length

Dunkerley's equation is a useful technique in analyzing structures that have known stiffness properties, yet have significant masses attached to them. The equation gives a lower bound for the beam frequency by solving the characteristic equation of the system flexibility matrix, and neglecting the higher mode components.

For the model, the frequencies were calculated at ω_n = 56.3 Hz and ω_b = 20.1 Hz. Tuning the device such that $\omega_n = 2\omega_b$ was accomplished by applying tension to the tine to push up the tine frequency while lengthening the flexures to decrease the torsional frequency, as indicated in Figure 1.3.
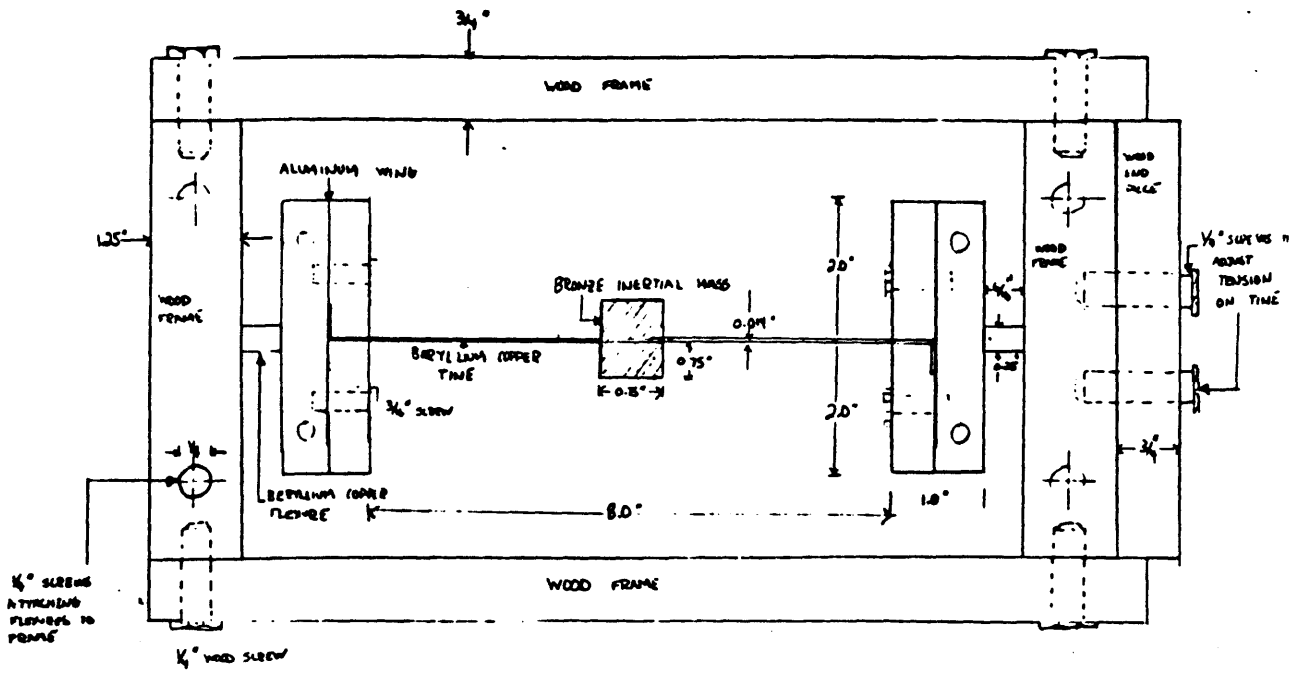
TOP VIEW
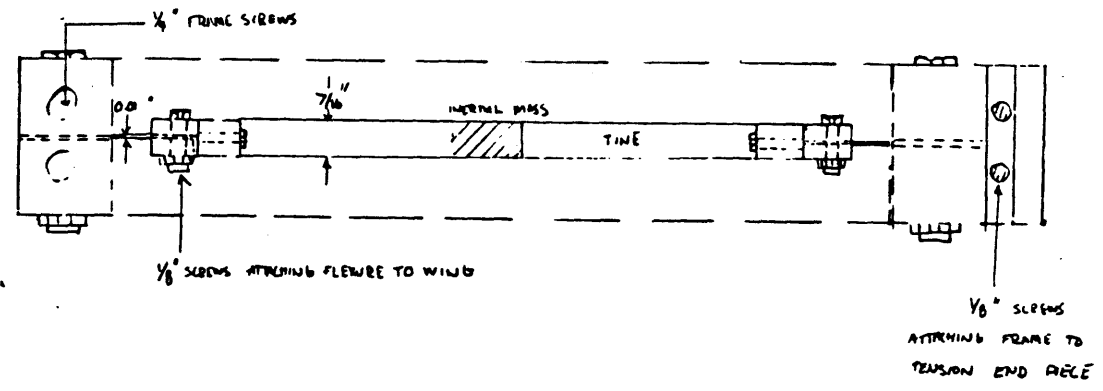
SIDE VIEW

Figure 1.2   Demonstration Model

11

Flexure natural frequency vs flexure length
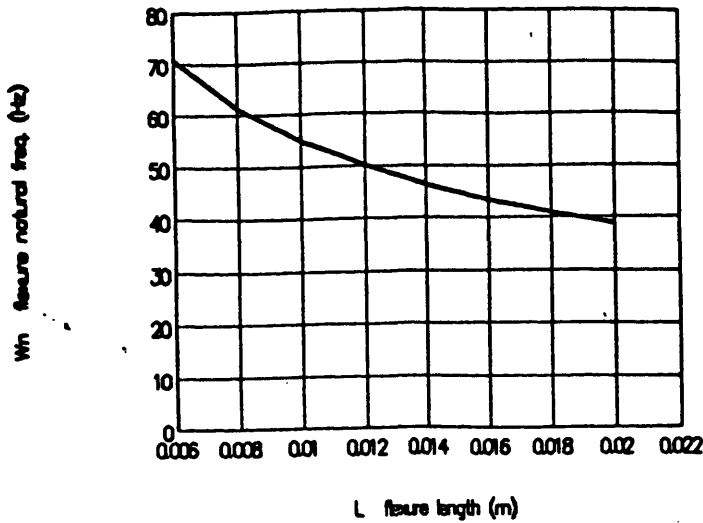
Tine natural frequency vs applied tensile force
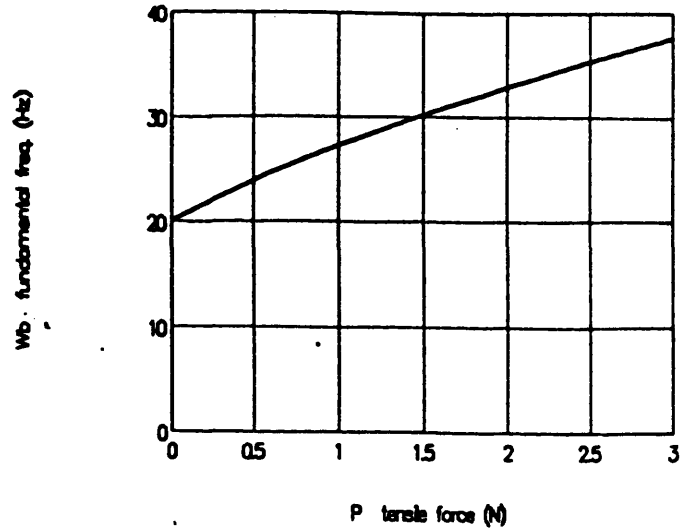
Figure 1.3   Resonance Tuning of Demonstration Model

Several observations were made on the model by vibrating the tine and applying an angular rate, and they are listed below:

1. The forced vibration excites a twisting mode of the tine about the sensitive axis. This mode must be of a sufficiently higher frequency than the driving frequency since it results in an error vibration of the sensing wings.

2. The manually excited tine vibration damps out in less than five seconds due mostly to energy losses in the joint at the wing, and vibration wave reflections back into the beam. This indicates that the device design should have no joints and a stable node where the tines are fixed to the wing.

3. Any misalignment in the z-direction of the proof masses results in an unbalance torque about the sensitive axis. This should be minimized, yet does not provide an error since this torque is in quadrature with the

gyroscope torque as shown later.

4. The thin torsional flexures, with sufficient tension applied, are very stiff in all degrees of freedom as desired.

5. The higher frequency torsional vibrations damp out slowly, mostly due to viscous air flow.

6. Tuning the system was difficult to achieve and maintain. This indicates that the tines should be driven off resonance if possible, and a feedback loop to lock the driving frequency to the torsional resonance is desirable.

7. Gyroscopic action appeared to occur, but was difficult to verify due to tine damping and unbalance vibrations.

1.3 Micromechanical Configuration

Although the model failed to accurately verify the gyroscopic action, it did indicate that a gyroscopic torque can be produced. The model also provided a set of useful guidelines in proceeding with a micromechanical design. The most obvious requirement is that the device should have only two degrees of freedom: a forced lateral tine vibration and rotation about the torsional flexures. A simple, yet practical configuration is a double tined fork, closed at both ends, with the entire structure homogeneous and etched from a silicon chip. Attached at the midpoint of the tines is a high density metal, which serves to increase the oscillating inertia. The flexures are attached to the substrate at each end of the sensitive axis, and the entire fork is suspended over a well which allows the torsional vibration. The configuration is shown in Figure 1.5. The geometry of the configuration is simple enough that it is safe to assume that it can be fabricated by current micromachining processes such as photolithography, masking, doping, selective etching, and electroplating or metallization.

13

The tines will be driven electrostatically by applying a sinusiodal voltage between them. The output signal will be produced by detecting the change in capacitance between the two fork wings and electrodes either suspended above the fork , or buried in the substrate beneath it. This technique has several advantages. By keeping the driving force within the fork, coupling betweeen motor and sensor is eliminated by assuring that no motor force is transfered across the sensor gap. This coupling might represent an error source in the micromechanical gyroscope designed by Boxenhorn [1,2], and in the tuning fork gyroscope designed by Sperry [3,6]. Also, the properties of the silicon allow voltages to be applied on the tines without laying wires across the structure. This configuration also reduces damping since there are no joints, and the only air damping results from the sensor plates on the wings. Various other methods for producing a micromechanical motor have been studied in the literature [9] but electrostatics has been the most successful. The test results of the Boxenhorn micromechanical gyroscope [1] demonstrate the validity of this method.

This configuration appears to offer the benefit of allowing a significant magnitude of the ratio $\frac{I_1}{I_0}$, which is the proportional to the gyroscopic torque, while maintaining only two degrees of freedom. The subsequent chapters will provide a thorough analysis, design, and performance evaluation, based on this configuration.
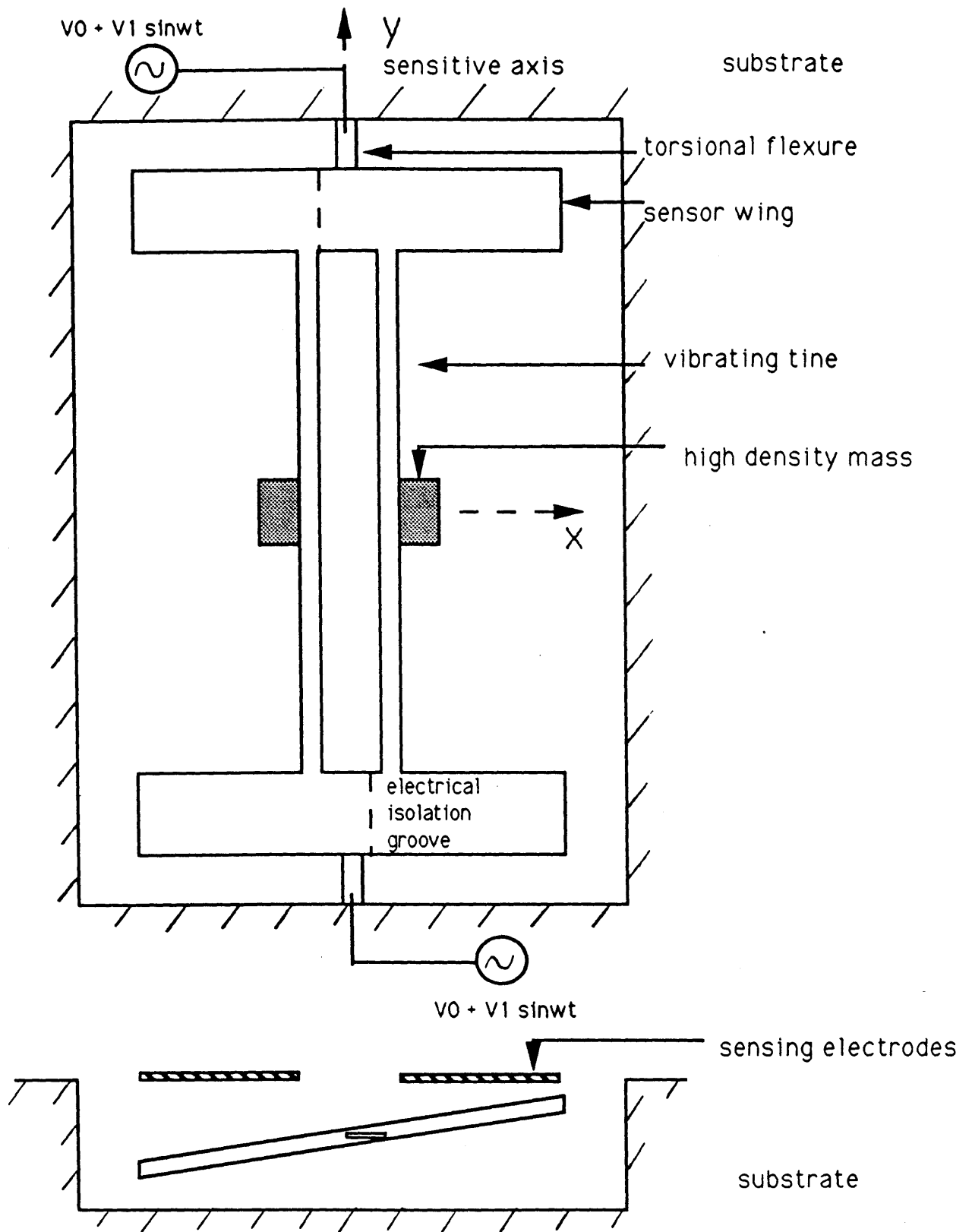
Figure 1.5 Micromechanical Configuration

15

2 DYNAMICS

2.1 System Model

The device is modeled as a dynamic system consisting of only one degree of freedom. Figure 2.1 shows a simplified representation of the system. It contains a rigid oscillating inertia, which represents the fork structure, attached to a torsional spring. The spring is rigidly attached to a base. It might seem ambiguous that tine vibration is not considered a degree of freedom, but since its motion is constrained by the motor and its dynamics are neglected, the tine vibration is accounted in the fixed oscillating inertia term. The tine dynamics are neglected by assuming that the driving frequency is significantly lower than the tine fundamental frequency. Also, the motor is isolated sufficiently such that it exerts no torques on the system. The only external torques acting on the system are the linear spring torque, $k_t\theta$, and a viscous air damping torque, $b_t\dot{\theta}$. The geometry is assumed to be symmetric such that any gravitational field will not result in any moment about the sensitive axis.

Three separate coordinate axes are needed to describe the system and are shown in Figure 2.1. The x-y-z coordinate system is fixed to the base of the fork which is assumed to be strapped to a moving body. The x'-y'-z' axes are fixed to the fork. The y' axis corresponds with the y axis, and is the sensitive axis. The x' axis runs through the center of the fork tines, and is the axis of the lateral tine vibration. The fork-based x' axis is related to the base-fixed x axis by the rotation angle, θ. The z and z' axis are defined by the right hand rule such that the z axis is normal to the substrate plane and the z' axis is normal to the fork plane. The third set of axes represents an inertial reference frame and is denoted by X-Y-Z.

Define the angular rotation of the fork base with respect to the inertial frame as the vector

16

$$\underline{\omega}_{bi} = W_x \, \underline{i}_x + \Omega \, \underline{i}_y + W_z \, \underline{i}_z. \tag{2.1-1}$$

The component about the y axis is denoted by Ω since it is the angular rate that the gyroscope is designed to detect. The angular rotation vector of the fork with respect to the fork base is ,

$$\underline{\omega}_{fb} = \dot{\theta} \, \underline{i}_y.$$

Then, the angular rotation of the fork with respect to the inertial frame, referenced by the x-y-z coordinates is,

$$\underline{\omega}_{fi} = \underline{\omega}_{fb} + \underline{\omega}_{bi} = W_x \, \underline{i}_x + (\Omega + \dot{\theta}) \, \underline{i}_y + W_z \, \underline{i}_z. \tag{2.1-2}$$

The inertia of the fork is defined as a tensor referenced by the x'-y'-z' axes. These axes are chosen because they represent the principal axes for a symmetric design. Then, the inertia tensor can be written as

$$\mathbf{I} = \begin{bmatrix} I_x & 0 & 0 \\ 0 & I_y(t) & 0 \\ 0 & 0 & I_z(t) \end{bmatrix} \tag{2.1-3}$$

The principal inertia components about the y' and z' axes must be written as a function of time due to the lateral vibration,

$$I_y(t) = I_0 + I_1 \sin \omega_d t, \quad \text{and} \quad I_z(t) = I_z + \Delta I_z \sin \omega_d t, \tag{2.1-4}$$

where ω_d designates the motor driving frequency. The fork axes and the fork base axes can be simply related by the rotation angle θ,

$$\underline{i}_x = \underline{i}_{x'} \cos\theta + \underline{i}_{z'} \sin\theta$$

$$\underline{i}_y = \underline{i}_{y'}$$

$$\underline{i}_z = \underline{i}_{z'} \cos\theta - \underline{i}_{x'} \sin\theta. \tag{2.1-5}$$

Substituting (2.1-5) into (2.1-2) gives the angular rotation vector in terms of the fork axes,

$$\underline{\omega}_{fi} = (W_x \cos\theta - W_z \sin\theta) \, \underline{i}_{x'} + (\Omega + \dot{\theta}) \, \underline{i}_{y'} + (W_z \cos\theta + \Omega \sin\theta) \, \underline{i}_{z'} \tag{2.1-6}$$

This represents the angular rotation relative to the the fork principal axes that the device inertia is subjected to.
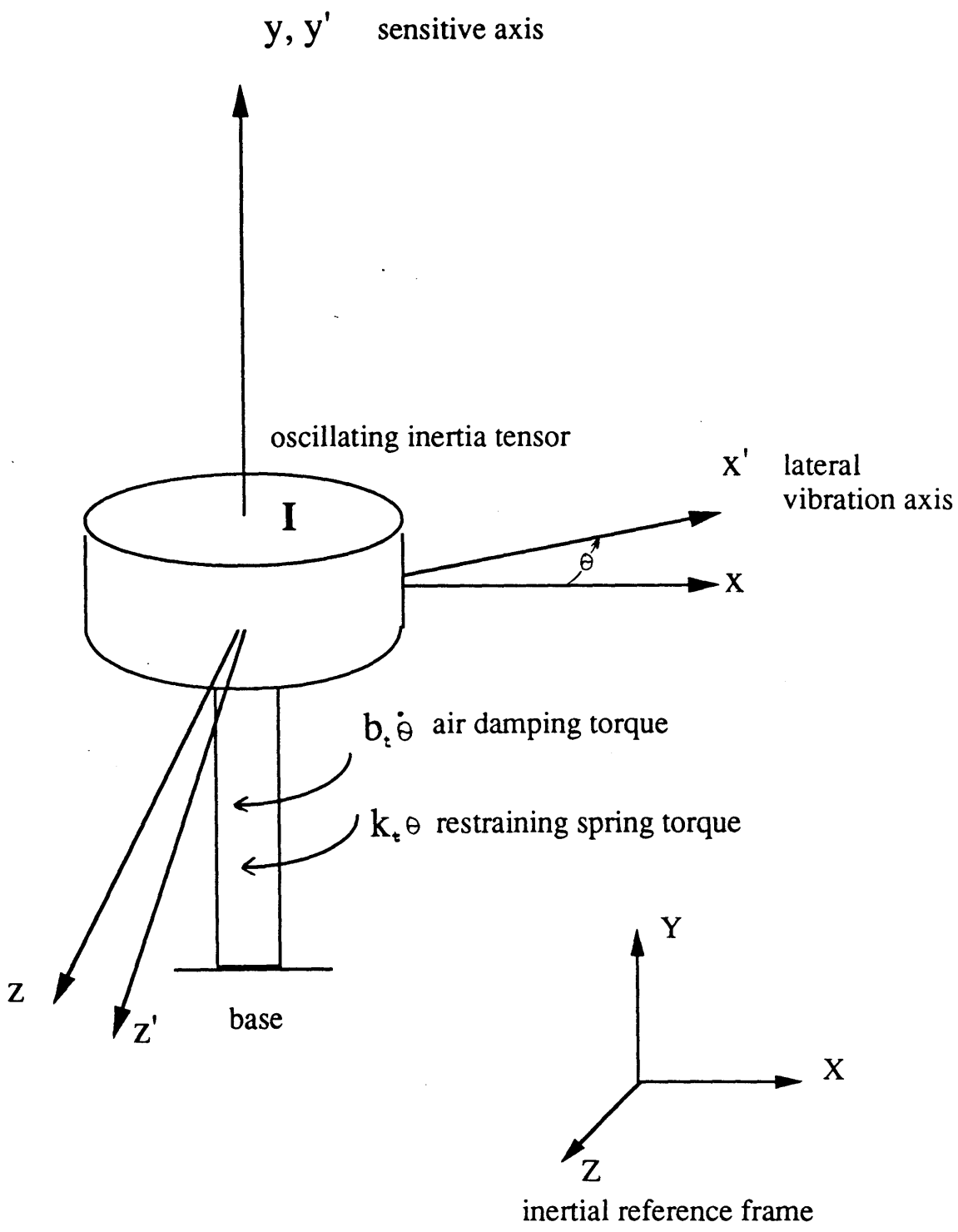
Figure 2.1 System Model

2.2 Neglected Modes

The single degree of freedom model of Figure 2.1 is valid only if the entire fork is rigid and free from structural vibrations. However, as observed from the demonstration model, the high frequency motor and structural unbalances excite other vibration modes. Three modes that demand concern are tine twisting, flexure bending about the x'-axis, and sensor wing bending about the sensitive axis.

The concept of *rigidity* is often loosely defined. In this study it will be assumed that if the free vibration frequency for a specific structural mode is significantly higher than the motor frequency, the mode will remain unperturbed. *Significantly higher* is generally meant meant to mean *more than a factor of four larger* so that the dynamic load factor [7] from the motor is approximately unity.

It is now the intention to show that for preliminary micromechanical design dimensions the three aforementioned modes can be neglected. The modes are analyzed individually as follows:

Tine Twisting: The tine is modeled as a vertical beam fixed at both ends, constrained from warping, and excited by an unbalance moment, T. The moment is applied about the tine longitudinal axis which is parallel to the sensitive axis. Figure 2.2 shows the model, and the torsional spring constant for the tine is given by Roark and Young [7] as

$$k_\phi = \frac{0.3 \, G \, h \, w^3}{L_t} \, .$$

(2.2-1)

The geometric dimensions are given in the figure. The free vibration frequency is then ,

$$\omega_b{}^2 = \frac{k_\phi}{I_t}$$

where I_t is the inertia of a single tine and the attached proof mass about its longitudinal axis. The preliminary design dimensions yield the approximation,

$$I_t \cong \frac{1}{3} I_0.$$

The driving frequency is assumed to be set at the torsional resonance of the flexures which can be determined from the stiffness Eqn. (1.1-6). Substituting, and comparing the twisting frequency to four times the driving frequency,

$$\frac{0.9 \, G \, h \, w^3}{L_t \, I_0} \geq 16 \, \frac{5.3 \, G \, a \, b^3}{L_f \, I_0} \tag{2.2-2}$$

which is valid provided,

$$\frac{h \, w^3}{L_t} \geq \frac{80 \, a \, b^3}{L_f} . \tag{2.2-3}$$

A suitable design, where the tine twisting is negligable, is when $w > 5 \, b$.

Flexure Bending : Each flexure is modeled as a beam fixed at the substrate end and subject to an excitation moment about the wing end. Assuming a Bernoulli - Euler model which neglects shear deformation and rotational inertia [9], the free vibration equation is

$$A \rho \, \ddot{u} \, (y, t) + E I \frac{\partial^4 u \, (y, t)}{\partial y^4} = 0 \tag{2.2-4}$$

where

$\quad A \quad = \quad$ cross sectional area of the beam

$\quad I \quad = \quad$ beam inertia about its neutral axis

$\quad \rho \quad = \quad$ density of the beam material

$\quad u \, (y,t) \quad = \quad$ deflection curve of the beam

A solution of the form $u(y,t) = u(y)e^{i\omega t}$ is assumed, and fixed end - free end boundary conditions are applied. The lowest eigenvalue solution to the transcendental vibration equation [9] is,

$$\omega^2 = \frac{12.4\,E\,I_f}{L_f^4\,\rho\,A_f}$$

(2.2-5)

where the subscripted terms denot the beam inertia, length and cross sectional are of the flexure. Make the approximation E 2G , substitute $I_f = \frac{1}{12}(2a)\,(2b)^3$, and compare to four times the driving frequency as given by (2.2-2) yields,

$$\frac{1}{m_f L_f^2} \geq \frac{40.4}{I_0}.$$

(2.2-6)

This statement is generally satisfied since the mass of the flexures are an insignificant portion of the structure mass.

Wing Bending: Each sensor wing is assumed to be fixed down its centerline, along the sensitive axis, at its attachment to the flexure. The angular rotation, or the tine vibration, could excite a bending moment about the y-axis, as shown in Figure 2.2. Again, using a Bernoulli - Euler beam model with fixed end - free end boundary conditions, the fundamental frequency is given by Eqn. (2.2-5). To correspond with the notation used for the flexure bending, let the wing dimensions be denoted by

L_w = distance from sensitive axis to end of wing

a_w = one-half of wing width

b_w = one-half of wing thickness

m_w = mass of the wing.

Comparing the fundamental wing bending frequency to four times the driving frequency results in,

21

$$\frac{2.1 \, a_w \, b_w{}^2}{L_w{}^3 \, m_w} \geq \frac{40.4 \, a \, b^3}{L_f \, I_0} \, .$$

To approximate, assume the dimensions are such that

$$m_w \, L_w^2 \approx \frac{1}{3} I_0 \quad \text{and} \quad L_w \approx 5 \, L_f \, .$$

Then, the constraint becomes

$$a_w \, b_w^3 \geq 20 \, a \, b^3 \tag{2.2-8}$$

which is achievable for a wing thickness considerably greater than the flexure thickness.

Flexure Bending

Tine Twisting

Wing Bending
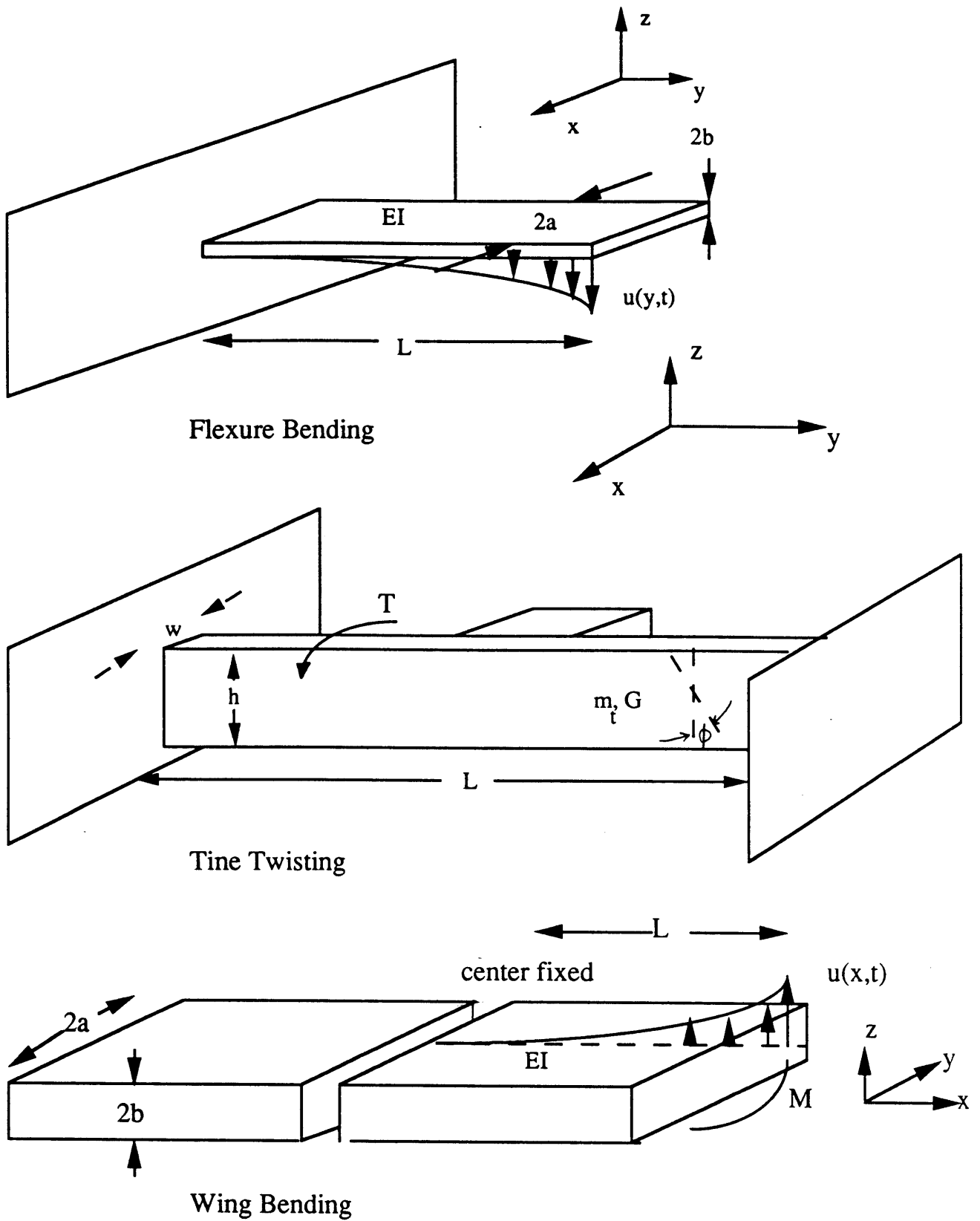
Figure 2.2   Neglected Modes

2.3 Equations of Motion

A simple, direct approach to the system dynamics was undertaken in chapter 1 resulting in the equation of motion given by Eqn. (1.1-4). In the process, several approximations were made and the analysis was only one-dimensional. In order to account for the cross-axis terms, Hamilton's variational approach to the system dynamics is performed which gives a more rigorous, indirect derivation of the equations of motion.

Hamilton's method uses an energy technique to determine the equations that the system variables, or state vector, must obey so that the system remains at equilibrium with the external forces and constraints. Hamilton derived a *variational indicator* which measures the magnitude of deviation from equilibrium due to incremental changes in the state variables. The variational indicator is represented as an integral over the trajectory time period for a sum of system work increments due to the variable deviations. The equations of motion are obtained by setting the variational indicator to zero for arbitrary admissable state variations. Joseph-Louis Lagrange derived a general equation [10] for a system that obeys Hamilton's principle, and which bears his name,

$$\frac{d}{dt}\left(\frac{\partial T}{\partial \dot{\xi}_j}\right) - \frac{\partial T}{\partial \xi_j} + \frac{\partial V}{\partial \xi_j} = \Xi_j$$

(2.3-1)

for j = 1...n   where,   n = the number of state variables, and

T = system kinetic coenergy

ξ_j = generalized coordinate for each state variable

V = system potential energy

Ξ_j = sum of all nonservative forces in the ξ_j dimension.

The reader is referred to Crandall *et al* [10] for a complete description of Hamilton's variational methods.

From the single degree of freedom system model illustrated in Figure 2.1, the only generalized coordinate is $\xi_1 = \theta$. The only nonconservative force acting on the system is the linear damping, so that $\Xi_1 = b_t\dot\theta$. The kinetic coenergy is due to the angular rotation of the fork ,

$$T = \frac{1}{2}\,\underline{\omega}_{fi}\;\mathbf{I}\;\underline{\omega}_{fi}\;. \tag{2.3-2}$$

It should be noted that the system kinetec coenergy is equal to the kinetic energy since the system is defined in a Newtonian reference frame. Substituting for the inertia tensor Eqn. (2.1-3) and the angular rotation vector of Eqn. (2.1-6) gives,

$$T = \frac{1}{2}I_x\left(W_x\cos\theta - W_z\sin\theta\right)^2 + \frac{1}{2}I_y(t)\left(\Omega + \dot\theta\right)^2 + \frac{1}{2}I_z(t)\left(W_z\cos\theta + W_x\sin\theta\right)^2\;.$$

The torsional spring restraining force is the only source of potential energy, so that,

$$V = \frac{1}{2}k_t\,\theta^2\;.$$

For the system, Lagrange's Equation (2.3-1) takes the form,

$$\frac{d}{dt}\left(\frac{\partial T}{\partial\dot\theta}\right) - \frac{\partial T}{\partial\theta} + \frac{\partial V}{\partial\theta} = \Xi_\theta$$

where,

$$\frac{\partial T}{\partial\dot\theta} = I_y(t)\left(\Omega + \dot\theta\right) \qquad \text{and,}$$

$$\frac{d}{dt}\left(\frac{\partial T}{\partial\dot\theta}\right) = I_y(t)\left(\dot\Omega + \ddot\theta\right) + \dot I_y(t)\left(\Omega + \dot\theta\right) \qquad \text{and,}$$

$$\frac{\partial T}{\partial\theta} = -I_x\left(W_x\cos\theta - W_z\sin\theta\right)\left(W_z\cos\theta + W_x\sin\theta\right) + I_z(t)\left(W_z\cos\theta + W_x\sin\theta\right)\left(W_x\cos\theta - W_z\sin\theta\right)$$

$$\tag{2.3-4}$$

Putting it all together, Lagrange's Equation becomes,

2 5

$$I_y(t)\left(\dot{\Omega}+\ddot{\theta}\right) + \dot{I}_y(t)\left(\Omega+\dot{\theta}\right) + I_x\left(W_x\cos\theta - W_z\sin\theta\right)\left(W_x\sin\theta + W_z\cos\theta\right) -$$
$$I_z(t)\left(W_z\cos\theta + W_x\sin\theta\right)\left(W_x\cos\theta - W_z\sin\theta\right) + k_t\theta + b_t\dot{\theta} = 0. \tag{2.3-5}$$

The trigonometric terms in (2.3-5) can be expanded in a Taylor series to transform the equation of motion into algebraic form. To simplify the expansion it can be noted that the rotation angle, θ, is very small. For example, the rotation angle is on the order of 10^{-5} radians for the Boxenhorn gyroscope [1,2], so that first order approximations will result in negligable errors. Letting $\sin\theta \cong \theta$, $\cos\theta \cong 1$, and $\sin^2\theta \cong 0$, and also substituting (2.1-4) for the oscillating inertia functions, the equation of motion becomes

$$\left(I_0 + I_1\sin\omega_d t\right)\left(\dot{\Omega}+\ddot{\theta}\right) + I_1\omega_d\cos\omega_d t\left(\Omega+\dot{\theta}\right) + \left(W_x^2 - W_z^2\right)\left(I_x - I_z(t)\right)\theta + k_t\theta + b_t\dot{\theta} = W_x W_z\left(I_x - I_z(t)\right) \tag{2.3-6}$$

This second order differential equation represents the complete description of the tuning fork gyroscope subject to an angular rate vector. In the literature on tuning fork gyroscopes, only Fearnside and Briggs [5] included the cross-axis and small order terms in the dynamics analysis. However, the analysis done by Fearnside and Briggs differs from this paper in a few respects. Fearnside and Briggs assume the damping is of large magnitude, which is not the case on a micromechanical level. They are then able to neglect second order terms of the ratio $\dfrac{I_1\,\omega_d}{b_t}$. This reduces the significance of the time-varying terms present for a lightly damped system which is studied in chapter 3. They also use a direct approach to the dynamics and simply drop all cross-axis terms after noting that they limit the device accuracy.

The first simplification made on Eqn. (2.3-6) is to neglect the angular acceleration term, $\dot{\Omega}$. The driving frequency is assumed to be high enough such that the frequency of the input rate is negligable in comparison. It is then possible to drop the $\dot{\Omega}$ term from the equation of motion. It must be noted that a limitation is placed on the system bandwidth, but the limitation is insignificant for practical applications. The driving frequency for a

equation of motion. It must be noted that a limitation is placed on the system bandwidth, but the limitation is insignificant for practical applications. The driving frequency for a micromechanical device is assumed to be in the 1-5 kHz range, and applications in guidance or control areas do not require bandwidths greater than 100 Hz. The input frequency is thus negligable compared to the output frequency, and no significant error results from dropping the $\dot{\Omega}$ term. The equation of motion can now be written in a more convenient form,

$$(I_0 + I_1 \sin \omega_d t) \ddot{\theta} + (b_t + I_1 \omega_d \cos \omega_d t) \dot{\theta} + k_t \theta = -I_1 \Omega \omega_d \cos \omega_d t$$
$$+(I_x - I_{0z}[W_x W_z - (W_x^2 - W_z^2) \theta] - I_{1z}[W_x W_z +(W_x^2 - W_z^2) \theta] \sin \omega_d t \qquad (2.3\text{-}7)$$

2.4 Simplified Output Solution

A closed form solution to Eqn.(2.3-7) is not apparent. The first step to understanding the behavior of the system is to drop all terms that complicate the equation and can be reasoned to have minimal effect on the solution. The cross-axis terms on the right hand side of the equation will be dropped first. These terms comprise a torque about the sensitive axis that is much smaller than the spring restraining torque, the damping torque, and the gyroscopic torque. The following section will give a more thorough analysis of the cross-axis effects. The equation can now be transformed to a solvable form if I_1 is considered much smaller than I_0, and $I_1 \omega_d$ is much smaller than b_t. The equation is then a second order, constant coefficient, harmonically forced oscillator,

$$I_0 \ddot{\theta} + b_t \dot{\theta} + k_t \theta = -I_1 \Omega \omega_d \cos \omega_d t. \qquad (2.4\text{-}1)$$

Assume a solution of the form,

$$\theta = A \sin \omega_d t + B \cos \omega_d t,$$

substituting gives,

$$A = \frac{-I_1 \Omega \omega_d^2 b_t}{-I_0\left(k_t - I_0 \omega_d^2\right) + k_t\left(k_t - I_0 \omega_d^2\right) + \omega_d^2 b_t^2}$$

and,

$$B = k_t - I_0 \omega_d^2 . \qquad (2.4\text{-}2)$$

The rotation angle can be maximized if the driving frequency is set at the torsional natural frequency such that,

$$\omega_d = \omega_n = \sqrt{\frac{k_t}{I_0}} = \omega . \qquad (2.4\text{-}3)$$

Hereafter in this paper, when the frequency is denoted by the symbol ω without a subscript, it denotes the driving frequency tuned to the torsional resonant frequency. The output is then a pure sine curve, in phase with the motor vibration,

$$\theta(t) = \frac{-I_1 \Omega}{b_t} \sin \omega t . \qquad (2.4\text{-}4)$$

The linear damping coefficient can be written in terms of the system quality factor, Q,

where $b_t = \dfrac{I_0 \omega}{Q}$. A more convenient expression for the simplified output solution is

$$\theta(t) = \frac{-I_1 Q \Omega}{I_0 \omega} \sin \omega t . \qquad (2.4\text{--}5)$$

If all the assumptions for the simplified solution are valid, the output angle is proportional to the ratio of the oscillating inertia component to the nominal inertia component, the system quality factor, the magnitude of the applied rate, and inversely proportional to the driving frequency. This gives a calibrated measure of the angular rate about the sensitive axis. The output signal can also be demodulated with the driving oscillation as a reference

2.5 Simplified Output Transient Response

Eqn. (2.4-5) gives the steady state vibration of the harmonically forced, linear system. However, the second order dynamics of the tuning fork will lead to an oscillating transient period that must be investigated in terms of system bandwidth. Eqn. (2.4-1) can be written in the following form,

$$\ddot{\theta} + \frac{\omega_n}{Q}\dot{\theta} + \omega_n^2\theta = \frac{-I_1\Omega\,\omega_d}{I_0}\cos\omega_d t \ .$$

(2.5-1)

Let $I_1(t) = I_1\sin\omega_d t$, then Eqn. (2.5-1) can be written,

$$\ddot{\theta} + \frac{\omega_n}{Q}\dot{\theta} + \omega_n^2\theta = \frac{-\dot{I}_1(t)\,\Omega}{I_0} \ .$$

Since this equation is linear, Laplace transforming yields,

$$\frac{\theta}{\Omega} = \frac{\dfrac{-I_1}{I_0}\,s}{s^2 + \dfrac{\omega_n}{Q}s + \omega_n^2} = G(s) \ .$$

(2.5-2)

G(s) represents the system transfer function, but it can not identify the system bandwidth since it relates the input signal which has unknown frequency to an output signal oscillating at the driving frequency. In order to transform G(s) into a DC transfer function, $G_m(s)$, the output signal is frequency modulated at the driving frequency. This means,

$$\theta_m(t) = \theta(t)\,e^{-j\omega_d t} \quad \text{or, in the Laplace domain,}$$
$$\theta_m(s) = \theta(s + j\omega_d) \ .$$

Replace s by $s + j\omega_d$ to give the DC transfer function,

$$\frac{\theta_m}{\Omega} = \frac{\dfrac{-I_1}{I_0}(s + j\omega_d)}{(s + j\omega_d)^2 + \dfrac{\omega_n}{Q}(s + j\omega_d) + \omega_n^2} = G_m(s) \ .$$

(2.5-3)

Expanding, rationalizing, and setting the driving frequency at the resonant frequency,

$$G_m(s) = \frac{\frac{-I_1}{I_0}(s+j\omega)\left[s\left(s+\frac{\omega}{Q}\right)-2j\omega\left(s+\frac{\omega}{Q}\right)\right]}{4\omega^2\left(s+\frac{\omega}{2Q}\right)^2+s^2\left(s+\frac{\omega}{Q}\right)^2}.$$

(2.5-4)

Assuming that the system bandwith is much lower than the driving frequency , the components of the transfer function can be written,

$$\text{Imag}\,(G_m(s)) = \frac{\frac{-I_1}{I_0}\left[s\left(s+\frac{\omega}{Q}\right)\right]}{4\omega\left(s+\frac{\omega}{2Q}\right)^2} \quad \text{and},$$

$$\text{Real}\,(G_m(s)) = \frac{\frac{-I_1}{I_0}}{2\left(s+\frac{\omega}{2Q}\right)}.$$

(2.5-5)

It is clear that the quadrature component is small compared to the in-phase component so that the signal has negligable phase shift during the transient period, and the sytem bandwidth is

$$BW = \frac{\omega}{2Q}.$$

(2.5-6)

2.6 Cross Axis Terms

The right hand side of Eqn. (2.3-7) consists of the gyroscopic torque term plus four terms due to the input rate about the axes orthogonal to the sensitive axis. These terms lead to torques about the sensitive axis of unknown magnitude. But, if these torques can be shown to either have negligable effect on the system, or cause an output deflection that has no component that is in-phase with the motor at the driving frequency, no error signal will result. This is because appropriate signal filtering and demodulation can eliminate all signals from the sensor rotation except the vibrational component in phase with the motor within a

30

component that is in-phase with the motor at the driving frequency, no error signal will result. This is because appropriate signal filtering and demodulation can eliminate all signals from the sensor rotation except the vibrational component in phase with the motor within a small frequency band about ω_d. However, any quadrature or off-frequency signal must not exceed the designed output range of the gyroscope.

The cross axis terms are analyzed term by term:

1) $(I_x - I_{0z})(W_x W_z)$:   This causes a DC output which can be filtered out. The bias that it causes can be made as small as possible by designing the nominal inertias about the x and z axes to correspond. It appears from Figure 1.5 that the symmetry can be easily obtained by adjusting the x and y dimensions of the proof masses.

2) $(I_x - I_z)(W_x^2 - W_z^2) \theta$:   For a symmetric design where $I_x \cong I_{0z}$, this term can be regarded as a small deviation in the spring constant. But, assuming a driving frequency in the 2-4 kHz range, and a practical limit on the cross axis rates of around 20 Hz, then $k_t = \omega^2 I_0 \gg (I_x - I_{0z})(W_x^2 - W_z^2)$. Hence, this term will have less than a 0.01% deviation on the spring constant and will not alter the output significantly.

3) $\Delta_{Iz} W_x W_z \sin \omega t$: Δ_{Iz} is the oscillation inertia about the z-axis, and is thus small and on the order of I_1. Again, for a high frequency system, this term is tiny compared to the gyroscopic torque for any significant Ω. It is also in quadrature with the gyroscopic torque, so even for very small values of Ω, the majority of the error signal from this term will be eliminated by demodulation.

4) $\Delta_{Iz}(W_x^2 - W_z^2) \theta \sin \omega t$:   This term can be viewed as a high frequency deviation in the spring constant. Since I_{1z} is generally on the order of 1% of I_{0z}, the maximum deiviation in the spring constant from this term is only about 0.0001%. And the frequency component of

31

the term does not lead to difficulties since, when combined with the sinusoidal output, it results in a double frequency torque.

In general, the cross axis terms do not lead to a significant limit on the accuracy of the device. As shown in the subsequent chapters, for a micromechanical device, Brownian and electronics noise are the predominant error sources. Zero rate errors, such as cross-axis coupling, tend to be insignificant by comparison.

3   SYSTEM RESPONSE ANALYSIS

In this chapter, the system response to the complete equation of motion will be studied. For the tuning fork to operate efficiently as an angular rate sensor, the output angle must be a linear function of the input rate. Eqn. (2.4-5) shows a linear relationship, but in its derivation the periodic terms in the equation of motion were neglected. It is necessary to verify that the periodic terms have a negligable effect on the system response. A brief overview of linear periodic equations is presented, and then the tuning fork equation of motion is analyzed by several different analytical and numerical tools.

3.1 Periodically Time - Varying System

If the cross axis terms are neglected and the system is driven at its torsional resonance so that $\omega_n = \omega_d = \omega$, the complete equation of motion (2.3-7) becomes,

$$\left(1 + \frac{I_1}{I_0} \sin \omega t\right) \ddot{\theta} + \left(\frac{b_t}{I_0} + \frac{I_1}{I_0} \omega \cos \omega t\right) \dot{\theta} + \omega^2 \theta = -\frac{I_1}{I_0} \Omega \omega \cos \omega t \qquad \text{or,}$$

$$\left(1 + \varepsilon \sin \omega t\right) \ddot{\theta} + \left(\frac{\omega}{Q} + \varepsilon \omega \cos \omega t\right) \dot{\theta} + \omega^2 \theta = -\varepsilon \Omega \omega \cos \omega t .$$

$$(3.1-1)$$

where

$$\varepsilon = \frac{I_1}{I_0} \qquad \textit{the mechanical gain}$$

$$Q = \quad \text{sytem quality factor.}$$

Generally, the mechanical gain is a small number, and the quality factor is defined in Eqn. (2.4-5). Equation (3.1-1) is a linear, time varying, periodic differential equation (LP) of second order. Equations of this form have arisen in many different fields of application,

and hence many different analytical methods to describe the behavior of such systems have been studied. The problem is that there is no uniform approach, such as the Laplace transform for linear, time-invariant, differential equations, to describe these systems. There are also no known exact solutions, which makes it necessary to treat each equation individually by the most appropriate approximate method.

The equation of motion (3.1-1) is of the form

$$a(t)\ddot{x} + b(t)\dot{x} + c(t)x = d(t)$$

where a, b, and the forcing function d, are all periodic of period $T = 2\pi/\omega$. The main deficiency with the simplified solution of Chapter 2 is that even though $a(t) \cong 1$ since ε is small, the periodic component of $b(t)$ cannot be accurately neglected since $1/Q$ is on the same order as ε for a lightly damped micromechanical system. This type of equation, with nearly constant a and c and periodic b, is a rare and unexplored form of an LP equation. Intuitively, the response to Eqn. (3.1-1) will be approximately the steady state and transient response of sections 2.4 and 2.5 for a small value of the product parameter, εQ. But when εQ grows greater than unity, and the periodic component of $b(t)$ begins to dominate, the oscillating response will deviate from the simplified solution. This can be viewed as a periodic perturbation in the damping, so that as εQ increases the output frequency should remain constant, but the output magnitude, phase, and bandwidth will be affected.

The periodic variation in the damping is an effective *energy pumping* of the system. This results in a substantial increase or decrease in the amplitude of the output oscillations. A physical example of *energy pumping* from the circuit design field is presented by Richards [11]. By periodically changing the capacitor plate distance in an LC circuit network, it is possible to *pump* the voltage across the capacitor, which results in a periodic damping term. When done at the proper frequency and phase, this increases the magnitude of the voltage across the capacitor. This view leads to the conclusion that for specific values of the parameter εQ the output magnitude will increase without bound, and the system will cease to

be globally stable. The product of the mechanical gain and the system quality factor, ϵQ, will thus be referred to as the *stability parameter*.

The stability problem of periodic systems is unique because small variations in a periodic coefficient can cause the system to lie in a region of instability, separated by regions of stability. In the tuning fork case, this means that as ϵQ is increased past a certain limit the response could go unstable, but a continued increase in the parameter could stabilize the system. The stability problem of periodic systems has been studied in depth, with particular emphasize by Maclachlan [12], Richards [11], and Porter [13].

An optimized design of the micromechanical tuning fork gyroscope will maximize the parameter ϵQ, since it is a factor in the output magnitude as shown by (2.4-5). It is thus imperative to determine the stability characteristics of this parameter. Several techniques to determine the stability of periodic systems exist. They include transformation to the Mathieu equation, Lyapunov stability theory, Floquet theory, and numerical simulation.

In the literature, much research has been done on homogeneous equations of the form

$$\ddot{x} + [\, a - 2 q \, \psi \, (t)]\, x \; = \; 0 \; ,$$

where $\psi \, (t)$ is a periodic function. This is known as Hill's equation and has its roots date back to 1886. A special case of Hill's equation that has received particular attention in regard to stability is the Mathieu equation, and is given by

$$\ddot{x} + [\, a - 2 q \cos 2t]\, x \; = \; 0 \; . \tag{3.1-2}$$

Approximate periodic solutions to Eqn. (3.1-2) have been obtained as a function of the parameters a, q. Since the stability regions for the parameters have been well documented [11,12], a useful technique to determine the stability of a particular LP system is to transform it to the Mathieu equation. Then the characteristics of the transformed equation, plus the particular transformation, yield information about the original equation. The disadvantage of this approach is that an appropriate transformation must be found, and information can be lost in the transformation.

Another approach is based on Floquet theory. This is recently emerging as a useful technique to give an exact *yes* or *no* answer to a particular system stability. However, this approach is limited in that it requires the computation of a discrete transition matrix, and its respective eigenvalues, for a given set of parameters. For the majority of LP systems, the discrete transition matrix cannot be obtained in closed form. Numerical techniques must be used and the stability conclusions are only obtained for specific values of the parameters.

Lyapunov stability theory, a more theoretical approach, uses mathematical functional analysis to check if a suitable bound can be determined for the system response. It has been used successfully for many particular periodic equations, but it requires the formulation of a suitable Lyapunov function. There is no defined method to determine the Lyapunov function, and extensive trial and error is often the method employed. Unfortunately, the Lyapunov function is not easily obtained for the tuning fork equation.

The last possible technique, numerical simulation, has the problems of truncation and round-off error, and is very sensitive to errors around the stability limits. Also, the high frequency oscillations in an unstable region can grow slowly over many periods, so extensive computation time is needed to reach conclusions. Simulation, though, can be used to reinforce analytical results and verify the forced system response.

3.2 Stability in Terms of the Mathieu Equation

In order to transform Eqn. (3.1-1) into a form of the Mathieu equation of (3.1-2), it is first written in a more convenient form. Dividing through by the a(t) term and noting the first order expansion

$$\frac{1}{1 + \varepsilon \sin \omega t} = 1 - \varepsilon \sin \omega t + O\left(\varepsilon^2\right) \qquad (3.2\text{-}1)$$

gives,

$$\ddot{\theta} + \left(\frac{\omega}{Q} + \varepsilon\,\omega\cos\omega t\right)\left(1 - \varepsilon\sin\omega t\right)\dot{\theta} + \omega^2\left(1 - \varepsilon\sin\omega t\right)\theta = -\varepsilon\,\Omega\,\omega\left(1 - \varepsilon\sin\omega t\right)\cos\omega t\,.$$

Again, neglecting the second order terms in ε, gives

$$\ddot{\theta} + \left(\frac{\omega}{Q} + \varepsilon\,\omega\cos\omega t - \frac{\varepsilon\,\omega}{Q}\sin wt\right)\dot{\theta} + \omega^2\left(1 - \varepsilon\sin\omega t\right)\theta = -\varepsilon\,\Omega\,\omega\cos\omega t\,.$$

If, for a lightly damped system, the parameter $\frac{1}{Q}$ is on the order of ε, then the sine

component of the b(t) term is negligable compared to the cosine component. This gives

$$\ddot{\theta} + \left(\frac{\omega}{Q} + \varepsilon\,\omega\cos\omega t\right)\dot{\theta} + \omega^2\left(1 - \varepsilon\sin\omega t\right)\theta = -\varepsilon\,\Omega\,\omega\cos\omega t\,. \tag{3.2-2}$$

An appropriate change of variables must be found that eliminates the b(t) term from

the homogeneous form of Eqn. (3.2-2). An appropriate transformation [11] is

$$x = \theta\,\exp{-\left(\frac{1}{2}\int_0^t b\,(\tau)\,d\tau\right)} \tag{3.2-3}$$

which transforms the equation

$$\ddot{\theta} + b(t)\,\dot{\theta} + c(t)\,\theta = 0 \qquad\qquad \text{into}$$

$$\ddot{x} + \left[c(t) - \frac{1}{2}\dot{b}(t) - \frac{1}{4}b^2(t)\right]x = 0. \tag{3.2-4}$$

Substituting the values for a(t) and b(t) from Eqn. (3.2-2) yields the transformed equation,

$$\ddot{x} + \omega^2\left[\left(1 - \frac{1}{4\,Q^2}\right) - \frac{1}{2}\varepsilon\sin\omega t - \frac{1}{2}\frac{\varepsilon}{Q}\cos\omega t - \frac{\varepsilon^2}{4}\cos^2\omega t\right]x = 0. \tag{3.2-5}$$

The oscillating component of the second term of Eqn. (3.2-5) is approximated by the sine

component since $Q \gg 1$ and $\varepsilon \ll 1$. The transformed equation is then written

$$\ddot{x} + \omega^2 \left[\left(1 - \frac{1}{4Q^2} \right) - \frac{1}{2} \varepsilon \sin \omega t \right] x = 0.$$

$$(3.2-6)$$

To put this in the form of Eqn. (3.1-2) a change is made in the independent variable. Let,

$$\tau = \frac{\omega t}{2} - \frac{\pi}{4}.$$

Eqn. (3.2-6) is then written,

$$\frac{d^2 x}{d\tau^2} + \left[\left(4 - \frac{1}{Q^2} \right) - 2\varepsilon \cos 2\tau \right] x(\tau) = 0.$$

$$(3.2-7)$$

Equation (3.2-7) is in the form of the Mathieu equation with the parameters

$$a = 4 - \frac{1}{Q^2} \quad \text{and} \quad q = \varepsilon.$$

An approximate solution to the Mathieu equation was first introduced by E. L. Ince in 1932. Since then, many mathematicians have studied the equation, and very accurate approximate series solutions exist. The reader is referred to Mclachlan [12] for a thorough treatise of the Mathieu equation and its solutions. A simple explanation of the solution technique, and its application to the transformed tuning fork gyroscope equation of motion, is presented here.

Since the Mathieu equation is second order and linear, the general solution is

$$x(\tau) = C_1 x_1 (\tau) + C_2 x_2 (\tau)$$

$$(3.2-8)$$

provided that the system Wronskian vanishes identically. For a differential equation of period T, it has been proven by Floquet [11] that the system solution at any time τ is related to the solution at time $\tau + T$ by a complex constant factor. This says,

$$x (\tau + T) = \sigma x(\tau).$$

$$(3.2-9)$$

The two independent particular solutions of (3.2-8) are then

$$x_1 (\tau + T) = a_1 x_1 (\tau) + a_2 x_2 (\tau)$$

$$x_2 (\tau + T) = a_3 x_1(\tau) + a_4 x_2 (\tau).$$

$$(3.2-10)$$

38

where the a's represent arbitrary complex constants. Combining (3.2-10) with (3.2-8) and (3.2-9) gives,

$$[(a_1 - \sigma) C_1 + a_2 C_2] + [a_3 C_1 + (a_4 - \sigma) C_2] = 0. \qquad (3.2-11)$$

A nontrivial solution to this equation exists only if

$$\begin{vmatrix} a_1 - \sigma & a_3 \\ a_2 & a_4 - \sigma \end{vmatrix} = 0. \qquad (3.2-12)$$

The Wronskian of the Mathieu equation is defined as

$$W = \begin{vmatrix} x_1 & x_2 \\ \dfrac{dx_1}{d\tau} & \dfrac{dx_2}{d\tau} \end{vmatrix}$$

It was shown by Porter [13] that for two independent solutions to the Mathieu equation, x_1 and x_2,

the derivative of the Wronskian, $\dfrac{dW}{d\tau}$, is identically zero. Then,

$$W (\tau) = W (0), \quad \text{and} \quad W (\tau + T) = W (\tau).$$

It is seen from Eqn. (3.2-10) that

$$W (\tau + T) = (a_1 a_4 - a_2 a_3) W (\tau).$$

Therefore,

$$a_1 a_4 - a_2 a_3 = 1 .$$

Substituting this into the determinant equation (3.2-12), a relationship is obtained between two of the arbitrary constants and the periodic scaling factor, σ

$$\sigma^2 - (a_1 + a_4) \sigma + 1 = 0. \qquad (3.2-13)$$

A root locus for this equation can be drawn where the free parameter, or gain , is

$$K = a_1 + a_4.$$

When K = 2 and K = -2, the roots become σ = -1, and σ = 1, respectively. At this point, when the roots σ cross from within the complex plane unit circle to outside the unit circle, the system becomes unstable. This is analogous to the stability criteria of a discrete system with poles in the z-plane. The instability is seen by noting that if the magnitude of σ exceeds unity the system output of Eqn. (3.2-9) will increase each period. The analogy to discrete systems is another interesting topic altogether, and it enables periodic systems to be readily analyzed in discrete state space form. This is the basis to Floquet theory which is studied in a forthcoming section.

From Eqn. (3.2-9) it is seen that for σ = 1 the solution is periodic with period T, and for σ = -1 the solution is periodic with period 2T. The Mathieu equation has period π , so the goal is to adjust the value of the parameters, a and q , until solutions that have period π or 2π are found. The corresponding values of the parameters represent the stability boundaries. It is noted from the Mathieu equation (3.1-2) that as q approaches zero the system reduces to a free oscillator with solution,

$$x\,(t)\;=\;C_3 \sin mt\;+\;C_4 \cos mt\,,$$

$$\text{for}\;\;m^2\;=\;a\,.$$

Assume an infinite series solution, that is periodic in π or 2π, and reduces to the free oscillator, in the form,

$$x1\,(t)\;=\;\cos mt\;+\;q\,C_{11}\,(t)\;+\;q^2\,C_{12}\,(t)\;+\;...$$

$$x2\,(t)\;=\;\sin mt\;+\;q\,C_{21}\,(t)\;+\;q^2\,C_{22}\,(t)\;+\;... \qquad (3.2\text{-}14)$$

Since there are two parameters, the technique is to fix q, and write a as a power series in q,

$$a\;=\;1\;+\;\alpha_1\,q\;+\;\alpha_2\,q^2\;+\;... \qquad (3.2\text{-}15)$$

For both the even and odd solutions, substituting Eqns (3.2-14) and (3.2-15) into the Mathieu equation [12] yields differential equations for the coefficients C_{ij}. It is shown [12,13] that the resulting differential equations can be solved for an infinite sequence of discrete values for the parameter a. These values are known as *characteristic numbers* and the corresponding curves from Eqn.(3.2-15) are the *characteristic curves*.

40

Mclachlan [12] calculates the characteristic curves to high accuracy for both the even and odd solutions, and labels them a_n and b_n, respectively. The curves are plotted in the a-q plane, and the regions bounded by the curves are checked by substitution to determine if they represent stable or unstable regions. This stability chart is called the *Strutt diagram* after the mathematician who first introduced it. A reprint of Mclachlan's diagram is shown in Figure 3.1. In the figure, the shaded regions are the unstable areas, and the unshaded regions are stable areas.

For the transformed equation of motion (3.2-7) the Mathieu parameters are

$$a = 4 - \frac{1}{Q^2} \quad \text{and} \quad q = \varepsilon. \tag{3.2-16}$$

This point lies very near the b_2 curve in the a-q plane shown in Figure 3.1. For this point to lie in a stable region, the parameters are restricted to place the point below the b_2 curve. Mclachlan's expansion for the b_2 curve is truncated to give

$$b2: \quad a = 4 - \frac{1}{12}q2 + O(q^4).$$

Substituting from Eqn. (3.2-16)

$$b2: \quad 4 - \frac{1}{Q^2} = 4 - \frac{1}{12}\varepsilon^2 + O(\varepsilon^4). \tag{3.2-17}$$

The stability boundary is then,

$$\varepsilon Q = \sqrt{12} \tag{3.2-18}$$

For the point to lie in the stable region of Figure 3.1, it is seen that,

$$\varepsilon Q < \sqrt{12}. \tag{3.2-19}$$

The approximate stability boundaries for the transformed equation are quite accurate. The remaining problem is to determine the relationship between the stability of the transformed equation (3.2-7) and the original equation (3.1-1). First, the change in the independent variable from t to τ, from Eqn. (3.2-7), does not affect the stability characteristics. It is a scaling and shift on the time axis. Stability criteria involves the limit as time approaches infinity, thus a scaled shift does not affect stability definitions. The
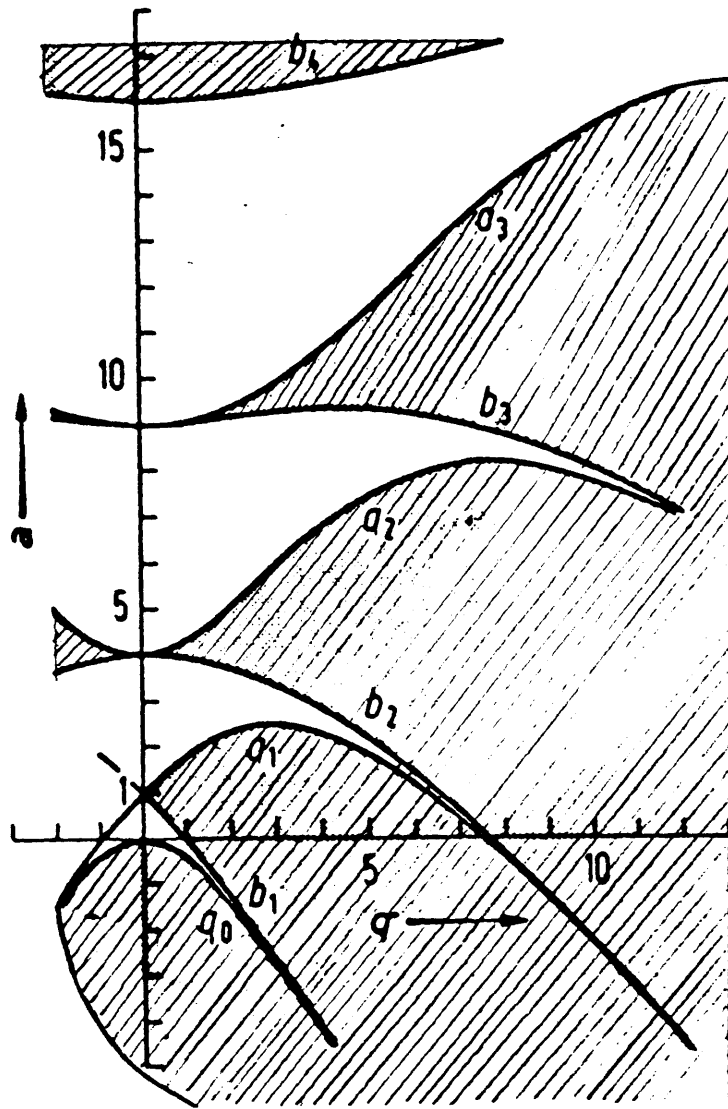
Figure 3.1   Stability Regions for the Parameters of the Mathieu Equation

42

dependent variable change is given by Eqn. (3.2-5). The variable of concern, θ, is equal to the transformed variable, x, multiplied by a scaling function

$$\theta(t) = x(t) k(t) \quad \text{where,}$$
$$k(t) = \exp\left[-\frac{1}{2}\omega\left(\frac{1}{Q}t + \varepsilon \sin \omega t\right)\right].$$

A matter of concern is that the scaling function does not contain one-to-one correspondence. But, the function is bounded by

$$k_{ub} = \exp\left(\frac{\varepsilon\omega}{2} - \frac{\omega}{2Q}t\right) = k_0 \exp\left(-\frac{\omega}{2Q}t\right)$$

where the initial constant is $\quad k_0 = \exp\left(\frac{\varepsilon\omega}{2}\right)$.

For a high frequency, the upper bound of the scaling function is a large number at time t = 0, then it quickly dies to zero. Therefore, at the upper bound, the scaling function magnifies the transformed variable, x (t), for small values of time. As time increases the scaling function drives x (t) to zero. If the variable x (t) is shown to be stable, then the transformation cannot destabilize the response, so that θ (t) is also stable. The restriction given by Eqn. (3.2-19) is thus a _sufficient_, but not necessary, condition for stability of the equation of motion.

3.3 Approximate Forced System Response by Harmonic Balance

In this section, the effects that the periodic terms in the equation of motion have on the *forced* response is analyzed. As discussed in section 3.1, it is believed that the existence of the periodic terms will produce a phase shift from the simplified sinusoidal approximation of Eqn. (2.4-5). The system can be written in state space form,

$$\dot{x}(t) = G(t) x(t) + B(t) \Omega$$

where,

$$x(t) = \begin{bmatrix} x_1 \\ x_2 \end{bmatrix}, \quad G(t) = \begin{bmatrix} 0 & 1 \\ -\omega^2 \left(1 - \varepsilon \sin \omega t\right) & -\dfrac{\omega}{Q} - \varepsilon\omega \cos \omega t \end{bmatrix}$$

$$B(t) = \begin{bmatrix} 0 \\ -\varepsilon \omega \cos \omega t \end{bmatrix}$$

(3.3-1)

The variable x_1 denotes the output angle θ. The input to the system is the magnitude of the applied rate about the sensitive axis since only the open loop system is studied. It is seen that both the plant and forcing matrix can be written in standard periodic form

$$G(t) = A_{sys} [\sin (\omega t + \phi_{sys})] \quad \text{and} \quad B(t) = A_{inp} [\sin (\omega t + \phi_{inp})]. \quad (3.3\text{-}2)$$

The A and ϕ matrices designate the amplitude and phase of the periodic functions. A graphical description of the system is shown in Figure 3.2. The steady state output of the system can then be written in the same form,

$$x(t) = A_{out} [\sin (\omega t + \phi_{out})]. \quad (3.3\text{-}3)$$

It is possible to determine the amplitude and phase of the system output for a given set of system parameters. This technique is similar to the *describing function* method to analyze the effect of system nonlinearities on sinusiodal input waveforms. In the case presented here, the input signal form is known, and the amplitude and phase of the system for given parametersis also known. It follows that the output amplitude and phase can be determined.

44
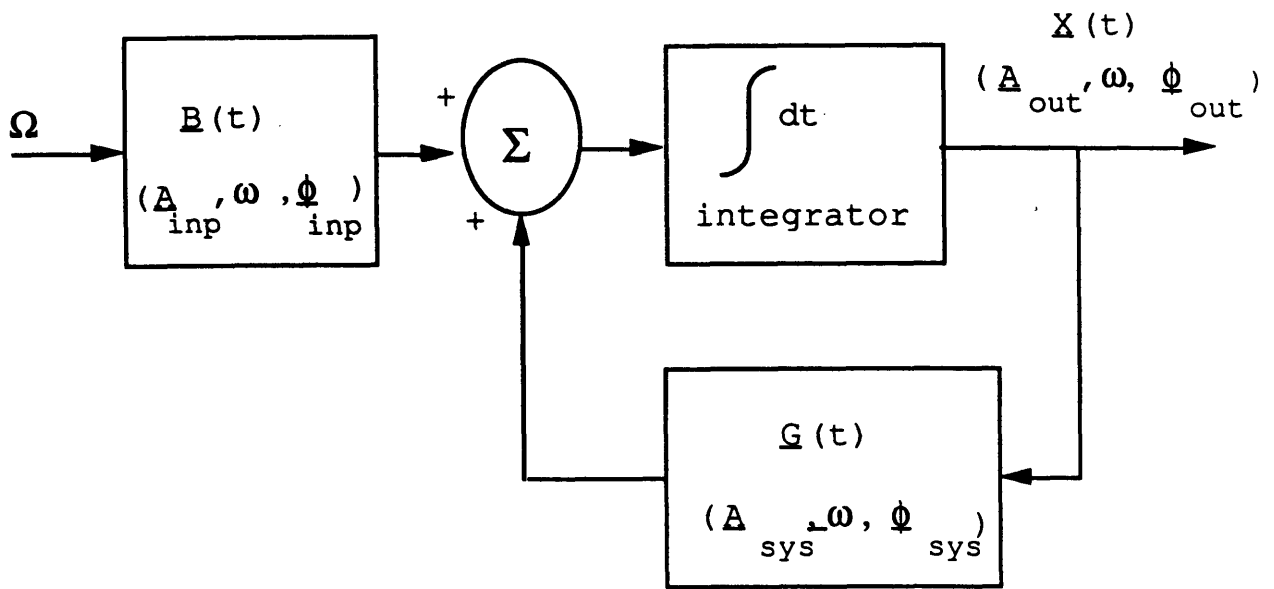
Figure 3.2 Periodically Forced System

The output waveform can be expanded in a Fourier series.

$$x_1(t) = A_{11}\left(\sin \omega t + \phi_{11}\right) = a_0 + \sum_{n=1}^{\infty} a_n \sin n\omega t + \sum_{r=1}^{\infty} b_r \cos r\omega t$$

(3.3-4)

This representation for the output θ (t) can then be substituted into the equation of motion in the form of Eqn. (3.1-1) to determine the Fourier coefficients. This technique to determine the amplitude and phase of an output signal is known as *harmonic balance*. The derivatives are

$$\dot{\theta}(t) = \sum_{n=1}^{\infty} a_n n\omega \cos n\omega t - \sum_{r=1}^{\infty} b_r r\omega \sin r\omega t$$

$$\ddot{\theta}(t) = -\sum_{n=1}^{\infty} a_n n^2\omega^2 \cos n\omega t - \sum_{r=1}^{\infty} b_r r^2\omega^2 \sin r\omega t .$$

Substituting,

45

$$-(1 + \varepsilon \sin wt)\left(\sum_{n=1}^{\infty} a_n \, n^2\omega^2 \, \sin n\omega t + \sum_{r=1}^{\infty} b_r \, r^2\omega^2 \cos r\omega t\right) + \left(\frac{\omega}{Q} + \varepsilon\omega \cos \omega t\right) \bullet$$

$$\left(\sum_{n=1}^{\infty} a_n n\omega\cos n\omega t - \sum_{r=1}^{\infty} b_r r\omega\sin n\omega t\right) + \omega^2\left(a_0 + \sum_{n=1}^{\infty} a_n\sin n\omega t + \sum_{r=1}^{\infty} b_r\cos r\omega t\right) = -\Omega\varepsilon\omega \cos \omega t \ .$$

$$(3.3\text{-}5)$$

To simplify Eqn. (3.3-5) it is necessary to recall the following trigonometric identities:

$$\sin \alpha \sin \beta = \frac{1}{2}\cos(\alpha - \beta) - \frac{1}{2}\cos(\alpha + \beta)$$

$$\cos \alpha \cos \beta = \frac{1}{2}\cos(\alpha - \beta) + \frac{1}{2}\cos(\alpha + \beta)$$

$$\sin \alpha \cos \beta = \frac{1}{2}\sin(\alpha + \beta) + \frac{1}{2}\sin(\alpha - \beta) \qquad (3.3\text{-}6)$$

Using these identities, the left hand side of Eqn. (3.4-5) is simplified and expanded into an infinite summation of even and odd harmonics. By equating the coefficients of the various harmonics, an infinite string of equations in terms of the system parameters and the Fourier coefficients is obtained. The first five such equations are given by,

constant: $\quad a_0 = 0.$

$\sin \omega t$: $\quad -\dfrac{\omega^2}{Q}b_1 + (2\varepsilon\omega^2 - \varepsilon\omega)b_2 = 0.$

$\cos \omega t$: $\quad \dfrac{\omega^2}{Q}a_1 - (2\varepsilon\omega^2 - \varepsilon\omega)a_2 = -\Omega\varepsilon\omega.$

$\sin 2\omega t$: $\quad -\varepsilon\omega^2 b_1 - 3\omega^2 a_2 - \dfrac{2\omega^2}{Q}b_2 + (\dfrac{9}{2}\varepsilon\omega^2 - \dfrac{3}{2}\varepsilon\omega)b_3 = 0.$

$\cos 2\omega t$: $\quad \varepsilon\omega^2 a_1 + \dfrac{2\omega^2}{Q}a_2 - 3\omega^2 b_2 - (\dfrac{9}{2}\varepsilon\omega^2 - \dfrac{3}{2}\varepsilon\omega)a_3 = 0. \qquad (3.3\text{-}7)$

The equations proceed such that only four terms are present in each equation. A general form is noted such that for the jth harmonic the two equations are

$\sin j\omega t$: $\quad -\dfrac{(j-1)^2}{2}\varepsilon\omega^2 b_{j-1} - (j^2 - 1)\omega^2 a_j - \dfrac{j\omega^2}{Q}b_j +$

$$[\dfrac{(j+1)^2}{2}\varepsilon\omega^2 - \dfrac{(j+1)^2}{2}\varepsilon\omega]b_{j+1} = 0, \text{ and}$$

$\cos j\omega t:$
$$\frac{(j-1)^2}{2} \varepsilon \omega^2 \, a_{j-1} \; - \; (j^2 - 1)\omega^2 \, b_j \; + \frac{j\omega^2}{Q} \, a_j \; -$$

$$[\frac{(j+1)^2}{2} \varepsilon \omega^2 \; -\frac{(j+1)^2}{2} \varepsilon \omega] \, a_{j+1} \; = \; 0. \qquad (3.3\text{-}8)$$

The exception to the generalization is that for the cos ωt equation the forcing term on the right hand side is the gyroscopic torque, $-\Omega \varepsilon \omega$.

The sequence of equations can be written in terms of infinite matrices,

$$\mathbf{C} \, \mathbf{x} \; = \; \mathbf{f} \qquad\qquad \text{where,}$$

$$\begin{bmatrix} 0 & \frac{\omega^2}{Q} & 0 & \cdots \\ \frac{\omega^2}{Q} & 0 & -2(\varepsilon\omega^2 - \varepsilon\omega) & \cdots \\ 0 & -\varepsilon\omega^2 & -3\omega^2 & \cdots \\ \vdots & \vdots & \vdots & \ddots \end{bmatrix} \begin{bmatrix} a_1 \\ b_1 \\ a_2 \\ \vdots \end{bmatrix} = \begin{bmatrix} 0 \\ \varepsilon \Omega \omega \\ 0 \\ \vdots \end{bmatrix}$$

$$(3.3\text{-}9)$$

It is not possible to exactly determine the values of the Fourier coefficients. But, as previously shown, the system is stable for a specified region of the parameters. Any periodic input applied to the system will result in a stable, periodic output. Then, it is necessary for the Fourier series to converge and the coefficients, a_n and b_n, tend to zero for large n. The infinite matrices can then be truncated at a sufficiently large dimension by neglecting infinitesimal Fourier coefficients. The corresponding finite matrix is

$$\mathbf{x}_f \; = \; [\, a_1, b_2, a_2, \ldots, b_m]^T \qquad \text{where m is the number of}$$

significant harmonics in the solution. The resulting finite matrix equation can be solved where,

$$\mathbf{x}_f \; = \; \mathbf{C}_f^{-1} \, \mathbf{f}_f . \qquad (3.3\text{-}10)$$

It is desireable to obtain an expression relating the Fourier coefficients to the system parameters, ω, ε, and Q. This would give system design guidelines necessary to keep the quadrature and higher harmonic components of the output small. However, the existence of

the matrix inversion makes it practically impossible to obtain an analytical expression for the Fourier coefficients. Hence, numerical solutions must be obtained for the truncated matrisx equation (3.3-10) for different parameter values to obtain quantitative relationships.

First, a set of preliminary design parameters that are within the stability region is chosen where,

$$\omega = 6000 \text{ rad/sec} \quad Q = 2000 \quad \text{and} \quad \varepsilon Q = 1.0 \, .$$

Substituting these values into a 10 X 10 dimensional form of Eqn. (3.3-9), the solutions are

$$a_1 = -1.7 \text{ E-3} \qquad b_1 = -5.6 \text{ E-7}$$

$$a_2 = 1.85 \text{ E-10} \qquad b_2 = -2.8 \text{ E-7}$$

$$a_3 = 3.4 \text{ E-11} \qquad b_3 = 2.9 \text{ E-14}$$

$$a_4 = 5.1 \text{ E-18} \qquad b_4 = 5.2 \text{ E-15}$$

$$a_5 = -8.6 \text{ E-19} \qquad b_5 = -9.4 \text{ E-22}$$

It is encouraging to observe that the magnitude of the in-phase component (a_1) at the driving frequency is equal to $\dfrac{\varepsilon Q}{\omega}$. This is the magnitude of the pure sine output that was determined by neglecting the periodic terms as shown in section 2.5. Also, the Fourier series converges rapidly. All terms greater than the second harmonic appear negligable. It is thus adequate to approximate the matrix equation (3.3-9) by a 4X4 dimensional matrix equation. This assumption loses its validity for large values of εQ since system instability could lead to a diverging Fourier series.

But, assuming that all terms greater than the second harmonic are negligable, values for a_1, a_2, b_1, and b_2 can be determined for a wide range of system parameters. Numerical results are obtained for values of the stability parameter from $\varepsilon Q = 0.3$ to $\varepsilon Q = 30$, and for values of the system quality factor ranging from $Q = 200$ to $Q = 1000$. Different values for the system frequency were inputted, but , for a fixed Q and ε the Fourier coefficients were

48

invariant to system frequency. The results are plotted in Figure 3.3, and a frequency $\omega = 1$ kHz was used throughout.

The figure shows the phase shift of the first harmonic versus the stability parameter. The phase shift is defined such that a 90 degree shift results in a pure cosine component, and a zero degree shift is a pure sine component. Results for three different values of the system quality factor are plotted, with $Q = 200$ as a minimum and $Q = 1000$ as a maximum. The ratio of the second cosine harmonic to the first sine harmonic is also plotted. For all cases run, the cosine phase of the second harmonic was significantly greater in magnitude than the sine component. Hence, this plot gives information on the magnitude of higher harmonic oscillations compared to the oscillations at the system frequency. The third plot shows the ratio of the first sine harmonic to the estimated value of the output obtained from neglecting the periodic terms. The estimated value is given by Eqn. (2.4-5).

The numerical results to the Fourier coefficients yield useful relationships between the system parameters and the actual response. A number of conclusions can be reached and they are listed as follows:

1)   The Fourier series converges within four terms in the esitmated stability range $\epsilon Q < \sqrt{12}$.

2)   The only significant higher harmonic term that is excited is the second even harmonic ($b_2 \cos 2\omega t$). However, this term is less than 1% of the first odd harmonic in the estimated stability range, and only increases to 3% at $\epsilon Q = 30$. Hence, all higher harmonic terms in the output can be accurately neglected. The small magnitude of higher harmonic oscillations that does exist is eliminated by filtering the output signal.

3)   For $\epsilon Q < 4$, the forced system output at the first odd harmonic ($\sin \omega t$) is exactly the output estimated form neglecting the periodic terms in the equation of motion.

first harmonic phase shift vs. stability parameter
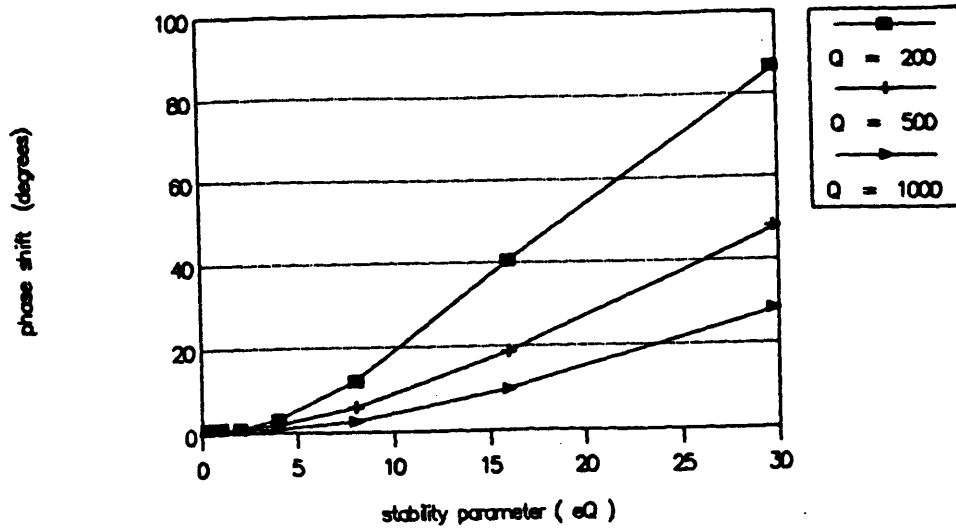
ratio of second cosine harmonic to first sine harmonic, vs. eQ
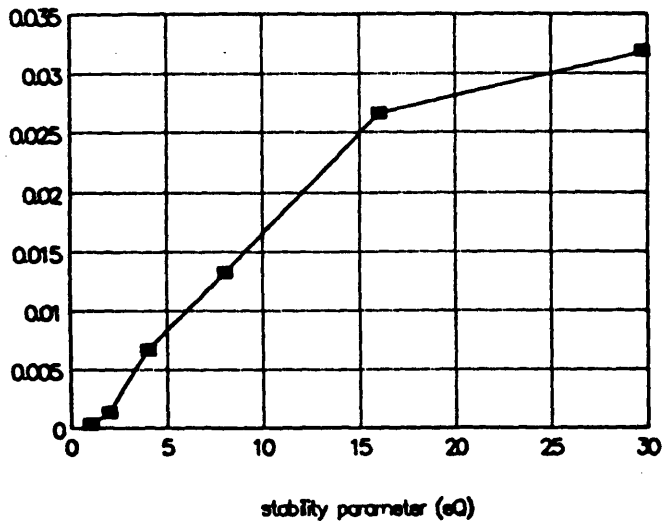
ratio of first sine harmonic to time invariant approximation
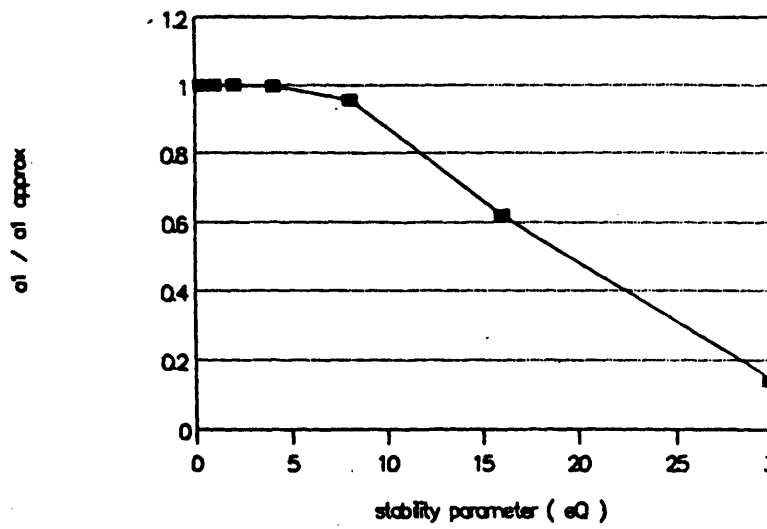
Figure 3.3   Numerical Results for Harmonic Balance Fourier Coefficients

50

For $4 < \varepsilon Q < 8$, the sine component decreases at a nearly linear rate. Therefore, for a system designed within the estimated stability range, the in-phase output is accurately predicted from the linear simplified theory,

$$a_1 = \frac{\Omega \varepsilon Q}{\omega}.$$

4)   The output phase shift increases with the magnitude of the system damping.

5)   Within the estimated stability range, the phase shift is less than 3 degrees for a system with minimum $Q = 200$. For $\varepsilon Q > 5$, the phase shift increases fairly rapidly. This small quadrature component can be easily eliminated by demodulation.

3.4   Numerical Simulation

The analytical results of the previous three sections have all included some degree of approximation. To gain increased confidence in the behavior of the periodic system, the equations of motion are solved numerically. The role of the simulation is to *reinforce the analytical results*. All too often, simulation is relied upon to provide the bulk of information on the behavior of a particular dynamic system. For the dynamic system presented in this paper, the high frequency nature renders it difficult to reach conclusive results from a simulation alone. Very small step-sizes and a very large number of steps are needed to solve the equations for a significant period of time. This requires excessive computation and magnifies the effect of truncation and round-off errors.

But, the simulation is useful in a few regards. The simulation response can be compared to the estimated sinusoidal response of Eqn. (2.4-5), and it can also be compared

to the response determined by harmonic balance. The specific roles that the simulation fills are listed below:

1) To check for non-periodic behavior.

2) To check the system time constant and transient response.

3) To determine the output oscillation magnitude and period for different parameters.

4) To compare the simulated response to the estimated response.

The simulation integrates the state space form of the equations of motion given by Eqn. (3.3-1), initially at rest where,

$$\theta = \frac{d\theta}{dt} = 0, \text{ at } t = 0.$$

The simulation is written in PASCAL programming language and uses a fourth order Runge-Kutta integration algorithm. A Runge-Kutta algorithm is chosen because of its programming ease compared to finite difference methods. Also, step-size changes can be easily implemented into this method. The Runge-Kutta algorithm is based on matching a Taylor series expansion about an initial point, for each of the state variables, to a polynomial written in terms of the initial values, the stepsize, and the functions representing the derivatives of the state variables. The coefficients of the polynomial are chosen such that a minimum number of functional evaluations are necessary per step. The fourth order Runge-Kutta algorithm, as given by Battin [14], is

$$x = x_0 + \frac{1}{6}h(k_0 + 2k_1 + 2k_2 + k_3) + O(h^5)$$

$$k_0 = f(t_0, x_0)$$

$$k_1 = f(t_0 + \frac{1}{2}h, x_0 + \frac{1}{2}h k_0)$$

$$k_2 = f(t_0 + \frac{1}{2}h, x_0 + \frac{1}{2}h k_1)$$

$$k_3 = f(t_0 + h, x_0 + h k_0)$$

where, $\frac{dx}{dt} = f(t, x)$, $x(t_0) = x_0$, and $t - t_0 = h$.

52

It is difficult to choose a fixed value for the step-size, h, to integrate the tuning fork equations of motion. Since the system oscillates at high frequency, a step-size chosen too large could lead to a divergent algorithm, and a step-size chosen too small leads to an excessive number of iterations. For this reason, an adaptive step-size procedure is added to the simulation program. Since the algorithm makes functional evaluations at the step midpoint, it is convenient to measure the truncation error by comparing the numerical estimates obtained form one step size of 2h (call it x_1), and that obtained from using two steps of size h each (call this estimate x_2). This error, Δ, is on the order of h^5 since the algorithm is fourth order. The desired accuracy is defined as Δ_0, where

$$\Delta = |x_2 - x_1| \quad \text{and}$$

$$\Delta_0 = \varepsilon_h (y_{max}) \quad \text{where,}$$

$$y_{max} = \text{amplitude of oscillation}$$

$$\varepsilon_h = 0.001.$$

The desired accuracy is defined such that the truncation error is always less than 0.1% of the oscillation amplitude. The procedure appropriately scales the step-size at each iteration such that it is at a maximum value that remains within the error limits. A copy of the simulation source code is given in Appendix A.

The program is run by interactively entering the system parameters, a specified transient time, and the number of periods for the stored data. The program integrates up to the specified transient time without storing data, and then stores data for the specified number of periods. The discrete data for the output angle and angular velocity, as a function of time, is printed in tabular form. In addition, the oscillation amplitude and period, the number of iteration steps, and the ratio of the simulated amplitude to the estimated amplitude of Eqn. (2.4-5), are also recorded. The program is run on an IBM PC using the Turbo Pascal compiler developed by Borland International, Inc.

The simulation data gives the approximate system response for different sets of parameter values. The discrete data for the output angle is presented in graphical form which

is compared to the estimated sinusoidal output. Simulations are performed for various values of ε and Q, and at a frequency of 1 kHz. For all cases, the input to the system is a unit step with magnitude Ω = 1.0 rad/sec.

First, simulations are run for various values of the quality factor, Q, while also varying the transient time input. This determines the time period necessary for the output to reach a steady state oscillation. The value of the system time constant, T_c, is then determined. For a second order system, the time constant is defined [33] as the time at which the output reaches 63% of its steady state value, assuming the system is initiated at time, t = 0. Figure 3.4 plots the ratio of the simulated time constant to the estimated time constant from Eqn. (2.5-6) as a function of the stability parameter, εQ. The estimated time constant is given as

$$T_{c,est} = \frac{2Q}{\omega} .$$

In order to check the simulated system response against the estimated linear response from Eqn. (2.4-5) and against the harmonic balance prediction from Figure 3.3, three simulation runs are presented here. The system quality factor is fixed at Q = 200, which represents an acceptable design value, and the frequency is fixed at 1 kHz. The data is recorded after an allowed transient period of 6 seconds, which well exceeds the system transient period. The three cases are

1) εQ = 1.0   within estimated stability region.

2) εQ = 4.0   near estimated stability boundary.

3) εQ = 16.0   exceeding estimated stability limit.

The results are shown in Figures 3.5 - 3.10. The phase plane plots give a visualization of the periodic nature of the output. In the figures, the simulated output is compared with the estimated sinusoidal output. It is also compared to the first harmonic oscillation curve obtained by using the Fourier coefficients of the preceding section. The first

two plots show an almost exact correspondence between the three predicted response curves. However, the three curves deviate in the third plot. For the parameter values of this case, which exceed the estimated stability region, the periodic terms in the equation of motion result in a substantial phase shift. It appears from the plot that the phase shift is nearly that predicted by the harmonic balance,

$$\phi_{pred} = 0.71 \text{ radians}.$$

However, the simulated oscillation magnitude exceeds the harmonic balance prediction magnitude by 24 %. The discrepancy is probably due to errors in evaluating the Fourier coefficients for a system with a large stability parameter by a 4X4 matrix. As discussed in Section 3.3, the 4X4 truncation is only valid for small values of the stability parameter where the Fourier series converges rapidly.

The simulation leads to the following conclusions:

1) The periodic terms do not significantly affect the system transient response, as seen from Figure 3.4.

2) When the stability parameter is within the estimated stability limit, the system output is accurately approximated by the sinusiodal response of Eqn. (2.4-5). This is seen from Figures 3.5 and 3.7.

3) For values of the stability parameter exceeding the estimated stability limit, the output magnitude decreases and a phase shift occurs, as seen form Figure 3.9.

4) The phase shift that ocurs for high values of ϵQ is approximately that predicted by the harmonic balance. However, the magnitude of oscillation for high values of ϵQ is greater than that predicted by harmonic balance, as seen in Figure 3.9.

5) The simulated responses are all periodic with period, $T = \dfrac{2\pi}{\omega}$.

55

Ratio of Sim. Time Const. to Estimated Time Const. vs. Stab. Parameter
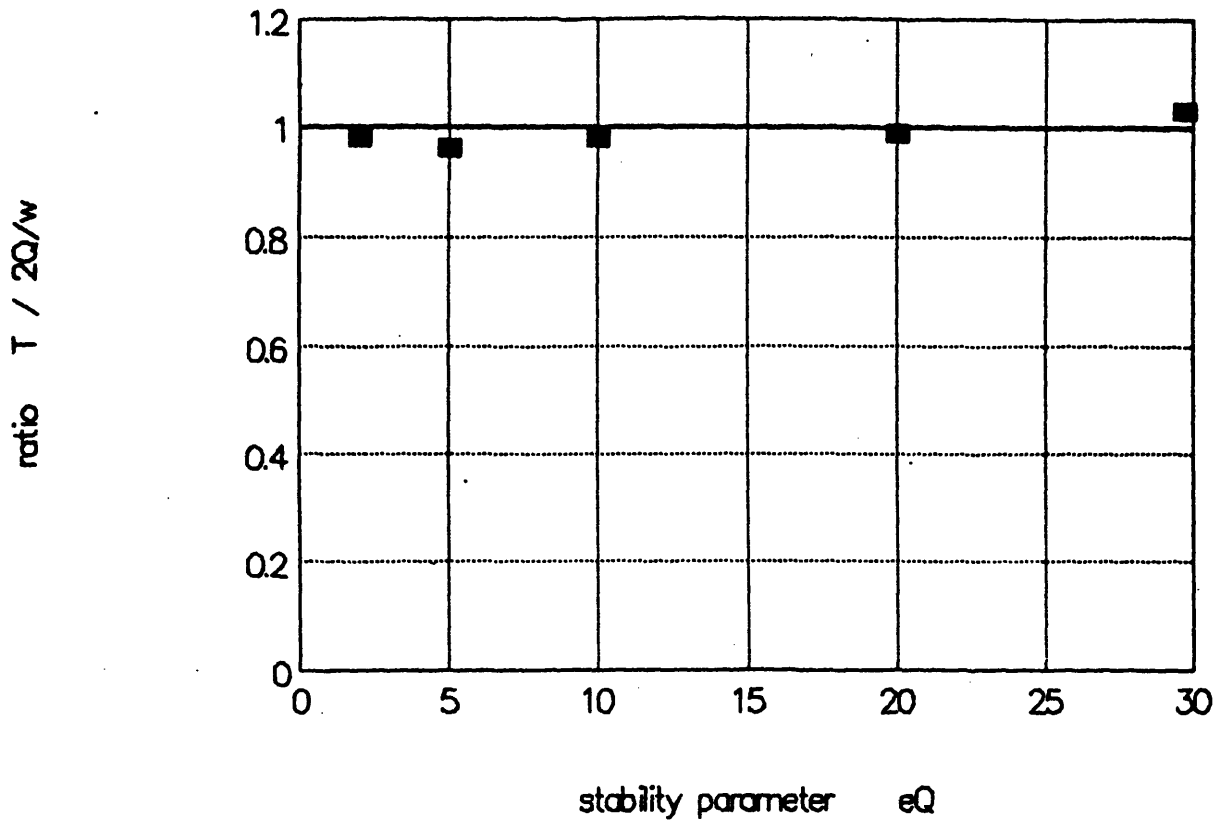
Figure 3.4   Simulation Results For System Time Constant
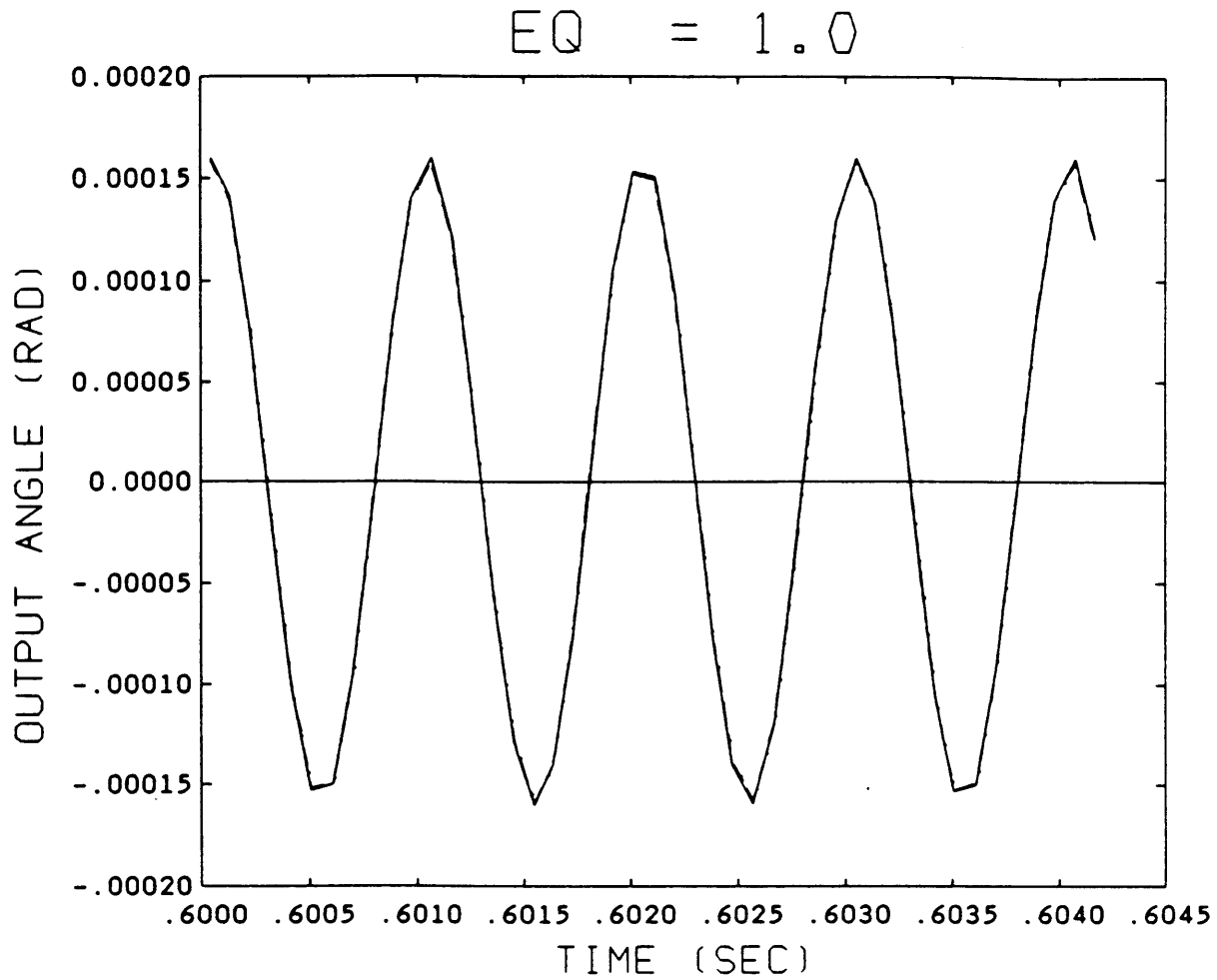
Figure 3.5   Simulation results for $\varepsilon = 0.005$ $Q = 200$ $\omega = 1 \text{ kHz}$

εQ = 1.0
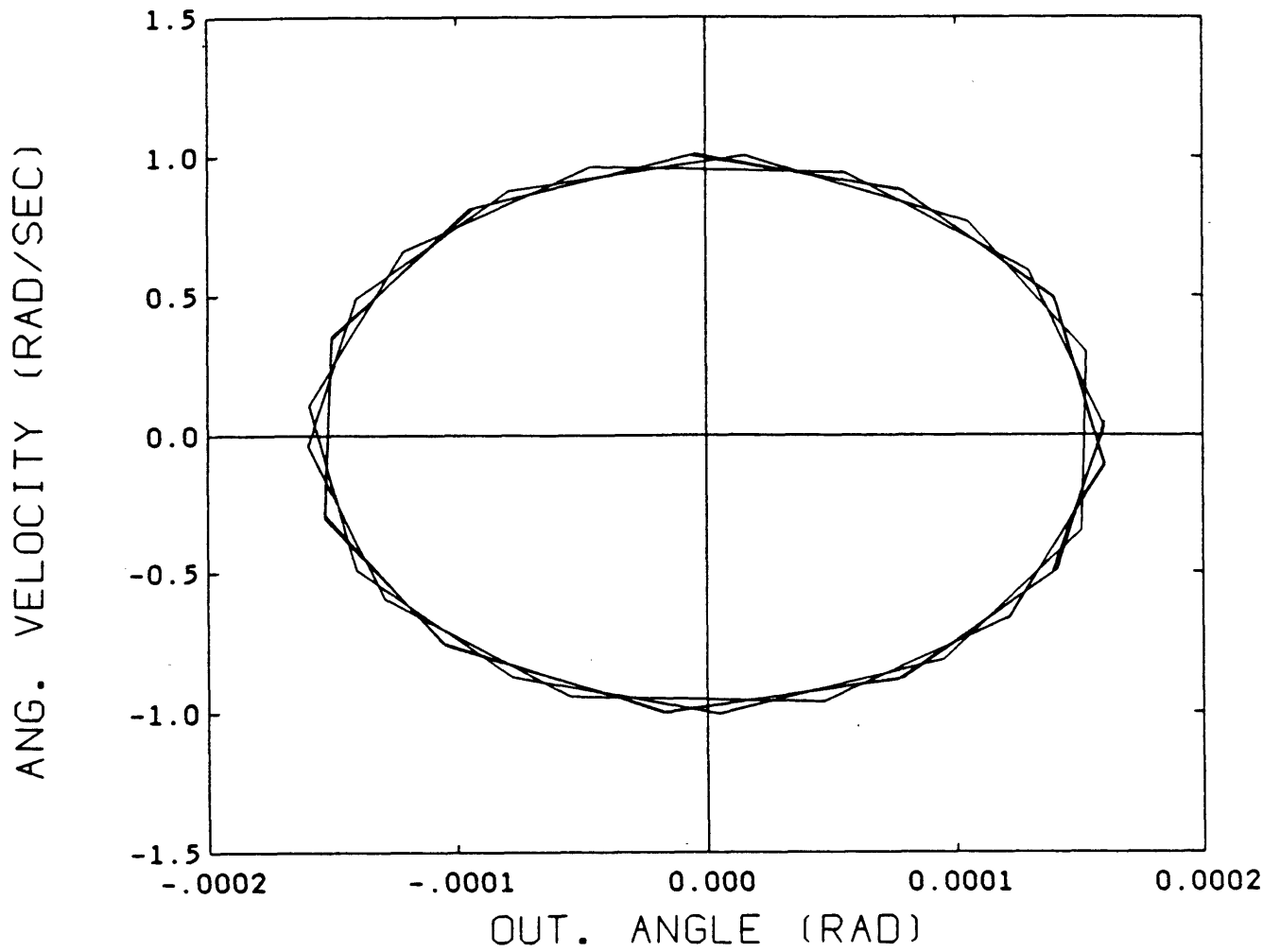
Figure 3.6   Phase Plane Plot for   ε = 0.005   Q = 200   ω = 1 kHz

EQ = 4.0
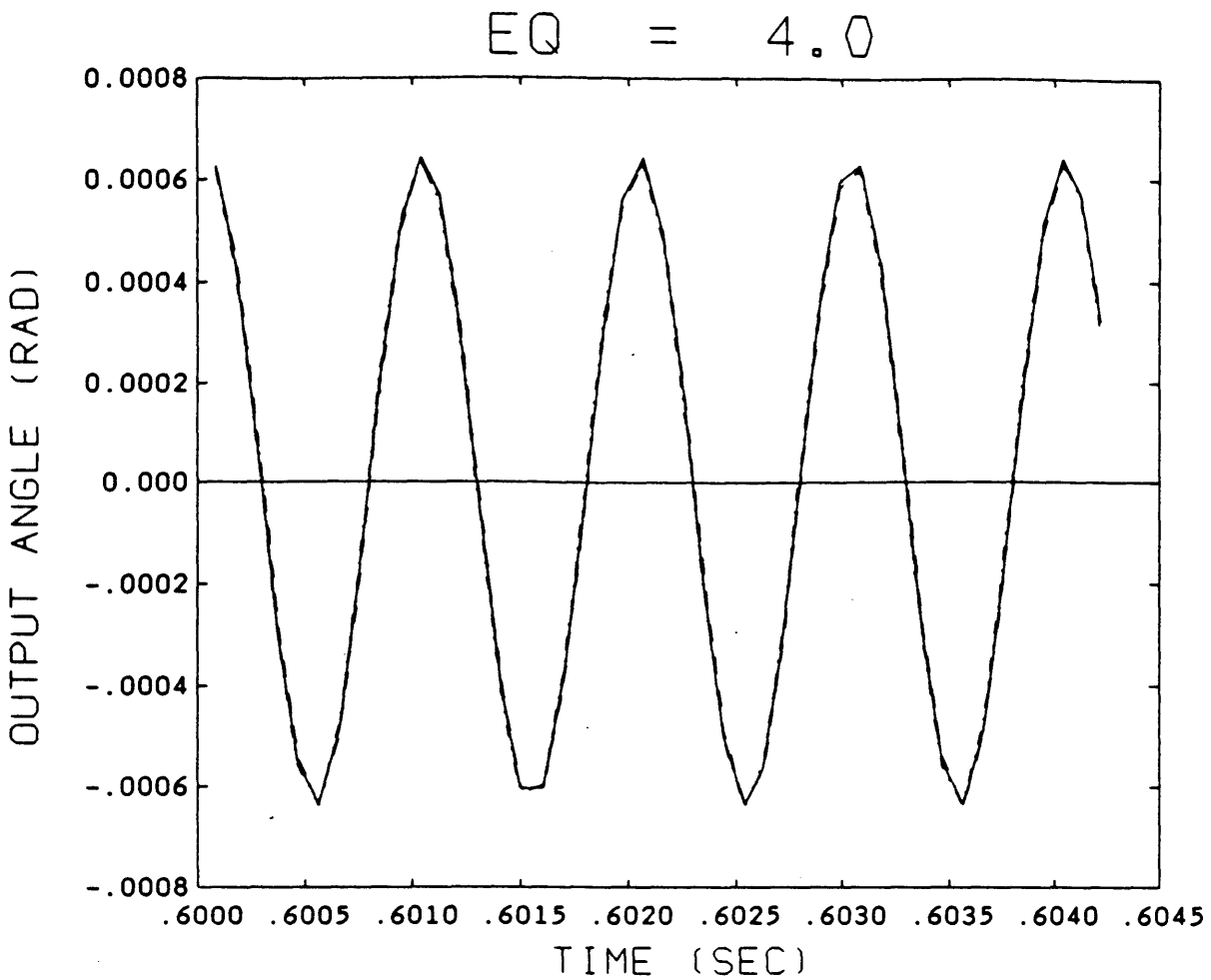
simulated response, θ_{max} = 0.000644 radians.

estimated response from neglecting periodic terms, θ_e = 0.000637 sin (ωt).

predicted response from harmonic balance, θ_{hb} = 0.000638 sin (ωt + 0.053).

Figure 3.7   Simulation results for ε = 0.02   Q = 200 ω = 1 kHz

$$\epsilon \, Q \quad = \quad 4.0$$
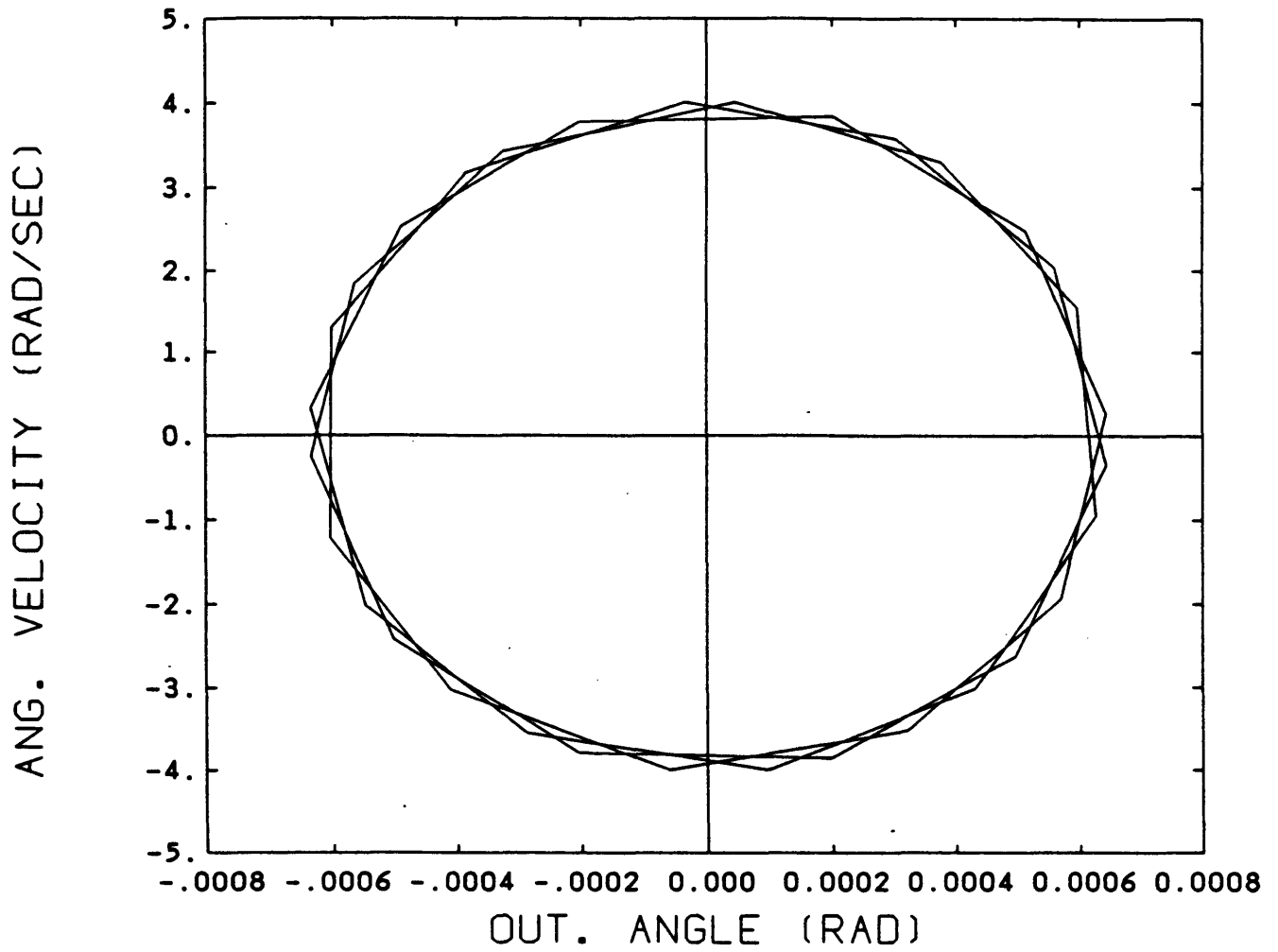
Figure 3.8   Phase Plane Plot for $\epsilon = 0.02$ $Q = 200$ $\omega = 1 \, kHz$

EQ = 16.0
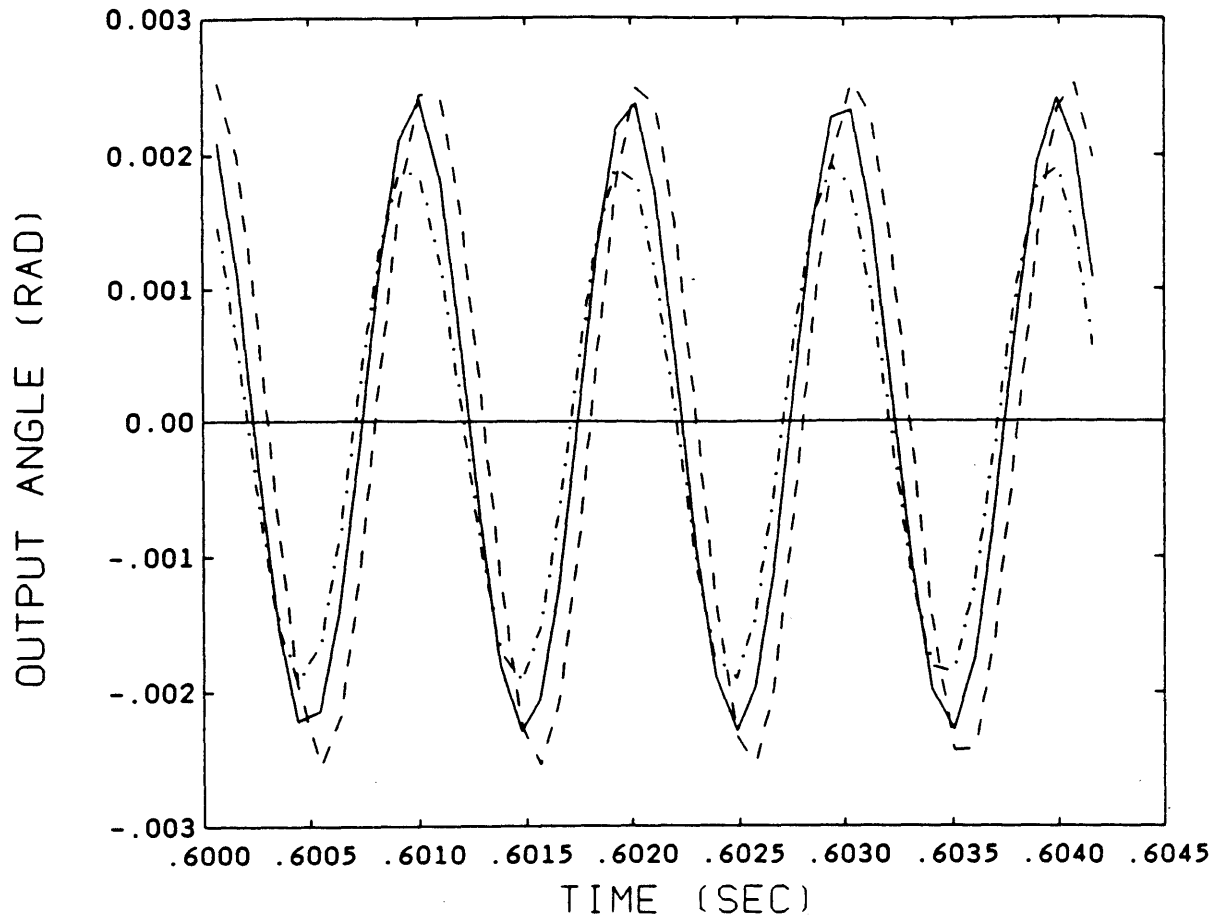
simulated response, θ_{max} = 0.002413 radians.

estimated response from neglecting periodic terms, θ_e = 0.002548 sin (ωt).

predicted response from harmonic balance, θ_{hb} = 0.00194 sin (ωt + 0.71).

Figure 3.9   Simulation results for ϵ = 0.08   Q = 200 ω = 1 kHz

$$\varepsilon\,Q \quad = \quad 16.0$$
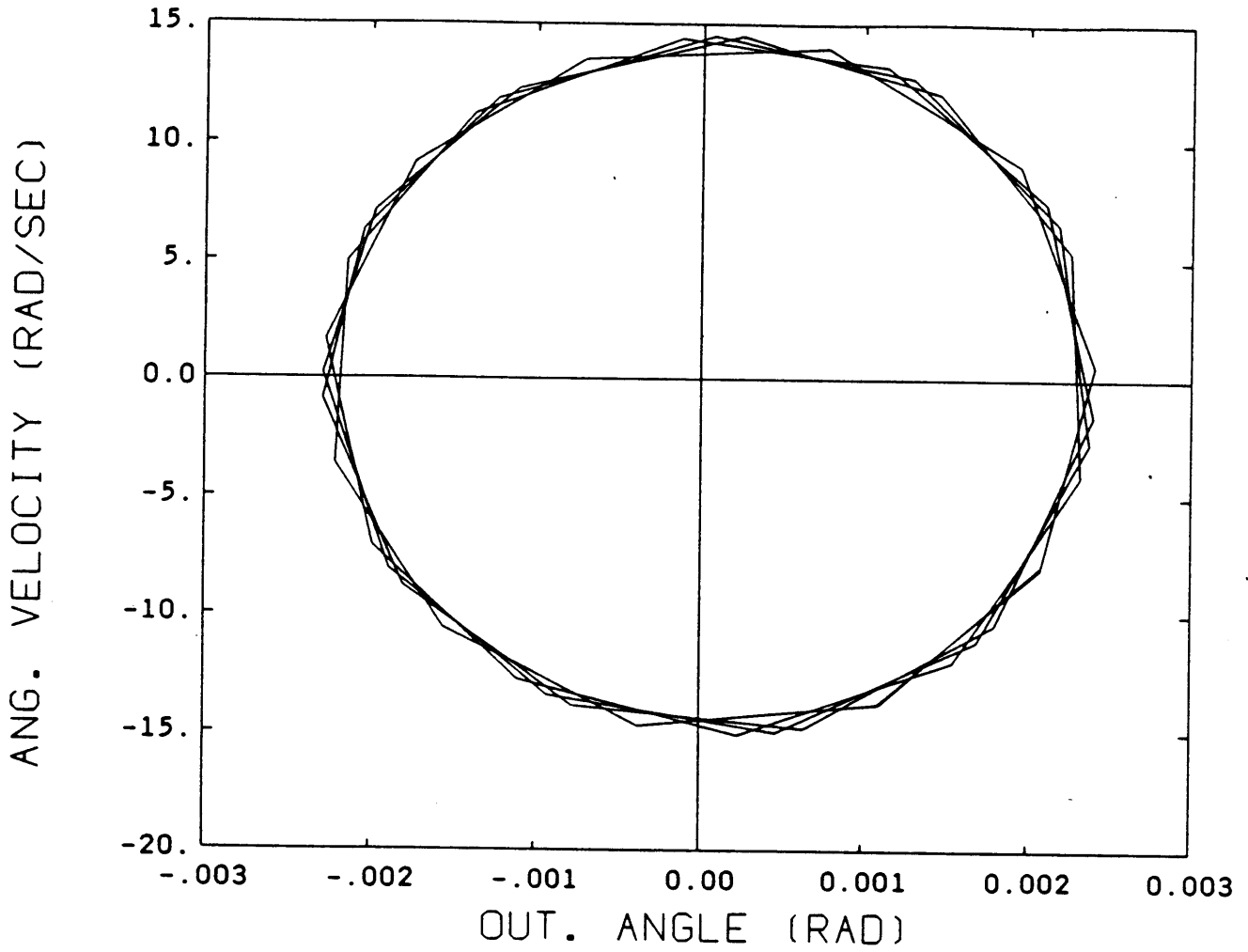
Figure 3.10   Phase Plane Plot for $\varepsilon = 0.08$ Q = 200 ω = 1 kHz

3.5 Stability in Terms of Floquet Theory

The simulation results are encouraging. They verified that within the estimated stability region, the gyroscopically forced output is accurately approximated by neglecting the periodic terms in the equation of motion. However, the simulation results *can not* be used to verify that the system is indeed stable. It is possible that an unstable system can have a periodic output, that does not appear to grow with time, if it is forced periodically [11]. Since the gyroscopic torque is periodic, an alternate means for verifying the stability of the system is necessary.

The most common method of determining the stability of an LP system is the use of Floquet Theory. The celebrated *Floquet Theorem* states that if the solution to a periodic differential equation is known for one period, then it is known for all time. The Floquet Theorem is also expressed in Eqn. (3.2-9) which shows that the solution to a periodic equation is related to the solution one full period away by a complex constant. The state space form of the tuning fork equation of motion (3.3-1) can be written in terms of a *state transition matrix* ,

$$\underline{x}(t) = \underline{\Phi}(t,t_0) \, \underline{x}(t_0) \quad \text{where,} \tag{3.5-1}$$

$$\frac{d}{dt}\underline{\Phi}(t) = \underline{G}\,\underline{\Phi}(t,t_0) \quad \text{and} \quad \underline{\Phi}(t_0,t_0) = \underline{I} \, . \tag{3.5-2}$$

Because of the Floquet Theorem (3.2-9), a *discrete transition matrix* can be defined which describes the solution at discrete points sampled every period, T, from an initial point $\underline{x}(0)$,

$$\underline{x}(T) = \underline{\Phi}(T)\,\underline{x}(0) \quad \text{and}$$

$$\underline{x}(kT) = \underline{\Phi}^k(T)\,\underline{x}(0) \quad \text{where} \quad \underline{\Phi}(T) = \underline{\Phi}(T,0) = \underline{\Phi}(t+T,t). \tag{3.5-3}$$

Eqn. (3.5-2) indicates that the solution to LP systems can be written in discrete-time form. The stability criteria for a system of this form depends on the eigenvalues of the discrete transition matrix, and is written as a theorem [11].

Theorem 3.1:

The natural response of a periodically time-varying system is stable if and only if no eigenvalues of the discrete transiton matrix have magnitudes greater than one and that an eigenvalue with unity magnitude is not degenerate.

However, it is not trivial to determine the discrete transition matrix that satisfies Eqn. (3.5-1) for the plant matrix, $\underline{G}$, defined in Eqn. (3.3-1). The most convenient method for determining $\underline{\Phi}$ (T) is to numerically integrate Eqn. (3.3-2) for a given plant matrix. Then the calculated eigenvalues of the state transition matrix can be used to check the stability of the system for a given set of parameters. But, instead of implementing another numerical integration scheme for Eqn. (3.3-2), the simulation of the previous section can be used to obtain the same information.

The homogeneous equation of motion is integrated with the initial conditions perturbed from equilibrium. Then, sampling the output at integer multiples of the period gives information about the placement of the discrete transition matrix eigenvalues. If the output for both states decreases in magnitude each period, then the eigenvalues have magnitude less than unity. On the other hand, if the output increases in magnitude for either state, one of the eigenvalues has magnitude greater than one.

The initial conditions are perturbed from a state of rest such that,

$$\theta (0) = 0.05 \text{ radians, and } \frac{d}{dt}\theta (0) = 0.1 \text{ rad/sec.}$$

The system parameters ε and Q are varied, and the discretely sampled output for the perturbed system is recorded. For all values of the stability parameter within the estimated stability range, the eigenvalues are concluded to have magnitude less than unity. A plot of the

64

discrete output for $\varepsilon Q = 4.0$ is shown in Figure 3.11. Moreover, the system was checked

for robustness, and values up to $\varepsilon Q = 30.0$ displayed stable responses.

response to initial value perturbation

at eQ = 4.0
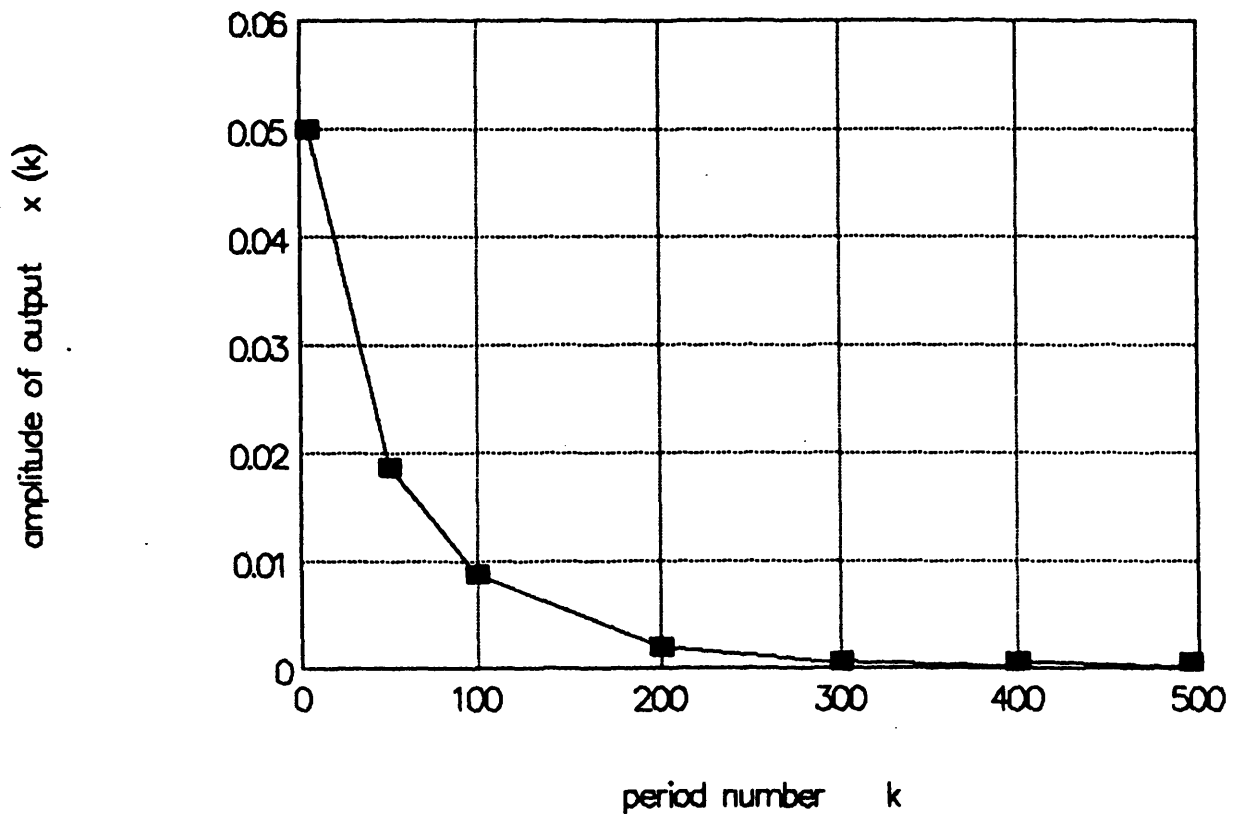
Figure 3.11   Response to Initial Value Perturbation for

$\varepsilon = 0.02$, $Q = 200$, and $\omega = 1$ kHz

4   SYSTEM MATHEMATICAL MODEL

The process used to design the micromechanical tuning fork gyroscope is
illustrated in Figure 4.1. The goal is to develop a reasonable design and a
corresponding set of performance predictions. The design is classified as a *baseline
design*. This means that it represents a starting point for the development of a
micromechanical tuning fork instrument, and not necessarily the exact design for a first
prototype. The performance predictions are used to evaluate the potential of the device
as an angular rate sensor. It is important to note that the performance predictions are
only analytical approximations. They are intended only to be accurate enough to make
conclusive comparisons with similar angular rate sensors.

The first two chapters of this paper provided the *concept demonstration* and
preliminary configuration steps in the design process. Chapters 2 and 3 served to
analyze the system dynamics. An appropriate linear model for the gyroscope sensitivity
was derived, and verified, for a given range of the system parameters. The next step is
to develop a thorough mathematical model of the system. The model relates the device
dimensions and input parameters such as driving voltage, frequency, temperature, and
pressure, to the gyroscope performance. The performance of the device includes the
sensitivity to an applied angular rate about the sensitive axis, the mechanical limitations,
robustness, electrical output, damping levels, and identified error levels. By
thoroughly modeling the system, a feasible design can be produced by varying the
dimensions and input parameters until a suitable performance level is obtained.
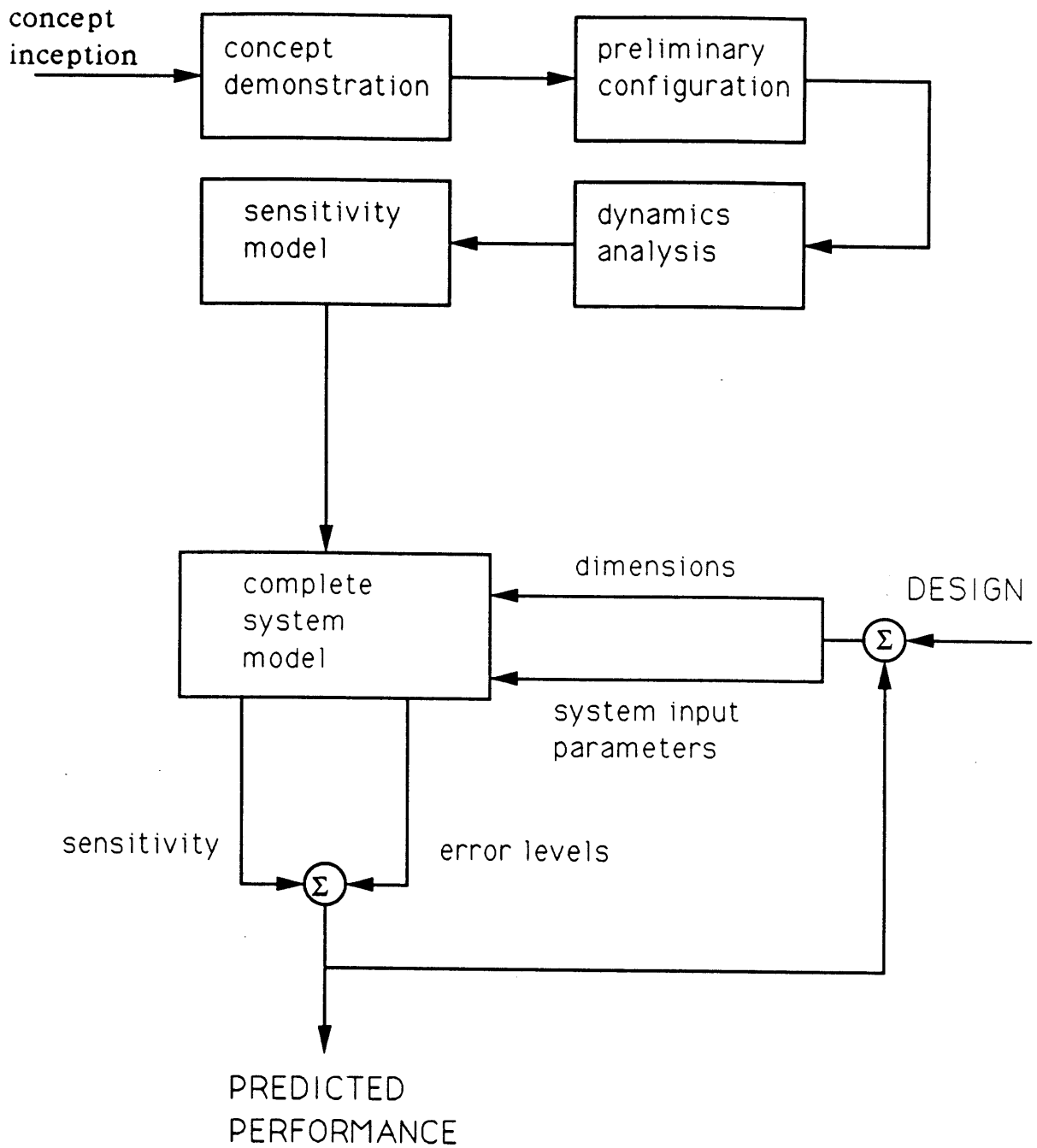
Figure 4.1   Design Process

4.1   Motor Model

The gyroscope motor consists of the two tines, the two attached proof masses, and the electronics which apply a voltage across the tines. The mathematical model of the motor relates the mechanical gain, ε, to the applied driving voltage, as shown in Figure 4.2. The first step in developing the model is to determine the electrostatic force which vibrates the tines as a function of the applied voltage.

It is clear that the tines cannot be accurately modeled as two parallel plate capacitors. The width of the tines is not negligable compared to the height . The applied voltage causes a uniform charge density to accumulate along the top and bottom (x-y plane) of the tines. Electric flux is radiated from this area and a fringing electric field is produced, as shown in Figure 4.2. The fringing flux adds to the parallel flux radiated form the inside of the tines to produce a electrostatic force between the tines. For the parallel plates alone, the force between the tines is determined by differentiating the electric energy with respect to the gap distance. The expression for the force is given [15] as,

$$F_1 = \frac{\varepsilon_0 A_1 V_d^2}{2 d^2} \quad \text{where},$$

(4.1-1)

$A_1 = hL$ area of inside of tines

$\varepsilon_0 \equiv$ permittivity of the gap air .

The electrostatic force due to the fringing electric flux is not determined as easily because the flux is not one-dimensional. The problem is to determine the capacitance between two flat plates lying in the same plane as a function of the plate dimensions. The electric energy can then be determined which is differentiated to give the electrostatic force.

68

Vd

driving voltage

motor model

ε

mechanical gain

y

z

x

gap between tines

d

width of tines

w

height of tines

h

length of tines

L

tine vibration

Ψp

electric flux lines Ψp, from parallel plates

Ψf

electric flux lines Ψf, from fringing

Vd sin ωt
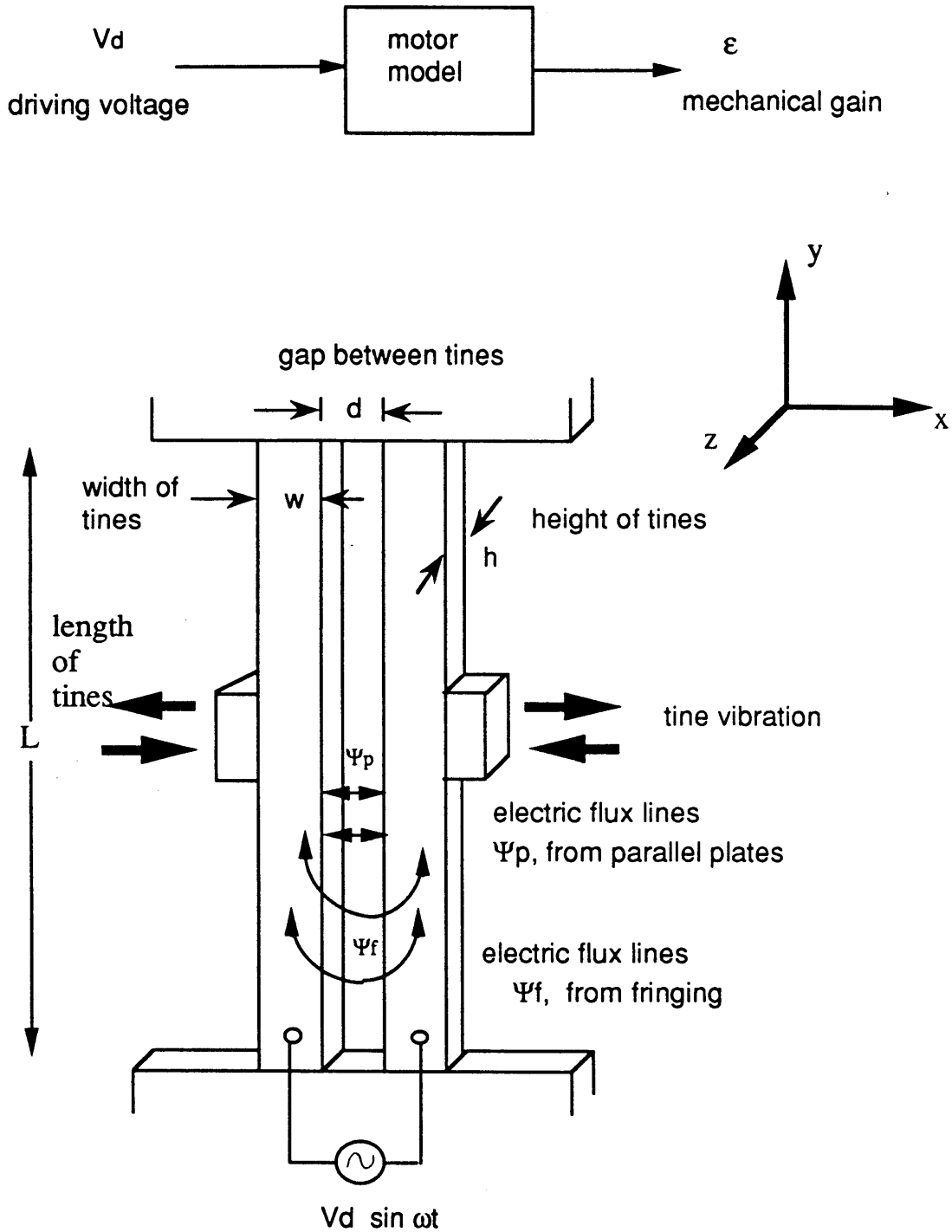
Figure 4.2   Diagram of Tuning Fork Motor

The electric flux lines are assumed to be two-dimensional as drawn in Figure 4.3. It is also assumed that the gap distance, d, is constant. This approximation is valid only if the tine vibration amplitude is small compared to the gap distance. It is desireable to make a transformation from the z-plane to the w-plane which would produce a one-dimensional flux bounded by known potentials. An appropriate transformation would be to transform the upper half of the z-plane into a closed rectangle with the sides at the potentials V_1, $-V_0$, 0, and V_0, as drawn in Figure 4.3. The value of the potential field in the same plane as the top of the tines, and outside of the tine gap, is assumed to be constant and denoted by V_1. The symbol V_0 is used to denote one-half of the driving differential voltage, so that,

$$V_0 = \frac{1}{2} V_d .$$

A transformation that maps a line segment on the real axis in the z-plane to a closed polygon in the w-plane is known as the *Schwarz-Christoffel transformation* [16]. The transformation is of the form,

$$\frac{dw}{dz} = C_1 (z - u_1)^{\beta_1} (z - u_2)^{\beta_2} \cdots (z - u_n)^{\beta_n} \tag{4.1-2}$$

This folds up the real line in the z-plane at the points $z_r = u_r$ by an angle given by α_r, where,

$$\alpha_r = \pi (1 + \beta_r).$$

The constant, C_1, is known as the *expansion constant* and is determined by the particular boundary conditions of the transformation.

To form a rectangle with the four corners given by the points $\mathcal{A}$, $\mathcal{B}$, $\mathcal{C}$, and $\mathcal{D}$ from Figure 4.3, the transformation parameters are,

$$\alpha_1 = \alpha_2 = \alpha_3 = \alpha_4 = \frac{\pi}{2}, \quad \text{and}$$

$$u_1 = -(\frac{d}{2} + w) , \quad u_2 = -\frac{d}{2} , \quad u_3 = \frac{d}{2} , \quad u_4 = \frac{d}{2} + w. \tag{4.1-3}$$

Combining equations (4.1-3) and (4.1-2) gives,

Z Plane
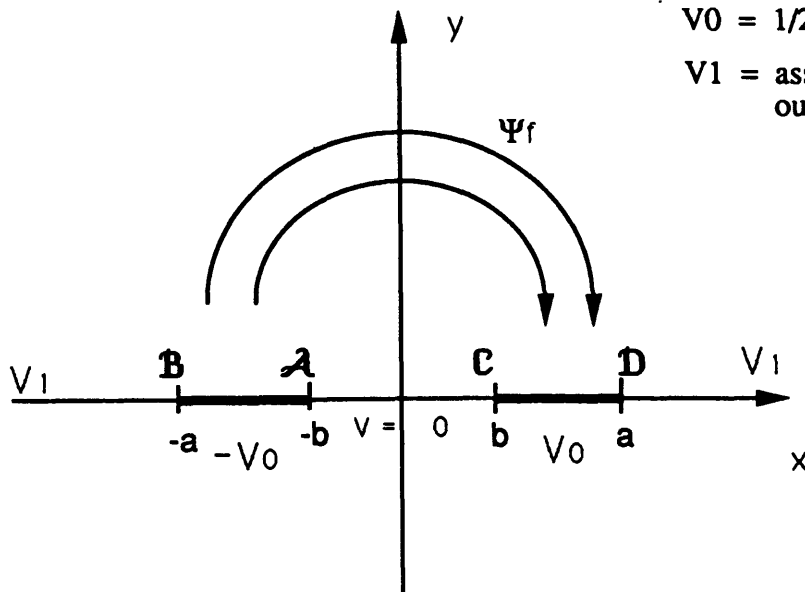
VO = 1/2 of driving voltage

V1 = assumed constant voltage outside of tine gap

W Plane
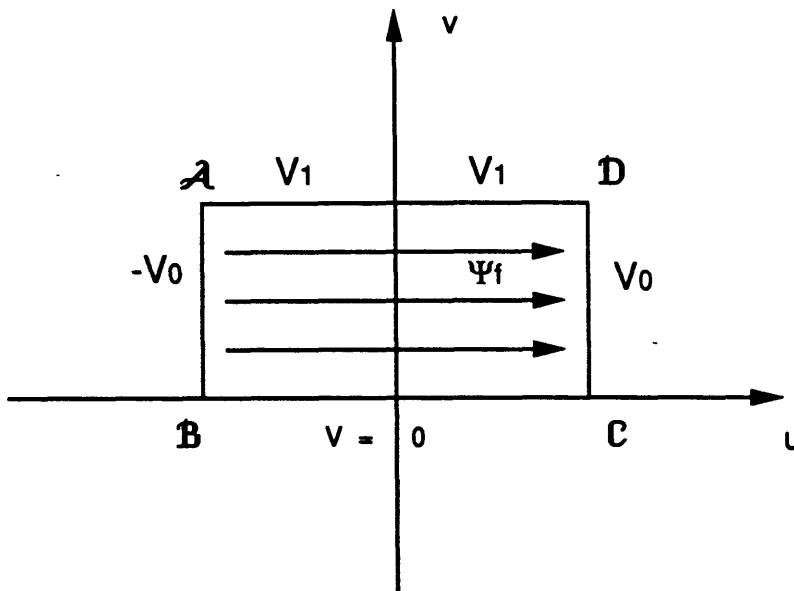
Figure 4.3 Conformal Mapping for Electrostatic Fringing Flux

71

$$w(z) = C_1 \int \left(z + \frac{d}{2} + w\right)^{-\frac{1}{2}} \left(z + \frac{d}{2}\right)^{-\frac{1}{2}} \left(z - \frac{d}{2}\right)^{-\frac{1}{2}} \left(z - \frac{d}{2} - w\right)^{-\frac{1}{2}} dz \tag{4.1-4}$$

Let $a = \frac{d}{2} + w$, and $b = \frac{d}{2}$, then Eqn. (4.1-4) is written,

$$w(z) = C_1 \int \frac{dz}{\sqrt{z^2 - a^2}\ \sqrt{z^2 - b^2}} . \tag{4.1-5}$$

By making the change of variables $\zeta = \frac{z}{a}$, and defining $k = \frac{b}{a}$, the integral in Eqn.

(4.1-5) can be written in Jacobi's form of the *elliptic integral of the first kind* [14],

$$w(\zeta) = C_2 \int \frac{d\zeta}{\sqrt{1 - \zeta^2}\ \sqrt{1 - k^2\zeta^2}} . \tag{4.1-6}$$

The constant, k, is known as the *elliptic integral modulus*, and the constant C_2 is

defined as,

$$C_2 = -\frac{1}{b} C_1.$$

The constant of integration from the indefinite integral of Eqn. (4.1-6) can be

made zero if the transformation is defined such that the origin in the z-plane maps to the

origin in the w-plane. As the variable z progresses from the origin to pt. C from figure

4.3, the variable ζ goes from $\zeta = 0$ to $\zeta = 1$. The transformation at C is then,

$$w(\zeta)\big|_{\text{pt. C}} = C_2 \int_0^1 \frac{d\zeta}{\sqrt{1 - \zeta^2}\ \sqrt{1 - k^2\zeta^2}} = C_2 K(k). \tag{4.1-7}$$

$K(k)$ is defined as the *complete* elliptic integral of the first kind. An elliptic integral is

complete when the integration is taken from zero to unity and the integral is written in

Jacobi's form. Efficient computational algorithms are available [14] to evaluate

complete elliptic integrals. In order to describe the transformation integral at the

complex points D and A, a conjugate to the complete elliptic integral is defined [16],

$$K'(k) = \int_{1}^{\frac{1}{k}} \frac{dt}{j \sqrt{1-t^2} \sqrt{1-k^2 t^2}}$$

(4.1-8)

where t is a complex number. It is shown by Gibbs [15] that the integral conjugate can be written,

$$K'(k) = K(k') \quad \text{where} \quad k' = \sqrt{1-k^2}$$

and k' is called the *modulus conjugate*. For the line segment $C\mathcal{D}$ in the z-plane the variable z goes from 1 to $\frac{1}{k}$, and the integration variable in the w-plane proceeds in the direction of the imaginary axis. The transformation at $\mathcal{D}$ is then recognized as,

$$w\big|_{Pt.\,\mathcal{D}} = C_2 K(k) + j C_2 K'(k)$$

$$= C_2 [K(k) + j K(k')].$$

By using negative values of z as it progresses from the origin in Figure 4.3 to points $\mathcal{A}$ and $\mathcal{B}$, it is readily shown that,

$$w\big|_{Pt.\,\mathcal{A}} = -C_2 K(k) \quad \text{and}$$

$$w\big|_{Pt.\,\mathcal{B}} = -C_2 [K(k) + j K(k')].$$

(4.1-9)

The solution to the complete elliptic integral of Eqn. (4.1-7) can be written in terms of *Jacobi Elliptic Functions* [15,16],

$$w(z) = \frac{1}{C_2} sn^{-1} \left(\frac{z}{b}, \frac{b}{a} \right) .$$

(4.1-10)

Using the boundary conditions for the voltages from Figure (4.3) at point $\mathcal{D}$,

$$K(k) + j K(k') = C_2 (V_0 + V_1) \quad \text{which implies}$$

$$C_2 = \frac{K(k)}{V_0} \quad \text{and} \quad V_1 = \frac{K(k') V_0}{K(k)} .$$

(4.1-11)

Eqn. (4.1-10) is now written,

$$w(z) = \frac{V_0}{K(k)} sn^{-1} \left(\frac{z}{b}, \frac{b}{a} \right).$$

(4.1-12)

The transformation can be checked by choosing points and using the appropriate tables to evaluate the elliptic integrals and elliptic functions.

73

The electrostatic problem in the w-plane is one-dimensional and can be solved routinely. Let C_w denote the capacitance between the parallel plates represented by the segments AB and CD, then

$$C_w = \frac{\varepsilon_0 \, CD_w \, L}{d_w} \qquad \text{where,} \qquad (4.1\text{-}13)$$

CD_w = the length of the segment CD in the w-plane

d_w = the distance between the parallel plates in the w-plane

L = The length of the tines

From the mappings given in Eqn. (4.1-9) this can be written in terms of z-plane dimensions,

$$C = C_w = \frac{\varepsilon_0 \, L \, K(k')}{2 \, K(k)}. \qquad (4.1\text{-}14)$$

Let U denote the electric energy between the parallel plates and F_2 denote the electrostatic force between them,

$$U = \frac{1}{2} C V_d^2$$

$$F_2 = \frac{1}{2} V_d^2 \frac{\partial C}{\partial d} \qquad (4.1\text{-}15)$$

where d is the gap between the tines as shown in Figure 4.2. Note that the electric energy is written in terms of the differential voltage between the plates, denoted by V_d. Differentiating the capacitance from Eqn. (4.1-15),

$$\frac{\partial C}{\partial d} = \frac{L}{2} \varepsilon_0 \left[\frac{K(k) \frac{\partial}{\partial d} K(k') - K(k') \frac{\partial}{\partial d} K(k)}{K^2(k)} \right] \qquad (4.1\text{-}16)$$

Let the integrands for the complete elliptic integral (4.1-7) and its conjugate be denoted by the functions $g(\zeta,d)$ and $f(\zeta,d)$,

$$K(k) = \int_0^1 g(\zeta,d) \, d\zeta, \qquad K(k') = \int_0^1 f(\zeta,d) \, d\zeta \ . \qquad (4.1\text{-}17)$$

The values of the modulus and its conjugate are written in terms of the gap distance and tine width,

$$k \ = \ \frac{b}{a} \ = \ \frac{d}{d + 2w} \qquad \text{and}$$

$$k' \ = \ \sqrt{1 \ - \ \frac{d^2}{(d + 2w)^2}} \ . \qquad (4.1\text{-}18)$$

By Leibnitz's Rule [18] the partial derivitive with respect to the gap distance can be taken inside the integral so that

$$\frac{\partial C}{\partial d} \ = \ \frac{L}{2} \varepsilon_0 \left[\frac{\displaystyle\int_0^1 g\,(\zeta,d)\,d\zeta \int_0^1 \frac{\partial}{\partial d} f\,(\zeta,d)\,d\zeta \ - \ \int_0^1 f\,(\zeta,d)\,d\zeta \int_0^1 \frac{\partial}{\partial d} g\,(\zeta,d)\,d\zeta}{\left[\displaystyle\int_0^1 g\,(\zeta,d)\,d\zeta\right]^2} \right] \qquad (4.1\text{-}19)$$

Substituting from (4.1-7) and (4.1-18) and differentiating,

$$\frac{\partial\, f(\zeta,d)}{\partial d} \ = \ A_1\,(d,w) \ \frac{-\zeta^2}{\left(1 - \zeta^2\right)^{\frac{1}{2}} \left(1 - k'^2\zeta^2\right)^{\frac{3}{2}}}$$

$$\frac{\partial\, g(\zeta,d)}{\partial d} \ = \ A_2\,(d,w) \ \frac{-\zeta^2}{\left(1 - \zeta^2\right)^{\frac{1}{2}} \left(1 - k'^2\zeta^2\right)^{\frac{3}{2}}} \qquad \text{where,}$$

$$A_1\,(d,w) \ = \ \frac{2\,w}{(\,d + 2w\,)^2} \qquad \text{and}$$

$$A_2\,(d,w) \ = \ \frac{2\,w\,d}{(\,d + 2w\,)^3} \qquad (4.1\text{-}20)$$

Substituting into Eqn. (4.1-19),

75

$$\frac{\partial C}{\partial d} = \frac{\varepsilon_0 \, L \, K \, (k) \, A_1 \, (d,w)}{2 \, K^2 \, (k)} \int_0^1 \frac{-\zeta^2 \, d\zeta}{\left(1 - \zeta^2\right)^{\frac{1}{2}} \left(1 - k'^2\zeta^2\right)^{\frac{3}{2}}} -$$

$$\frac{\varepsilon_0 \, L \, K \, (k') \, A_2 \, (d,w)}{2 \, K^2 \, (k)} \int_0^1 \frac{-\zeta^2 \, d\zeta}{\left(1 - \zeta^2\right)^{\frac{1}{2}} \left(1 - k'^2\zeta^2\right)^{\frac{3}{2}}} \qquad (4.1\text{-}21)$$

The integrals in Eqn. (4.1-21) can be shown to be the derivative of the complete elliptic integral of the first kind,

$$\frac{d \, K}{d \, k} = \int_0^1 \frac{-\zeta^2 \, d\zeta}{\left(1 - \zeta^2\right)^{\frac{1}{2}} \left(1 - k'^2\zeta^2\right)^{\frac{3}{2}}} \qquad (4.1\text{-}22)$$

One of the most significant results in the study of elliptic integrals came from the famous French mathematician Adrien-Marie Legendre in a paper of 1826, and it may be stated as a theorem [14],

Theorem 4.1:

If P(x) is a polynomial of at most fourth degree with real coefficients and if R is a rational function of two variables with real coefficients, while x is restricted to a range in which P(x) is positive, the integral

$$\int_0^x R\left[x, \sqrt{P(x)}\right] \, dx$$

can be expressed as a linear combination of terms, each of which is either an elementary function, or an elliptic integral of the first, second, or third kind.

Theorem 4.1 implies that the derivative, $\frac{dK}{dk}$, can be written in terms of elliptic

integrals. The relationship was derived by Bowman [17] and is given by,

$$\frac{d\,K\,(k)}{dk} = \frac{E\,(k)\,-\,k'^2\,K\,(k)}{k\,k'^2}.\qquad(4.1\text{-}23)$$

The term $E\,(k)$ represents the *complete elliptic integral of the second kind*, and it is

also readily evaluated by computational algorithms.

Substituting Eqns. (4.1-23) and (4.1-21) into (4.1-15) for the electrostatic force

from the fringing,

$$F_2 = \frac{\varepsilon_0\,V_d^2\,L}{4\,k\,k'}\left[\frac{E\,(k')\,A_1}{k\,K\,(k)} - \frac{k\,K\,(k')\,A_1}{K\,(k)} + \frac{E\,(k)\,K\,(k')\,A_2}{k'\,K^2\,(k)} - \frac{k'\,K\,(k')\,A_2}{K\,(k)}\right]\qquad(4.1\text{-}24)$$

The total electrostatic force that the tines are subjected to is obtained by adding the

forces from the parallel flux (4.1-1) and the fringing flux,

$$F_0 = F_1 + 2\,F_2.\qquad(4.1\text{-}25)$$

To include fringing from both the top and bottom of the tines a factor of two is

included. The computational techniques for evaluating Eqn. (4.1-24) will not be

described in this paper. The reader is referred to Battin [14] and Press *et al* [19] for a

description of the algorithms used. For a set of typical dimensions for the tines,

$$L\;=\;500\text{ microns}\qquad d\;=\;5\text{ microns}$$

$$h\;=\;15\text{ microns}\qquad w\;=\;4\text{ microns}$$

The force component due to the fringing is calculated to be 20 % of the total force.

The fringing has the advantage of adding a significant amount of force per volt, but has

the disadvantage of being highly nonlinear.

The electrostatic force represented by the equations above produces a uniform

load on each tine. The tines are modeled as Bernoulli-Euler beams fixed at both ends,

as shown in Figure 4.4. The static deflection curve is given by [20],
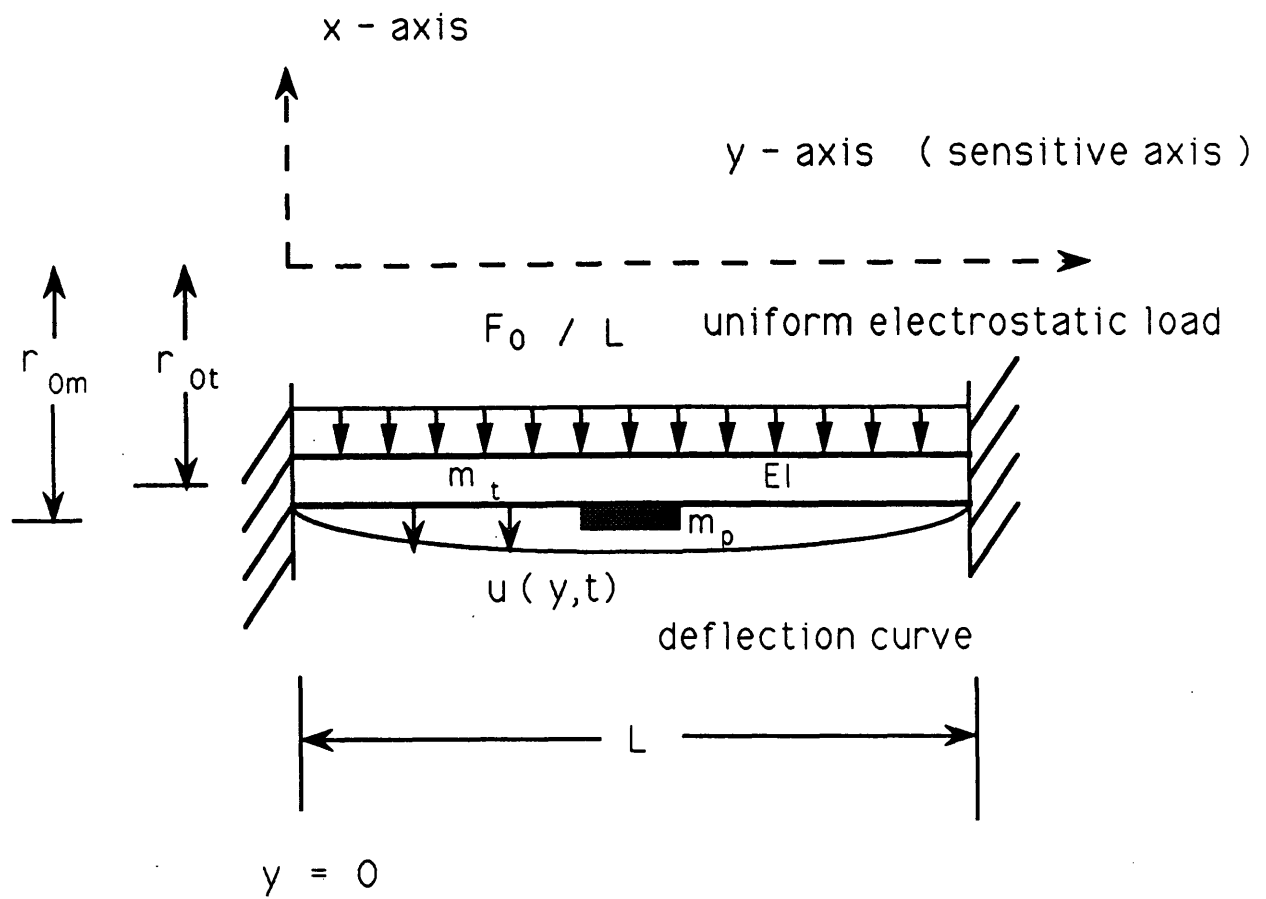
Figure 4.4 Tine deflection from electrostatic force

$$u(y) = \frac{F_0 y^2}{24\,E\,I\,L}(L-y)^2 \tag{4.1-26}$$

where I denotes the beam inertia of the tine,

$$I = \frac{1}{12}\,h\,w^3$$

Since the tines are assumed to be driven at a frequency significantly below their resonance, as described in Chapter 2, the deflection curve is sinusoidal at the driving frequency, ω_d

$$u(y,t) = u(y)\sin\omega t.$$

If the proof mass is approximated by a point mass with the magnitude denoted by, m_p , and the inertia of the proof mass about the y-axis (sensitive axis) is denoted by I_m ,

$$I_m = m_p\left[r_{0m} + u\left(\frac{L}{2},t\right)\right]^2 \quad\text{where,}$$

r_{0m} = nominal distance from the proof mass to sensitive axis

Assuming that the tine vibration amplitude is small such that second order terms in u(y,t) can be neglected, the proof mass inertia becomes,

$$I_m \approx m_p r_{0m}^2 + 2\,m_p r_{0m} u\left(\frac{L}{2},t\right) = I_{0m} + I_{1m}\sin\omega t$$

where, from Eqn. (4.1-26), the oscillating component is given by,

$$I_{1m} = \frac{F_0 L^3 m_p r_{0m}}{192\,E\,I}. \tag{4.1-27}$$

For each tine of mass m_t the moment of inertia about the y-axis is defined as I_t, where,

$$I_t = \int_0^L \left[r_{0t} + u(y,t)\right]^2 dy \tag{4.1-28}$$

Again assuming that second order terms in u(y) are negligable and that the height and width of the tines are small compared to the length, Eqn. (4.1-28) becomes

$$I_t = m_t r_{0t}^2 + 2\,\rho\,h\,w\,r_{0t}\int_0^L u(y)\,dy\,\sin\omega t \quad\text{where,}$$

$$r_{0t} = \text{nominal distance from tine center of mass to the y-axis}$$

$$\rho = \text{density of tine material (silicon)}$$

Integrating the deflection curve of (4.1-26) and writing the tine inertia about the y-axis as a nominal term plus an oscillating term,

$$I_t = I_{0t} + I_{1t} \sin wt \qquad \text{where}$$

$$I_{0t} = m_t r_{0t}^2 \qquad \text{and}$$

$$I_{1t} = \frac{m_t r_{0t} F_0 L^3}{360 \, E I} . \tag{4.1-29}$$

Combining Eqns. (4.1-27) and (4.1-29) the mechanical gain of the device is a linear function of the electrostatic force,

$$\varepsilon = \frac{\dfrac{F_0 L^3}{E I} \left[\dfrac{m_p r_{0m}}{192} + \dfrac{m_t r_{0t}}{360} \right]}{m_p r_{0m}^2 + m_t r_{0t}^2} \tag{4.1-30}$$

8 0

4.2 Sensor Model

The function of the sensor is to transform the magnitude of the output angle vibration into an electrical signal. The sensor is comprised of four capacitance plates on each side of both wings. Four electrodes are situated above the plates, and an excitation voltage is applied across the four sets of capacitor plates. As the wings vibrate due to the gyroscopic torque the capacitance between the plates is altered. The electrical signals coming from the capacitors are combined and processed to provide the gyroscope output signal.

This is the same type of sensor used on the double gimbal micromechanical gyroscope designed by Boxenhorn [1,2]. The sensor on the Boxenhorn gyroscope has been shown to be sufficiently linear. For simplicity purposes, the signal processing electronic configuration is designed to be identical to the open loop configuration of the Boxenhorn gyroscope. In this section, only the fundamentals of the sensor model are presented. The reader is referred to Boxenhorn for a more detailed derivation.

Figure 4.5 shows the sensor geometry on one wing. The parameters x_1 and x_2 denote the distances from the sensitive axis to the front and back edges of the sensor plates, respectively. The distance, g, is the nominal gap between the capacitor plates, and W_y denotes the width of the plates (y-dir). On one side of the wing the capacitance is increased by the angular rotation, θ, and is given by [1,15]

$$C_i = \int_{x_1}^{x_2} \frac{\varepsilon_0 W_y \, dx}{g - \theta x} = \frac{\varepsilon_0 W_y}{\theta} \ln \left(\frac{g - \theta x_1}{g - \theta x_2} \right)$$

$$(4.2\text{-}1)$$

And, on the other side the capacitance is decreased,

$$C_d = \int_{x_1}^{x_2} \frac{\varepsilon_0 W_y \, dx}{g + \theta x} = - \frac{\varepsilon_0 W_y}{\theta} \ln \left(\frac{g + \theta x_1}{g + \theta x_2} \right)$$

$$(4.2\text{-}2)$$

Expanding Eqns. (4.2-1) and (4.2-2) in a Taylor series about the point $\theta = 0$,

$$C_i = C_0 + \frac{\varepsilon_0 W_y \left(x_2^2 - x_1^2\right)}{2 g^2} \theta + \frac{\varepsilon_0 W_y \left(x_2^3 - x_1^3\right)}{6 g^2} \theta^2 + O\left(\theta^3\right)$$

$$C_d = C_0 - \frac{\varepsilon_0 W_y \left(x_2^2 - x_1^2\right)}{2 g^2} \theta + \frac{\varepsilon_0 W_y \left(x_2^3 - x_1^3\right)}{6 g^2} \theta^2 + O\left(\theta^3\right)$$

where C_0 represents the nominal capacitance between the parallel plates,

$$C_0 = \frac{\varepsilon_0 W_y (x_2 - x_1)}{g} \qquad (4.2\text{-}3)$$

If the capacitances are subtracted,

$$\Delta C = C_i - C_d = K_s C_0 \theta + O(\theta^3)$$

where the sensor scale factor is given by

$$K_s = \frac{x_1 + x_2}{2 g} . \qquad (4.2\text{-}4)$$

Subtracting the two variable capacitance signals has two advantages. First, the error in the linear model of the sensor is reduced to $O(\theta^3)$ since the quadratic terms in the expansion cancel each other. Second, any error caused by a deflection of the wings in the z-direction will be eliminated. The deflection will cause a change in capacitance of equal magnitude on both sides of the sensor, and the errors will cancel each other.

A diagram of the signal processing electronics is shown in Figure 4.4. The ΔC signal from each wing is added, amplified, demodulated twice, and run through a low pass filter to produce the voltage output. The baseline design assumes that the electronic configuration is fixed. The relationship between the output signal and the change in capacitance is given by,

$$e_{out} = 100 \left(\frac{2}{\pi}\right)^2 \frac{\Delta C}{C_{fb}} E_x . \qquad (4.2\text{-}5)$$

suspended electrode plates
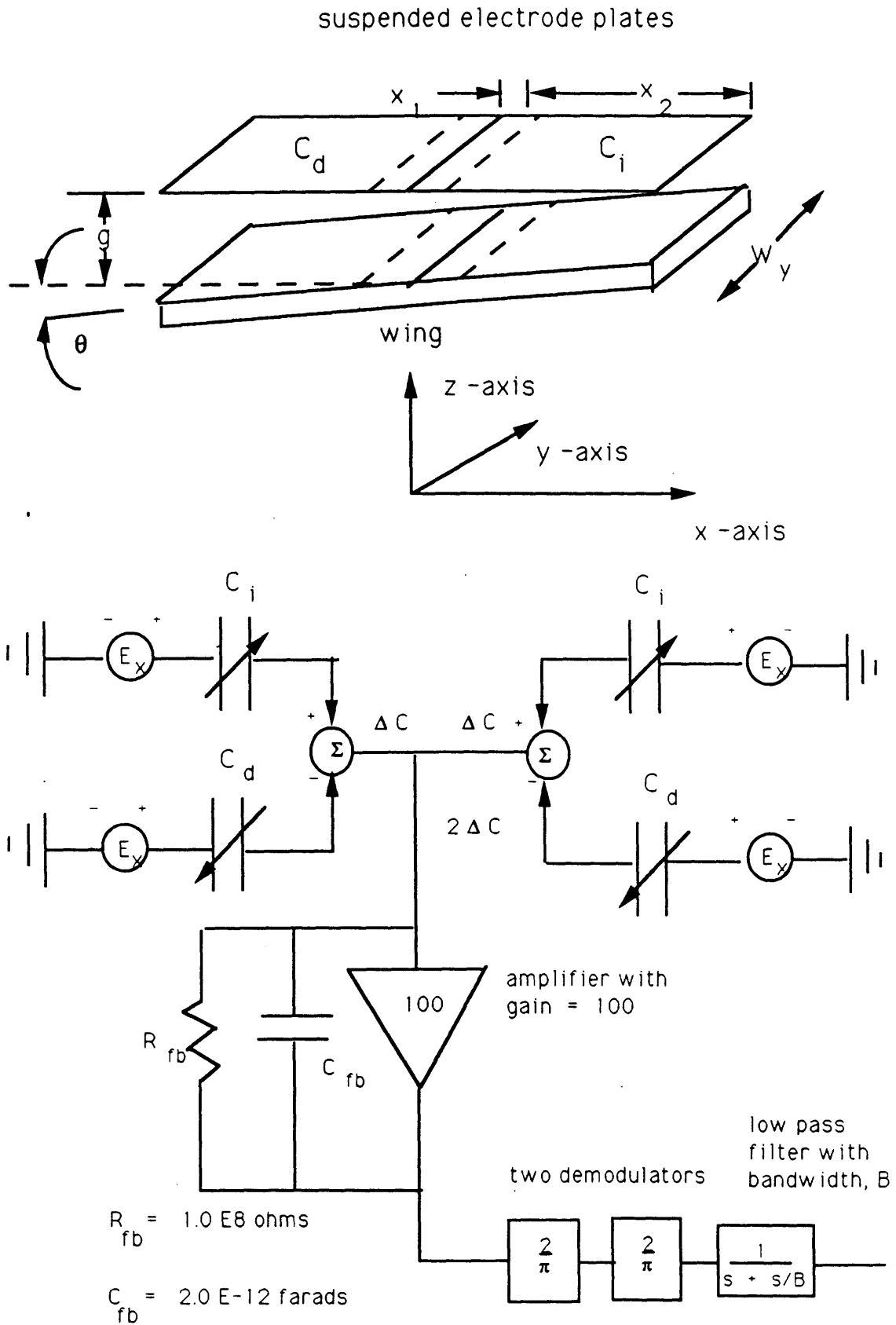
Figure 4.5 Sensor Diagram

83

4.3 Mechanical Factors

The gyroscope rotation is provided by two thin, rectangular silicon shafts which twist axially about their cross-sectional center of gravity and serve as torsional springs. The flexures extend on both ends from the wings and are fixed to the substrate. They are designed assuming a fixed length and width, and varying the thickness to yield a torsional stiffness that corresponds to the desired frequency.

It is important that the stiffness model for the flexures is accurate since the driving frequency is tuned to the torsional resonant frequency. The classical St. Venant solution which determines the stiffness of the flexures [21] is not applicable in this case for two reasons. First, the St. Venant solution assumes free ends, that is, it allows the rectangular ends to warp. But, in this case, both ends are fixed and constrained from warping. Second, since the flexures are of a different thickness than the wings, they must be fabricated using separate etching diffusions. When boron is diffused into the silicon, which is needed for the selective etching process, the boron atoms replace the larger silicon atoms and cause a lattice contraction. It is the relative contraction between the wing and the flexure that produces an axial pre-stress on the flexure which affects its torsional stiffness. The fabrication process will not be discussed in this paper. The reader is referred to the literature [22,23] for descriptions of micromechanical fabrication processes.

The flexure stiffness problem was solved by J. A. Connally in his MIT Master's thesis [24] <u>Torsion of a Thin Rectangular Beam with Axial Prestress and Ends Constrained from Warping</u>. The stiffness equation developed by Connally is used in the design presented here. The torsional stiffness for the flexure shown in Figure 4.5 is given by,

$$k_t = \frac{\frac{1}{3} f_z f_x^3 G \mu}{l_f - L_c} \quad \text{where,}$$

$$\mu = 1 + \frac{1}{4}\left(\frac{f_z}{f_x}\right)^2 \frac{\sigma_0}{G}$$

$$L_c = \frac{f_z \sqrt{E}}{\left[12\left(\sigma_0 + G\right)\mu\right]^{\frac{1}{2}}}$$

(4.1-1)

where,

σ_0 = the axial prestress on the flexure

L_c = length correction factor

f_z = thickness of flexures

f_x = width of flexures

Connally's equations were verified by a finite element model, and the error was shown to be within 4 %. Also, the model was used to calculate the natural frequencies for a double gimbal micromechanical test device designed by Boxenhorn. For six different frequency tests, the Connally model yielded accuracies within 10%.

The magnitude of the prestress is determined from the relative diffusion contraction between the flexures and the wings. The misfit factor between boron and silicon atoms is defined as [25],

$$\beta = \frac{1 - \left(\frac{r_b}{r_{si}}\right)^3}{\mu_{si}} \quad \text{where}$$

(4.3-2)

r_b = atomic radius of boron = 0.98 angstoms

r_{si} = atomic radius of silicon = 1.17 angstroms

μ_{si} = Poisson's ratio for silicon = 0.33

The axial contraction of each flexure (y-dim) is proportional to the misfit factor, the concentration ratio, and the axial length of the flexure [25]

85

$$\delta_f = \beta \left(\frac{c_{bf}}{c_{sif}} \right) l_f$$

and for the contraction of each wing,

$$\delta_w = \beta \left(\frac{c_{bw}}{c_{siw}} \right) w_y \qquad (4.3\text{-}3)$$

where,

c_{bf} = concentration of boron atoms for each flexure

c_{sif} = concentration of silicon atoms for each flexure

c_{bw} = concentration of boron atoms for each wing

c_{sif} = concentration of silicon atoms for each wing

Generally, for fabricating micromechanical structures with thicknesses less than 10 microns deep, the boron concentration is two orders of magnitude less than the silicon concentration. The resulting axial stress in each flexure is given by,

$$\sigma_0 = \frac{(\delta_w - \delta_f) E}{l_f} \qquad (4.3\text{-}4)$$

One complicating factor in calculating the torsional stiffness of the flexures is that single crystal silicon is *anisotropic*. This means that the elasticity of a single crystal silicon structure depends on the orientation of the lattice surfaces. The values for the silicon elasticity constants used in the calculations are

$$E = 1.7\ E11\ N/m^2 \quad \text{and} \quad G = 5.1\ E10\ N/m^2 .$$

These values were documented by Connally [24] by assuming that the etching process will cut symmetric structures along the (1,1,0) crystal planes.

Equations for the shear stresses induced in the flexures by the axial twisting were also determined by Connally. They are shown [24] to be at very low levels for micromechanical structures, and hence are not of much concern. However, if the width of each wing (y-dim) is designed to be significantly longer than the length of each flexure, the axial stress (4.3-4) becomes very large. This tensile stress stiffens up the flexures and reduces the reliability of the device if it approaches the yield strength.
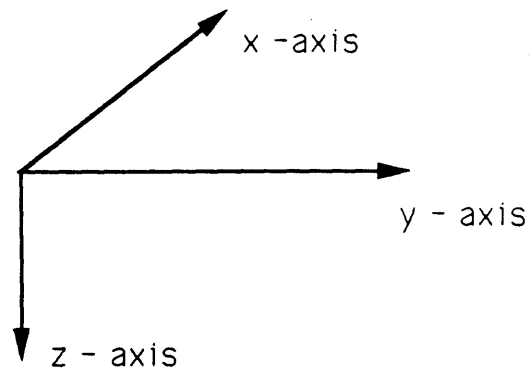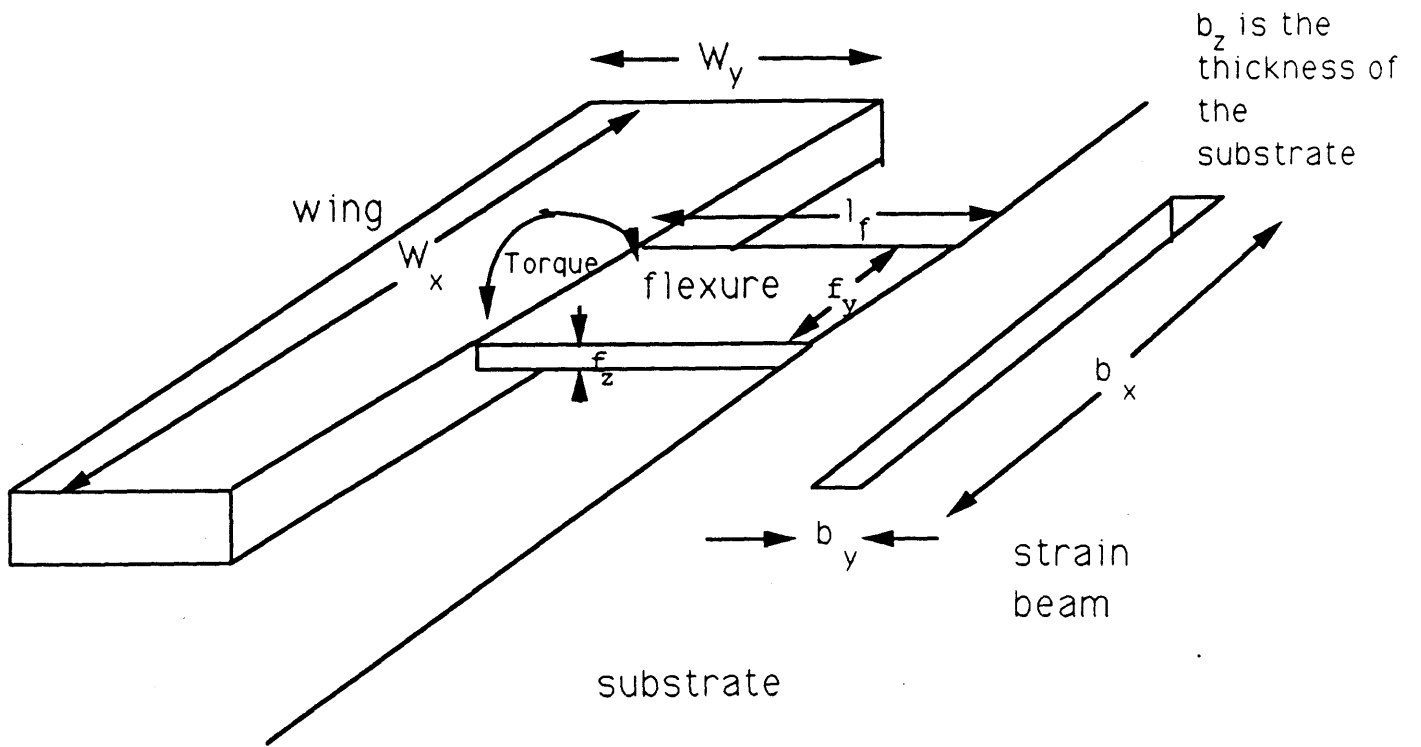
figure 4.6 Torsional Flexure

To reduce the axial stress, the device is designed with a strain relief beam in the substrate near the flexure end. The strain relief beam is a slot which is cut through the substrate and absorbs some of the strain induced by the lattice contraction. It is shown in Figure 4.6. The flexure and the strain beam act as linear springs in series acted upon by the tensile deflection. The effective linear stiffnes is given by

$$k_{eff} = \frac{k_{lf} k_{lb}}{k_{lf} + k_{lb}} \qquad \text{where}$$

$$k_{lf} = \frac{Ebc}{l_f} \qquad \text{(flexure linear stiffness)}$$

$$k_{lb} = \frac{192 \, EI_b}{b_x} \qquad \text{(strain beam linear stiffness)}$$

$$I_b = \frac{1}{12} b_z b_y^3 \, . \qquad (4.3\text{-}5)$$

By appropriately designing the dimensions of the strain beam so that the beam stiffness is much less than the flexure stiffness, the majority of the contraction strain can be absorbed.

Stress levels in other areas of the device are not of much concern. For reasonable levels of external shock and vibration the possibility of structure failure is very low. Silicon is a very high strength material, and the device is homogeneous such that there are no obvious stress concentrations areas. The equations for the tine twisting, flexure bending, and wing bending, developed in Section 2.2, are also implemented in the system model to verify the rigid body assumption for a specific design.

4.4 Damping Model

In the system model introduced in Chapter 2, it was assumed that the torsional vibrations encounter a restraining damping torque that is proportional to the angular velocity. The source of the damping torque is almost wholly attributed to fluid damping.

Since the device is homogeneous with no joints or sliding surfaces, any structural damping is assumed to be negligable. The damping is an important design consideration since the sensitivity (2.4-5) and the stability criteria (3.2-19) are both written in terms of the system quality factor. In fact, the Boxenhorn micromechanical gyroscope [1] is designed to be operated in a vacuum package to limit the air damping and increase the sensitivity. For the tuning fork configuration the air damping is confined mainly to the sensor wings so that the damping is less significant than the double gimbal configuration.

The damping is written in terms of the quality factor, Q, which is related to the system frequency, inertia, and linear damping coefficient by Eqn. (2.4-5). The mathematical model of the damping is intended to provide an approximate upper bound on the damping torque, or a lower bound on Q. This is meant to simplify the fluid mechanics analysis yet still provide a conservative estimate of the gyroscope sensitivity.

The oscillating wing induces flow along its surface which produces a pressure difference between the two sides of the wing. The pressure difference leads to a damping torque that resists the oscillation. Two flow patterns that provide the majority of the damping torque are identified:

1) air flow impingement on the wing surface as it oscillates.

2) air pumping through the channel between the wing and its bridge electrode.

The damping due to each of these flow patterns is analyzed seperately, then it is multiplied by two to account for both wings to provide the system Q estimate.

Air Flow Impingement

The air flow on the oscillating wing is modeled as a plate suspended in a free stream of air with velocity

89

$$U_\infty = \frac{W_x}{2} \omega \qquad \text{where}$$

W_x = length (x-dim) of the entire wing

ω = angular velocity of wing in rad/sec $\qquad\qquad$ (4.4-1)

This free stream velocity corresponds to the maximum linear velocity on the oscillating wing. The model is simplified by assuming that the flow over the entire wing is in one direction. Actually, as the wing rotates about its pivot, each side of the wing is moving in a different direction. However, for the simple model presented here, the damping effect is equivalent. A diagram of the model is shown in Figure 4.7. The viscous air flow is assumed to be incompressible and steady with respect to the oscillating wing. Also, the flow is assumed to be two dimensional such that the air flows along the plate in the x-direction as drawn. Again, this is conservative since the neglected flow around the plate edge in the y-direction will decrease the pressure gradient. The two dimensional continuity equation in differential form is written

$$\frac{\partial u}{\partial x} + \frac{\partial w}{\partial z} = 0$$

$\qquad\qquad$ (4.4-2)

where,

u $\equiv$ air flow velocity component in x-direction

w $\equiv$ air flow velocity component in z-direction.

The Navier Stokes equations [26] in two dimensions describe the flow momentum

$$u\frac{\partial u}{\partial x} + w\frac{\partial u}{\partial z} = -\frac{1}{\rho}\frac{\partial P}{\partial x} + \frac{\mu}{\rho}\left(\frac{\partial^2 u}{\partial x^2} + \frac{\partial^2 u}{\partial z^2}\right)$$

$$u\frac{\partial w}{\partial x} + w\frac{\partial w}{\partial z} = -\frac{1}{\rho}\frac{\partial P}{\partial z} + \frac{\mu}{\rho}\left(\frac{\partial^2 w}{\partial x^2} + \frac{\partial^2 w}{\partial z^2}\right)$$

$\qquad\qquad$ (4.4-3)

The density of the air, ρ , is assumed constant , and the viscosity is given by μ. For a no-slip condition along the surface of the wing the boundary conditions are

$$w = 0 \quad \text{at} \quad z = 0 \ , \quad -L < x < L$$

$$u = 0 \quad \text{at} \quad z = 0 \ , \quad -L < x < L$$

$$w = -U_\infty \ , \text{ and } \quad u = 0 \quad \text{at free stream.}$$

This problem was solved by Happel [27] and the solution for the resultant force on the plate is given by,

$$F_f = -16\,\mu\,L\,U_\infty = -16\,\mu\,L^2\,\omega \quad \text{for } L = \frac{W_x}{2} \ . \tag{4.4-4}$$

Translating this to a pressure drop and substituting the dimensions of the wing

$$\Delta P_f = 4\,\mu\,\omega\,\frac{W_x}{W_y} \ . \tag{4.4-5}$$

Channel Pumping

As seen from Eqn. (4.2-4) the gyroscope output signal is inversely proportional to the gap distance between the wing and the electrode plate suspended over the wing. For a small gap, as the wing oscillates air is *pumped* between the electrode plate and the wing. The viscosity of the air flow adds to the pressure differential between each side of the wing.

Again, the flow is assumed to be two dimensional, as shown in the bottom half of Figure 4.7. For the pumping effect only one-half of the wing is analyzed. This is because the bottom of the substrate beneath the wing is at a great enough distance such that no pumping occurs. It is furthur assumed that along the oscillating axis (x = 0) the air is unperturbed.

Define Q_f as the volumetric flow rate through the channel

$$Q_f = -\frac{d}{dt}\,(\,g\,L\,W_y\,) \ . \tag{4.4-6}$$

The dimension W_y is the width of the wing. For small values of the oscillation magnitude, θ , at an instant in time the channel gap is a function of x,

$$g\,(x) = g_0 - \theta\,x \ . \tag{4.4-7}$$

Equation (4.4-6) is then

$$Q_f(x) = L W_y x \omega .$$ (4.4–8)

Making the approximations $\frac{du}{dx} = 0$ and $w = 0$ the Navier Stokes equations

(4.4-3) reduce to

$$\frac{d^2 u}{dz^2} = \frac{1}{\mu} \frac{dP}{dx} .$$ (4.4-9)

Solving gives

$$u = \frac{1}{2\mu} \frac{dP}{dx} z^2 + C_1 z + C_2 .$$ (4.4-10)

For a no-slip condition at $z = \frac{g_0}{2}$ and $z = -\frac{g_0}{2}$, the constants are evaluated to give,

$$u(x, z) = \frac{1}{2\mu} \frac{dP}{dx} \left(z^2 - \frac{g_0^2}{4} \right)$$ (4.4-11)

Define Q'_f as the profile flow rate where

$$Q'_f = \int_{-\frac{g_0}{2}}^{\frac{g_0}{2}} u(x, z) \, dz = -\frac{dP}{dx} \frac{g_0^3}{12 \mu} .$$ (4.4-12)

Then the volumetric flow through the channel is

$$Q_f = W_y Q'_f = -W_y \frac{dP}{dx} \frac{g_0^3}{12 \mu} .$$ (4.4-12)

Equating Eqn. (4.4-12) and Eqn. (4.4-8) gives an expression for the pressure gradient along the plate,

$$\frac{dP}{dx} = \frac{-12 \mu L \omega x}{g_0^3}$$ (4.4-13)

Eqn. (4.4-13) is integrated and boundary condition $P = P_{atm}$ at $x = L$ is used to evaluate the constant of integration

$$P(x) = \frac{6 \mu L \omega}{g_0^3} \left(L^2 - x^2 \right) + P_{atm}$$ (4.4-14)

Flow impingement of one wing
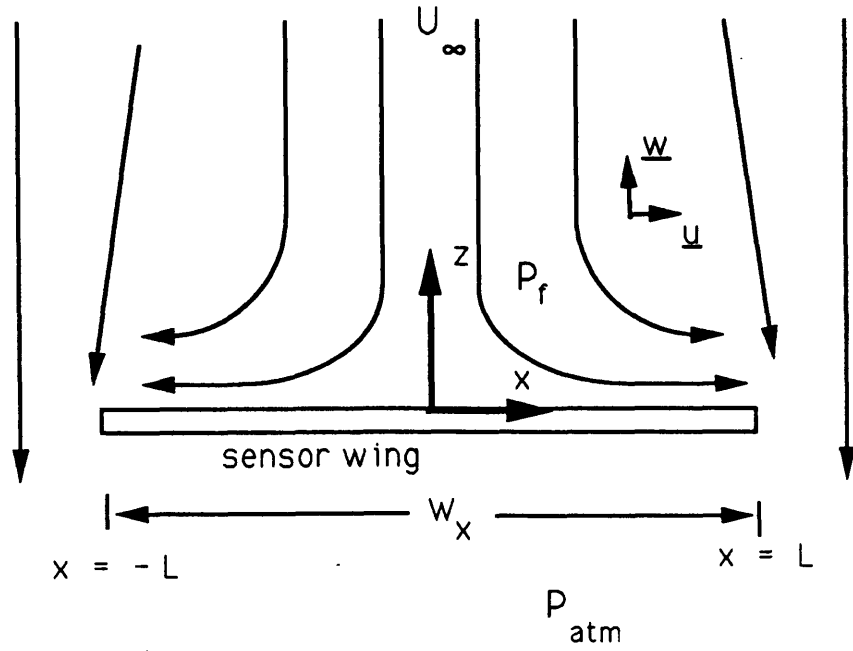
Channel Pumping
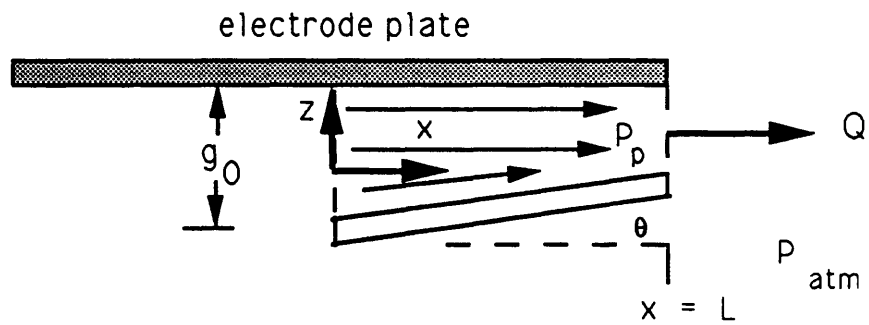
Figure 4.7   Damping Model

Integrating the change in pressure on both sides of the wing to obtain the resultant force gives

$$F_p = \int_A (P(x) - P_{atm}) \, dA = W_y \int_0^L (P(x) - P_{atm}) \, dx \tag{4.4-15}$$

Substituting the dimensions of the wing $L = \frac{W_x}{2}$ yields the result

$$F_p = \frac{W_y \, W_x^4 \, \omega \, \mu}{4 \, g_0^3} \, . \tag{4.4-16}$$

The moment arm for the resultant force on the wing is

$$d = \frac{W_x}{4}$$

Thus, the net restraining torque from both flow patterns is given by,

$$T_{damp} = \frac{2 \, W_x}{4} \, (F_f + F_p) \tag{4.4-17}$$

where the forces are given in Equations (4.4-4) and (4.4-16) and the factor of two accounts for two wings. The net restraining torque relates to the linear damping coefficient by

$$T_{damp} = b_t \frac{d\theta}{dt} \, .$$

This can be written in terms of the system quality factor to give

$$Q = \frac{2 \, \omega^2 \, I_0}{W_x \, (F_f + F_p)} \, . \tag{4.4-18}$$

It is seen from the force equations that if the gap distance is significantly smaller than the wing dimensions, the pumping effect will contribute the majority of the damping. This indicates that if the conservative model from Eqn. (4.4-18) gives a value of Q which is too small, design alternatives to reduce the pumping should be investigated. Strategically oriented slits in the wing will reduce the damping from the channel pumping. However, the baseline design presented in this paper will be restricted to a solid wing design, and if the damping is excessive, a vacuum package will be implemented.

94

4.5 Error Sources

It is now appropriated to discuss the various error sources that are inherent in the micromechanical tuning fork gyroscope, and to determine design criteria to minimize the errors. The error sources are classified into four categories: modeling errors, external torques, internal torques, and random noises. This excludes errors due to cross coupling and time-variant terms in the equation of motion which were investigated in Chapters 2 and 3.

Modeling Errors

The calibration of the gyroscope linear response to an applied rate depends on fixed values for system frequency, quality factor, and mechanical gain. However, during a mission the gyroscope is subjected to changes in temperature and pressure. If the stiffness properties of the torsional flexures are altered, the driving frequency will differ from the torsional resonant frequency. This will decrease the sensitivity. Changes in pressure will affect the air damping properties so that the quality factor is not a constant. Furthermore, the mechanical gain depends on the tine stiffness properties which are affected by temperature and fatigue.

It is necessary that the system is designed to be *robust* to these deviations. The solution to modeling errors is best approached on a *system level* rather than an instrument level. Two possible methods to minimize these errors are packaging techniques and feedback control. First, it is desirable to isolate the instrument from the environment by its packaging. This would keep the gyro at a reasonably constant temperature and pressure. But, the design tradeoff is when the cost of the packaging, relative to the cost of the gyro, becomes excessive. It is then more efficient to lock the driving frequency on the torsional resonance through a feedback configuration, and control the motor by feeding back the tine

vibration amplitude. Feedback system and packaging design analysis is not presented in this paper, but represents a vital design study for a micromechanical tuning fork gyroscope.

External Torques

One of the advantages of a micromechanical gyroscope is its *ruggedness*. It is thus important that the device is insensitive to external vibrations and accelerations. Accelerations normal to the plane of the gyroscope, combined with a mass unbalance, yield a torque about the sensitive axis. This is a DC torque and will not affect the output signal. This requires that the mass unbalance is small enough that the maximum possible acceleration does not cause the wings to rotate to the point of striking the sensor plates. Micromechanical surfaces have a tendency to adhere to each other upon touching. Also, oscillating torques from external vibrations should not result in any errors since the system frequency is designed to be significantly higher than any reasonable external vibration frequency.

Internal Torques

It is also possible that the vibrating motor will lead to oscillating torques about the sensitive axis in the absence of an applied angular rate. The output signal of the gyroscope can be calibrated to account for these *zero rate errors* , but the gyroscope design should minimize these errors.

One source of an internal torque error is *motor-sensor coupling*. It is possible that the electric field which drives the tines can also effect the capacitance between the sensor wing and its bridge electrode. However, for the tuning fork configuration this effect is minimal. The motor is driven internally so that the parallel electric flux from the motor should not cross the sensor gap. The motor fringing flux coupling with the sensor can be minimized by situating the tines close to each other, and increasing the sensor wing area.

The internal motor represents a possible advantage of the tuning fork configuration over the double gimbal [1] micromechanical configuration. The advantage can not be quantified because it is difficult to accurately model the motor-sensor coupling. The magnitude of the coupling is most efficiently determined experimentally. For the purpose of the baseline design study, it is sufficient to say that the motor-sensor coupling can be made minimal.

Another source of internal torque is a misalignment in the z-direction of the two proof masses. As the tines oscillate, if the proof masses do not have their center of masses aligned with the sensitive axis, an oscilling torque will occur. Figure 4.8 shows the masses misaligned by a distance Δz. If x_m denotes the amplitude of vibration at the tine midpoint, the torque about the sensitive axis from the unbalance is given by

$$
\begin{aligned}
T_{unb} &= m_p \Delta z \frac{d^2}{dt^2}\left(x_m \sin \omega t\right) \\
&= m_p \Delta z \, \omega^2 \left(x_m \sin \omega t\right)
\end{aligned}
\tag{4.5-1}
$$

Substituting the unbalance torque (4.5-1) into the simplified equation of motion (neglecting the periodic terms) represented by Eqn. (2.4-5), gives

$$
\ddot{\theta} + \frac{\omega}{Q}\dot{\theta} + \omega^2 \theta = -m_p \Delta z \, \omega^2 (x_m \sin \omega t) \ .
\tag{4.5-2}
$$

The response to the unbalance torque is determined by solving Eqn. (4.5-2) to give

$$
\theta_{unb}(t) = \frac{m_p \Delta z \, x_m Q}{I_0} \cos \omega t \ .
\tag{4.5-3}
$$

97
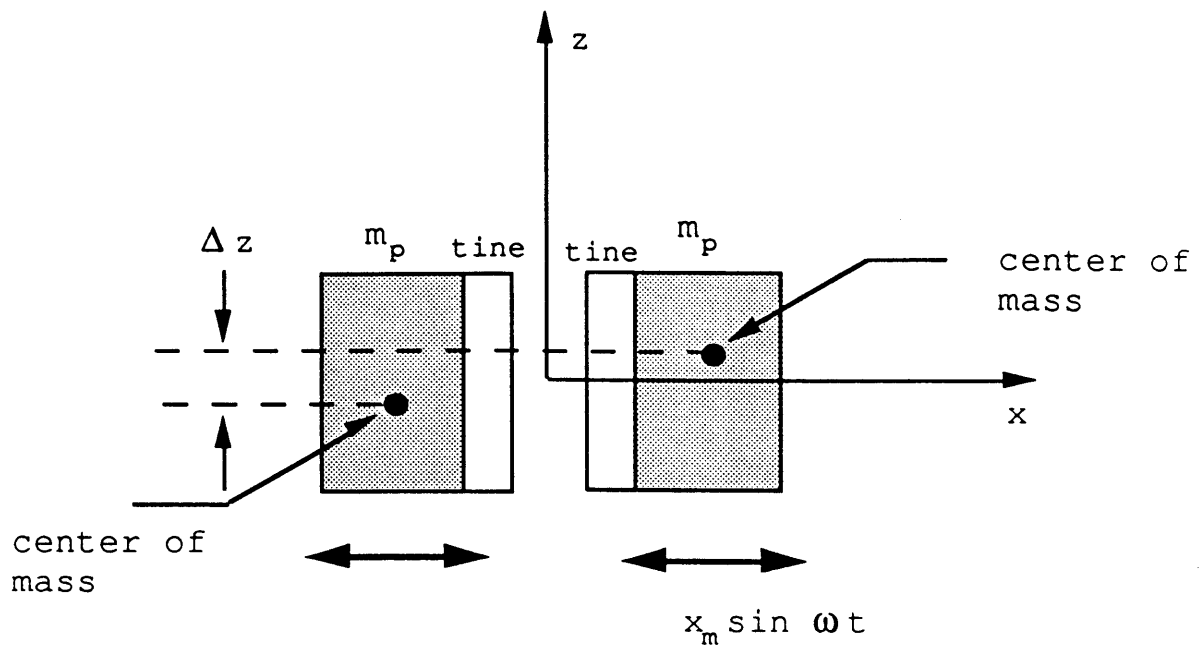
Figure 4.8 Unbalance Torque from Proof Mass Misalignment

The response to the unbalance is seen to be in quadrature with the gyroscopic response, and the demodulation will prevent the unbalance from resulting in an output signal. But, the proof mass tolerance must be within the limit

$$\Delta z \; < \; \frac{\theta_{max} \, I_0}{x_m \, Q \, m_p} \; = \; \frac{2 \, I_0 \, g}{W_x \, x_m \, Q \, m_p} \; .$$

(4.5-4)

This insures that the unbalance torque will not cause the sensor wing to strike the electrode plate.

Random Errors

98

There are two identified noise inputs into the system that will limit the accuracy of the output signal. The first is random thermal noise, which will be referred to as *Brownian Noise*. As the wings oscillate, the thermal energy in the air causes a random movement of the air molecules which leads to a random torque on the wings. This torque is generally negligable for conventional scale systems. But, for a micromechanical resonator, the system energy is small enough that the thermal energy is significant.

The Brownian Noise is modeled as a white noise entering the system at the torque summing junction as shown in Figure 4.9. The amplitude of the white noise is assumed to be

$$A_B = 2 T_{ab} K_B b_t .$$ (4.5-5)

where,

$$K_B = \text{Boltzmann's constant}$$

$$T_{ab} = \text{absolute temperature}$$

$$b_t = \text{linear damping coefficient}$$

The noise propagates through the system and results in a variance of the output. The relationship between the Brownian noise and the output signal is

$$x(t) = G_1(s) A_B$$

where,

$$x(t) = e_{out}(t) \qquad \text{(output voltage signal)}$$

$$G_1(s) = \frac{K_\theta K_e \, B/b}{(s + a)(s + B)}$$ (4.5-6)

$$a = \frac{\omega}{2Q} , \qquad b = I_0 \omega$$

$$B = \text{filter bandwidth} \quad (B = \frac{1}{20} \text{ Hz for calculations })$$

The constants in Eqn. (4.5-6) are explained in Figure 4.9. The output signal can be written as the convolution of the noise input and the transfer function [28] written in the time domain,

$$x(t) = \int_0^t g_1(u)\, n_1(t-u)\, du \quad .$$

(4.5-7)

Taking the inverse Laplace transform of the transfer function gives

$$g_1(u) = \frac{K_\theta K_e B}{b} \int_0^t e^{-a\tau} e^{-B(t-\tau)} d\tau$$

$$= \frac{K_\theta K_e B}{b(a-B)} \left[e^{-Bt}\, e^{-at} \right] \quad .$$

(4.5-8)

The system is assumed to be *stationary* such that the variance of the output is written

$$\sigma^2 = E\left[x(t_1)\, x(t_2) \right] = E\left[x^2(t) \right] \quad .$$

(4.5-9)

Substituting Eqn. (4.5-7) into (4.5-9) and noting that $g_1(u)$ is deterministic

$$\sigma^2 = \int_0^t \int_0^t g_1(u)\, g_1(v)\, E\left[n_1(t-u)\, n_1(t-v) \right]\, du\, dv$$

$$= \int_0^t \int_0^t g_1(u)\, g_1(v)\, A_B\, \delta(u-v)\, du\, dv$$

(4.5-10)

where $\delta(u-v)$ is the *Dirac delta function* .

Substituting Eqn. (4.5-8) into (4.5-10) gives

$$\sigma^2 = \int_0^t \int_0^t \left[\frac{K_\theta K_e B}{b(a-B)} \right]^2 \left(e^{-Bu}\, e^{-au} \right) \left(e^{-Bv}\, e^{-av} \right) A_B\, \delta(u-v)\, du\, dv \quad .$$

(4.5-11)

Solving the double integral yields the result

$$\sigma^2 = \frac{A_B K_\theta^2 K_e^2 B}{2\,b^2 a(a+B)} - \frac{A_B K_\theta^2 K_e^2 B}{2\,b^2(a-B)^2} e^{-2Bt} + \frac{2\,A_B K_\theta^2 K_e^2 B^2}{(a+B)\,b^2\,(a-B)^2} e^{-(a+B)t} - \frac{A_B K_\theta^2 K_e^2 B^2}{2\,b^2 a(a-B)^2} e^{-2at} \,.$$

$$(4.5\text{-}12)$$

The steady state variance due to the Brownian noise input is then

$$\sigma_{ss,B}^2 = \frac{A_B K_\theta^2 K_e^2 B}{2\,b^2\,a\,(a+B)}$$

$$(4.5\text{-}13)$$

The effect of the Brownian noise on the system output has some interesting characteristics. In general, the bandwidth of the low pass filter, B, will be small compared to the system bandwidth, a. The Brownian noise variance is then inversely proportional to the square of the system bandwith. Substituting for the system bandwidth (2.5-6), the amplitude of the Brownian noise (4.5-5), and the dynamics constant $b = I_0 \omega$, gives

$$\sigma_{ss,B}^2 = \left(4\,T_{ab} K_B K_e^2 K_\theta^2\right) \frac{B\,Q}{I_0^3 \omega}\,.$$

$$(4.5\text{-}14)$$

Assuming that the capacitance constant, electronics constant, and temperature are all fixed, then the Brownian noise variance is a function of B, Q, I_0, and ω. A very interesting obserbation from (4.5-14) is that the variance is proportional to Q. At first glance, this seems contradictory. Since as Q increases the damping decreases and the effect of the random molecular movement is reduced, it would seem that this would reduce the variance. But, increasing Q reduces the system bandwidth which has a squared effect on the variance to offset the first order decrease in Brownian Noise amplitude. To minimize the Brownian Noise error, the system should be designed to have a high system bandwidth to filter bandwidth ratio. Also, by increasing the size of the gyro, the Brownian error will be reduced.

In addition to Brownian noise, there is an additional random noise input into the system as shown in Figure 4.9. The amplifier of the signal processing electronics contains an inherent random noise. The noise input enters the system at the ΔC signal summing junction. The amplifier noise is assumed to be white and stationary with an amplitude denoted by A_a. The exact value of A_a is determined from the amplifier specifications, but in the calculations presented here the assumed value is

$$A_a = 3.3 \text{ E-28 } A^2/\text{hz} .$$

This value corresponds to the specifications of a typical amplifier for the electronics confguration modeled in Section 4.2.

The variance of the output due to the amplifier noise is determined by following the same steps used for the Brownian noise. Denoting the amplifier noise by n_2 the input-output relationship is

$$x(t) = G_2(s) \, n_2(t)$$

where,

$$G_2(s) = \frac{K_1 \, K_\theta \, K_e \, B}{s + B}$$

$$K_1 = \frac{1}{\omega_x \, E_x} . \tag{4.5-15}$$

Taking the inverse Laplace transform of the transfer function,

$$g_2(u) = K_1 \, K_e \, K_\theta \, e^{-Bu}. \tag{4.5-16}$$

Substituting the expressions for A_a and $g_2(u)$ into double integral of Eqn. (4.5-10), the expression for the output variance due to amplifier noise becomes

$$\sigma_a^2 = K_1^2 K_\theta^2 K_e^2 B^2 A_a \int_0^t e^{-2Bv} \, dv . \tag{4.5-17}$$

Integrating, and looking only at the steady state term, the variance due to amplifer is

$$\sigma_{ss,a}^2 = \frac{K_1^2 K_\theta^2 K_e^2 B A_a}{2} . \tag{4.5-18}$$

102

It is seen that the most efficient methods to reduce the amplifier noise error are to decrease the filter bandwidth, or to decrease the excitation constant.

input rate
Ω

gyro
multiplier

$I_1 \omega$

n_1 Brownian noise
$A = 2 \, T_{ab} K_B \, b \, (Nm)^2/hz$

cos $\omega_d t$

Π

Σ Torque

dynamics

$$\frac{1}{b \, (s + a)}$$

low pass
filter with
bandwidth, B

electronics
constant

capacitance
constant

$$\frac{1}{1 + s/B}$$

K_e

Σ

DC

K_θ

θ

e_{out}

output voltage

K_1

excitation
constant

n_2 amplifier noise
$A_a = 3.3 \ E-28 \ \overset{2}{A}/hz$
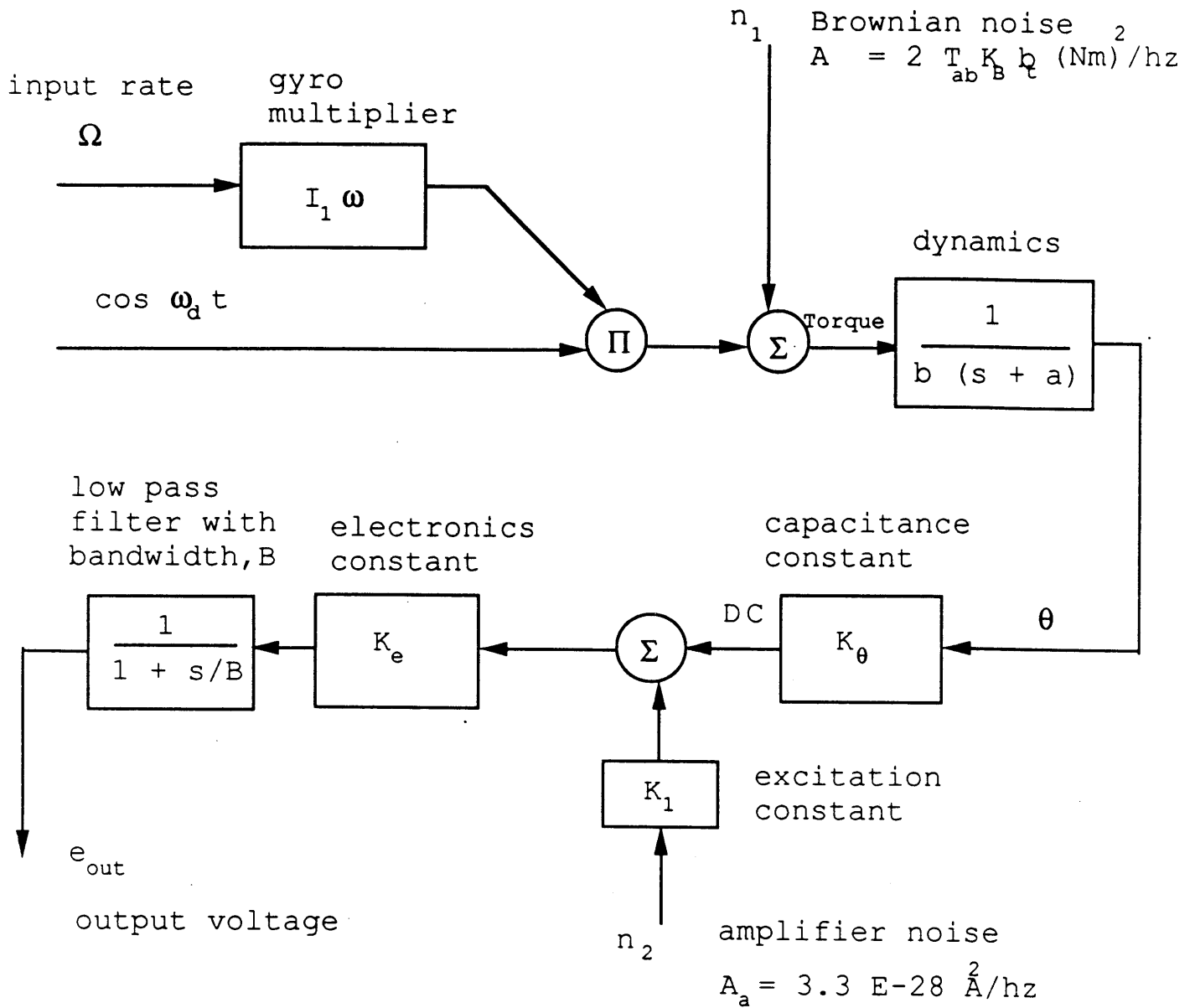
$$K_1 = \frac{1}{\omega_x E_x} \qquad \text{(excitation frequency and voltage)}$$

$$K_\theta = \frac{(x_1 + x_2) \, C_0}{2g} \qquad \text{(Eqn. 4.2-4)}$$

$$K_e = \frac{100 \, (2/\pi) \, E_x}{C_{fb}} \qquad \text{(Eqn. 4.2-5)}$$

Figure 4.9 System Diagram with Noise Inputs

104

5   DESIGN

The previous chapters have laid the mathematical foundation upon which a baseline design is developed. The main difficulty in developing a design of a micromechanical tuning fork gyroscope is that there exists no precedent. The only test results available to support the design are from the Boxenhorn gyroscope [1] and the observations from the demonstration model. For these reasons, the only design tool is the system mathematical model.

The system mathematical model is implemented into a computer program written in PASCAL programming language and run on an IBM PC. The design program uses an inputted set of device dimensions and system parameters and outputs a set of performance predictions. The program allows design tradeoff studies to be performed interactively. At this early stage in the design of the gyro, the design program is only a very rough model of the device. It includes models for the physical characteristics that were identified in the previous chapters. As the investigation into the gyro design continues, the program will quickly grow as additional system characteristics are identified.

In this chapter, the performance predictions for a set of baseline design parameters are discussed. A printout of the program output for the baseline design is listed in Table 5.1. The design is determined considering *geometric constraints* and *performance tradeoffs*, and they are the basis of the two sections of this chapter. It must be noted that the design is not rigorously optimized. The tradeoffs are analyzed to the point of producing an *acceptable* performance level. Optimization is left for a future study.

105

5.1 Geometric Constraints

The geometry of micromechanical structures is restricted by the fabrication techniques. The micromachining techniques were originally developed by the semiconductor industry to etch circuit lines on microchips, and they were basically limited to simple, planar geometries. Although the advent of micromechanical structures has greatly increased micromachining technology, there are still broad limitations on possible geometric configurations.

It is difficult to exactly specify the geometric limits of micromachining since new techniques are being invented daily. In this chapter, a set of *assumed restrictions* are specified. They are based on state-of-the-art technology and resources available at the Charles Stark Draper Laboratory. The assumptions are conservative and are derived from the input of technicians and engineers within Draper's micromachining laboratory.

Figure 5.1 shows a sketch of the geometry of the baseline design. The figure only shows one half of the device which is symmetric about the gold bar (x-axis). The first geometric restrictions involve the tines. The ratio of the height of each tine to its width is assumed to be limited to

$$(h : w) \quad < \quad 15 : 4 . \tag{5.1-1}$$

Also, the value for the distance between the tines is restricted by a minimum value,

$$d \quad > \quad 4 \quad \text{microns} . \tag{5.1-2}$$

Since micromechanical fabrication processes are best suited for planar structures (z-dimensions less than a few microns), the fabrication of the tines requires the most complicated micromachining procedures for the gyro. Generally, precise geometries are patterned by standard photolithographic techniques, and shallow etches cut through the silicon wafer [23] to form a specific structure. However, a *deep etch* is required for fabricating the tines. Anisotropic deep etching must be done along one of the weakly

106

bound silicon crystal planes. Generally, this requires a cut angled at about 54 degrees from the vertical. An additional procedure to fabricate a vertical structrure is then required [22].

It is also assumed that there exists a minimum gap between the sensor wing and the bridge electrode such that

$$g \quad > \quad 12 \quad microns \ . \tag{5.1-3}$$

The bridge electrodes are metallized onto a seperate plate which is suspended over the gyro by bonding the plate to the silicon wafer. The sensor gap restriction is a conservative estimate of the z-dimensional tolerance for situating the plate. Furthermore, the depth of the strain beam is assumed equal to the depth of the sensor wing,

$$b_z \quad = \quad W_z \ . \tag{5.1-4}$$

This is meant to simplify the fabrication so that seperate diffusions are not needed.

The two inertial masses consist of rectangular gold bars. Gold is chosen because of its high density and its compatibility with the fabrication process. The gold is attached to the tine by either *metallization* or *electroplating* [30]. For either technique, it is assumed that the height of the gold bar is equal to the height of the tine,

$$m_z \quad = \quad h \ . \tag{5.1-5}$$

Also, it is assumed that the gold can only extend from the tine in the x-direction a maximim distancesuch that

$$m_x \quad < \quad 80 \quad microns \ . \tag{5.1-6}$$

Again, these are fabrication restrictions.

The dimension representing the thickness of the flexures, f_z , is not an input quantity. Instead, the system driving frequency, which is matched to the torsional resonant frequency, is an input. The flexure thickness is calculated from the stiffness model presented in Section 4.3 for given values of the flexure width, f_x , length, f_y , and system frequency, ω_0. A loop in the program iterates the flexure thickness until the desired frequency is obtained. The system frequency is chosen as a design input instead of the flexure thickness because it is more significant in terms of the entire *system* design.

The fabrication of the sensor wings is complicated by the requirement that the sides of each wing are *electrically isolated* from each other. Electrical isolation eliminates the need to lay wires across the flexures and wings in order to apply a differential voltage across the tines. Instead, a differential voltage is applied across the two flexures. The semiconductor properties of silicon allow the potential to transfer to the tines. Thin diagonal slots are cut through the wings from a point between the tines to one side of the flexure. This allows each flexure to be electically connected to a different tine. The two sides of the wing are connected by a *lap joint* shown in Figure 5.1. An oxide covering in a rectangular pattern is laid over the slot. The oxide is covered by a polysilicon layer a few microns thick which adds structural integrity to the wing. It is seen that the width of the lap joint must be at least the width of the flexure. An apparant disadvantage of the lap joint is that it reduces the capacitance area of the sensors. The lap joint forces an x-dimensional gap between the sensor plates which is denoted by the variable *sensgap* in the program where,

$$sensgap = 2x_1. \qquad (5.1-7)$$

for x_1 defined in the sensor model of Eqn. (4.2-4). Then, assuming that the lap joint is at least twice the flexure thickness, the variable x_1 is restricted by

$$x_1 > f_x. \qquad (5.1-8)$$

The top portion of Table 5.1 lists the device geometry with the dimensions in microns. The constrained parameters d, h, w, g, m_x, and *sensgap* are all set at the limit which maximizes the gyroscopic sensitivity. The tine aspect ratio is set as high as possible, 15 : 4 microns, to maximize the tine deflection per applied driving volt. The inertial mass dimension, m_x, is also set at its limit (5.1-6) to maximize the mechanical gain. The gap between the bridge electrodes is set at its minimum value to maximize the sensor area (5.1-8).

The geometric parameters that remain available for design tradeoffs include:

l	length of tines ,
m_y	y-dim of gold bar ,
W_x , W_y , W_z	dimensions of wings ,
f_x , f_y	dimensions of flexures , and
b_x , b_y	dimensions of strain beam .

For simplicity purposes, it is also assumed that the driving frequency, driving voltage, and electronics configuration are fixed by the system requirements. The frequency is set at

$$\omega = 2 \text{ kHz}$$

and the differential driving voltage is set at

$$V_d = 20 \text{ V} . \tag{5.1-9}$$

This specific driving voltage supplies adequate motor force and is also easily compatible with a typical motor electronics configuration. A frequency of 2 kHz is chosen since it has been shown to be an effective frequency for the Boxenhorn micromechanical gyroscope [2].

5.2 Performance Tradeoffs

The remaining design parameters are chosen to produce a reasonable performance level of the gyro. The performance is defined as a balance between sensitivity and errors. In this section, each design parameter is analyzed separately in terms of the modeled performance characteristics that it affects.

length of tines and y-dim of mass :

To increase the mechanical gain of the gyro, the length of the tines and the dimensions of the mass are made as large as possible. Long tines increase the area for the motor electrostatic force and decrease its lateral stiffness. The mass of the gold bar also increases the mechanical gain as shown in Eqn. (4.1-30). The foremost limiting restraint is the estimated stability limit. For the baseline design the stability parameter is

$$\varepsilon Q \;=\; 3.16 \,. \tag{5.2-1}$$

This falls within the linear response region as shown in Chapter 3.

Also, the amplitude of the tine vibration cannot exceed one-half of the gap between the tines. A maximum value for the ratio of the tine amplitude to one-half of the tine gap is defined as

$$u_2 = \frac{x_m}{d/2} \;<\; 0.25 \,. \tag{5.2-2}$$

This ratio should insure that the tines do not strike each other, and it is small enough to satisfy the assumptions used in deriving the motor model in Chapter 4.1. Also, the tine length must obey the constraint of Eqn. (2.22-3) which guarantees that the tine twisting mode will not be excited. The twisting resonant frequency is listed in Table 5.1 under the "Dynamic Characteristics" heading. For the baseline design, the frequency of the tine twisting mode is more than a factor of six greater than system frequency.

The program variable, *phi* , listed under the "Motor Characteristics" heading, is defined as the static twist angle of each tine for a z-direction gravitational acceleration. The twist occurs because the gold bar center of mass is not aligned with the tine center of mass. For the baseline design, m_y and l were chosen such that *phi* is less than two degrees for an acceleration of 100 g's.

Throughout the analysis of the gyroscope, it was assumed that the natural frequency of each tine is greater than the driving frequency. This was meant to simplify the analysis. However, if the length of the tine is adjusted to yield a tine frequency which is

near the driving frequency, the mechanical gain increases per driving volt. The gain from operating near resonance is defined as the *dynamic load factor* [9]. For the tines,

$$d \, l \, f_{tine} = \frac{1}{1 - \left(\dfrac{\omega_0}{\omega_{tine}}\right)^2}$$

(5.2-3)

The baseline design capitalizes on the resonance gain to limit the necessary driving voltage. The design fixes the tine frequency only 15% higher than the driving frequency to yield a dynamic load factor of 4.63.

wing dimensions :

To maximize the gyro sensitivity, the wing area is made as large as possible. The output signal is linearly related to the nominal parallel plate capacitance, C_0, by Eqn. (4.2-3). But, increasing the sensor area has no effect on the gyro signal to noise ratio since the capacitance constant present in the random noise equations (4.5-14) and (4.5-18) is also linearly proportional to C_0. The standard deviation of the noise thus increases at the same rate as the sensitivity. However, increasing the length of the wing, W_x, has an added effect on the sensitivity, besides increasing the capacitor area. Eqn. (4.2-4) indicates that $x_2 = \frac{W_x}{2}$ is a linear factor of the sensitivity. It is thus advantageous for the x-dimension of the wing to exceed the y-dimension.

The wing dimensions strongly influence the magnitude of the air damping. For the pumping effect of Eqn. (4.4-16), the damping force is linearly related to W_x^4. A successful design tradeoff between low air damping and reasonable sensitivity could not be obtained. Instead, the baseline design assumes a vacuum package that fixes the quality factor at $Q = 200$. This value was chosen because it allows a reasonable device sensitivity,

$$e_{out} = 0.47 \text{ millivolts per rad/sec} \qquad (5.2\text{-}4)$$

while maintaining a system bandwidth of 5 Hz which is significant for noise rejection. For the baseline design dimensions the Q estimate for air damping is

$$Q = 2.9 . \qquad (5.2\text{-}5)$$

The damping force due to the air pumping is two orders of magnitude greater than the flow impingement damping force, as listed in Table 5.1 under "Dynamic Characteristics". This means that if the gyro is to be efficiently operated in air, the sensor wings must be designed with slits to reduce the air pumping.

flexure and strain beam dimensions :

The length and width of the flexures are chosen such that the calculated thickness for the desired frequency is in a practical range. This generally means that the flexure thickness is between

$$0.25 \text{ microns} < f_z < 2.0 \text{ microns} . \qquad (5.2\text{-}6)$$

The flexure dimensions are constrained only by Eqn. (2.2-6) which guarantees that the flexure bending will not be excited. For the baseline design, the flexure thickness is

$$f_z = 0.6 \text{ microns} .$$

The strain beam dimensions are chosen to keep the maximum principle stress on the flexures less than 1% of the yield strength. for silicon, the yield strength is assumed [25] to be

$$YS = 4.4 \text{ E9 } N/m^2 .$$

For the baseline design, the strain beam alleviates the stress caused by a 0.2 micron boron diffusion contraction deflection into a maximum principal stress of only 0.38% of the yield strength.

to electronics

$E_x + \dfrac{V_d}{2}\sin wt$

substrate

strain beam slot

Si

bridge electrode

electrical isolation slot

Si

lap joint

bridge electrode

Si

oxide covering

polysilicon layer

Si

plated gold

Au

z

y

x
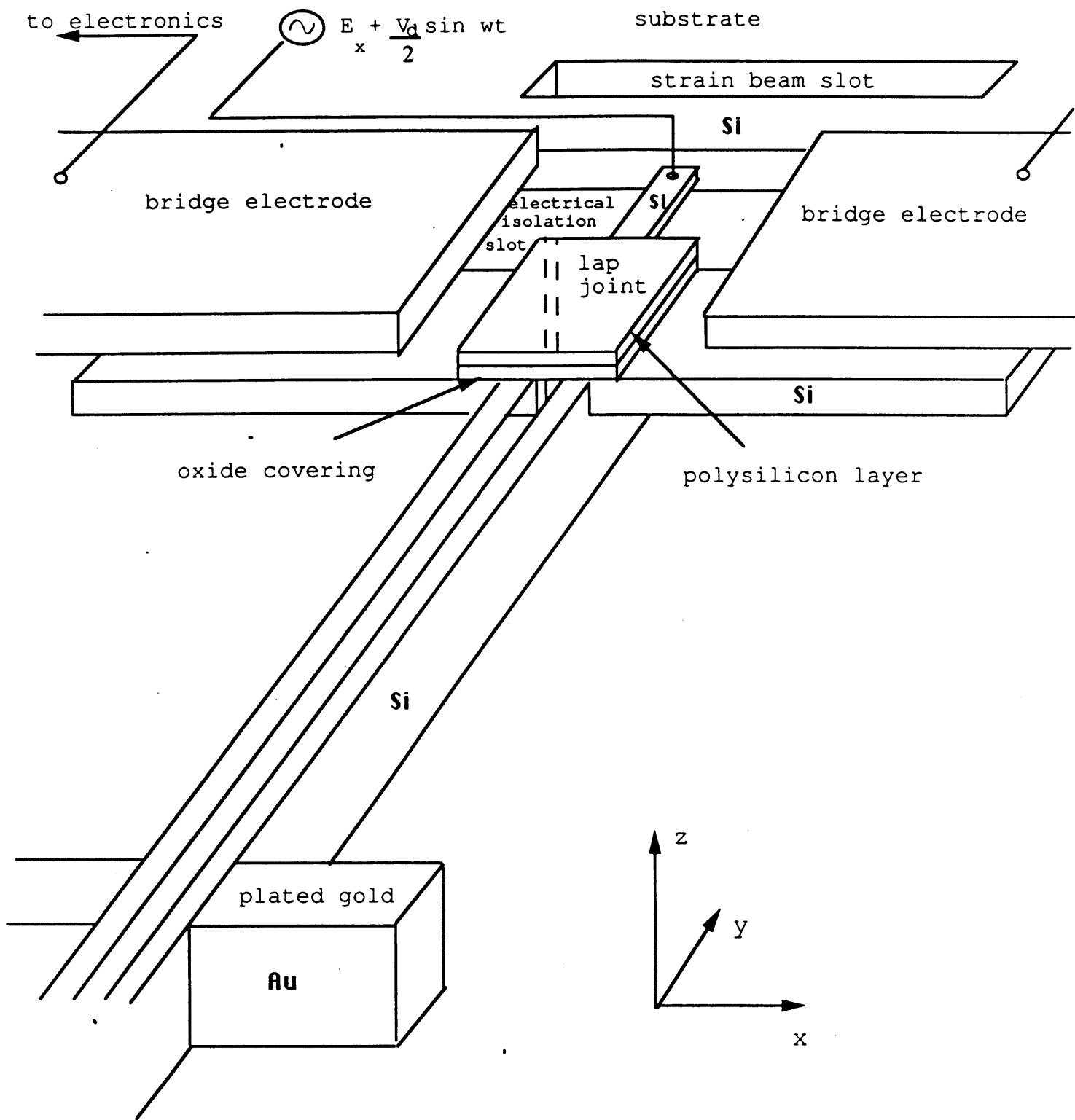
Figure 5.1 Design Sketch

113

TUNING FORK MICROMECHANICAL GYROSCOPE PERFORMANCE
****

++++++++++++++++++GEOMETRY++++++++++++++++++++++

l	700.00	microns	length of tines
d	4.00	microns	gap between tines
w	4.00	microns	width of tines
h	15.00	microns	height of tines
mx	80.00	microns	width of inertial mass
my	50.00	microns	length of inertial mass
Wx	160.00	microns	length of wings
Wy	120.00	microns	width of wings
Wz	3.00	microns	height of wings
g	12.00	microns	sensor gap
fx	10.00	microns	width of flexures
fy	40.00	microns	length of flexures
fz	0.61	microns	thickness of flexures
sensgap	20.00	microns	gap between sensor electrode plates
bx	200.00	microns	length of strain beam
by	8.00	microns	width of strain beam
bz	3.00	microns	substrate thickness

++++++++++++++++++MECHANICAL PROPERTIES+++++++

massg	1.2E-0009	kg	mass of each gold bar
masst	9.7E-0011	kg	mass of each tine
massw	1.3E-0010	kg	mass of each wing
masstot	2.8E-0009	kg	total mass of structure
Ibeamt	8.0E-0023	m^4	beam area inertia for tines
Ibeamw	2.7E-0022	m^4	beam area inertia for wings
It	3.5E-0021	Kgm^2	mass moment of inertia for tines
Im	3.1E-0018	Kgm^2	mass moment of inertia for gold bars
Iw	2.8E-0019	Kgm^2	mass moment of inertia for wings
Io	6.8E-0018	Kgm^2	total nominal mass momt of inertia
Iox	5.3E-0017	Kgm^2	mass momt. of inertia, x-axis
Ioz	6.0E-0017	Kgm^2	mass momt. of inertia, z-axis
pmps	3.8E-0001	%	percent max princ. stress on flexures

++++++++++++++++++MOTOR CHARACTERISTICS+++++++

Vd	20.00	Volts	differential driving voltage
F1	1.2E-0006	N	electrostatic force, parallel plates
F2	3.4E-0007	N	electrostatic force, fringing
Fo	1.5E-0006	N	total electrostatic force
ym	.4.6E-0001	microns	tine midpoint drive amplitude
phi	2.9E-0002	degrees	tine rotation angle per z-dir g
u2	2.3E-0001	unitless	ratio of drive amplitude to maximum
I1	1.1E-0019	kgm^2	variable inertia term

Table 5.1

```
+++++++++++++++++DYNAMIC CHARACTERISTICS++++++++

BWol        5.000      Hz         open loop system bandwidth
wtineb      2.258      kHz        tine fundamental frequency
wwing       564.423    kHz        wing fundamental frequency
wtwist      12.640     kHz        tine twisting frequency
wo          2.000      kHz        driving frequency
dlft        4.63       unitless   dynamic load factor, tines
dlfw        1.00       unitless   dynamic load factor, wings
dlftw       1.03       unitless   dynamic load factor, tine twisting
Q           200.00     unitless   system amplification factor
Qair        2.93       unitless   Q if operated at atmospheric pressure
Qvac        200.00     unitless   assumed Q from vacuum chamber
Fpu         4.5E-0006  N          damping force due to pumping
Fpl         2.3E-0008  N          damping force due to flow around plate


+++++++++++++++++++GYRO OUTPUT+++++++++++++++

omega       1.00       rad/sec    input rate
eps         1.6E-0002  unitless   inertia ratio - mechanical gain term
stabrat     0.913      unitless   open loop stability ratio
theta       1.4E-0002  degrees    output vibration amplitude
theta       0.8655     minutes
thmax       8.5960     degrees    maximum vibration amplitude
ul          0.0017     unitless   ratio of output to max output
gtor        1.3E-0015  Nm         gyroscopic torque
gtor        1.3E-0004  dyne-mic
Co          6.2E-0015  farads     nominal sensor capacitance
delC        2.3E-0017  farads     change in capacitance
eout        0.474      mVolts     output signal


+++++++++++++++++++ERROR SOURCES++++++++++++++++

sigbrn      2.6E-0007  volts      Brownian noise standard deviation
sigamp      2.3E-0007  volts      amplifier noise standard deviation
SNrat       956.70     unitless   output signal to noise ratio
zunb        0.750      microns    assumed tolerance of gold mass in z-dir
thquadu     0.6761     degrees    unbalance quadrature output
ulq         0.079      unitless   ratio of quad output to max
del         0.200      microns    boron diffusion contraction on flexures
ps          1.7E+0007  N/m^2      axial pre-stress on flexures


                End of Output
                -------------
```

Table 5.1 (continued)

6   CONCLUSIONS

From the baseline design and performance predictions described in the previous chapter, it is safe to conclude that the micromechanical tuning fork gyroscope merits furthur investigation. The gyro sensitivity is shown to be at a reasonable level relative to the possible applications. The output voltage is predicted to be

$$e_{out} = 0.47 \text{ millivolts per rad/sec} .$$

None of the identified error sources appear to fundamentally limit the effectiveness of the gyro as an angular rate sensor. By modeling the effect of the error sources, the output signal to noise ratio is predicted at

$$S/N = 957$$

which translates to a minimum detectable rate of

$$\Omega_{min} = 218 \text{ deg/hr} .$$

Originally, the biggest question concerning the feasibility of the device was whether the periodic terms present in the equation of motion would lead the system response to become nonlinear. The high frequency and low damping necessary for a micromechanical instrument increase the significance of the periodic terms.

This question was adressed in Chapter 2 and it was shown that the response is linear and stable within a specified parameter region. A sufficient condition for stability was determined by transforming the equation of motion to the Mathieu equation. The stability condition is

$$\varepsilon Q < \sqrt{12}$$

where,

$$\varepsilon \equiv \frac{I_1}{I_0}$$

$$Q \equiv \text{system quality factor}.$$

116

The stability was checked by applying Floquet Theory to the LP equation of motion. The eigenvalues of the system discrete state transition matrix were shown numerically to lie within the complex unit circle for the region specified above.

If the periodic terms in the equation of motion are neglected, the output of the gyroscope, written in terms of the rotation angle, is a linear function of the input rate

$$\theta (t) = -\frac{\varepsilon Q}{\omega} \Omega \sin \omega t .$$

With the periodic terms included, the system response was approximated by a Fourier series. It was shown that the linear approximation above is valid for the region

$$\varepsilon Q < 4 .$$

For values of the stability parameter (εQ) exceeding four, an output phase shift occurs, the first sine harmonic component decreases, and higher harmonic terms become more significant. The linear response within the specified region was further verified by numerical simulation.

The next feasibility concern stemmed from the demonstration model. It questioned whether undesirable vibration modes would be excited. From a model of the mechanics, it was shown that the device is easily designed to be rigid. The most significant mode is twisting of each tine about its longitudinal axis. For the baseline design, the frequency of this mode was shown to be more than a factor of six greater than the system frequency.

Brownian noise is a problem that plagues the design of any micromechanical instrument. The low energy levels of micromechanical instruments can lead to Brownian noise levels that restrict instrument effectiveness. However, for the baseline design presented in this paper, the error due to the Brownian noise is on the same order as the amplifier noise. Hence, Brownian noise is not a dominating error source. In fact, none of the identified error sources are shown to dominate. These include cross-axis sensitivity, external acceleration and vibration, motor-sensor coupling, and unbalance torques.

The only major disappointment from the performance predictions is the requirement of a vacuum package. It was previously believed that the air damping for a tuning fork configuration might be low enough to eliminate the need of a controlled pressure chamber. However, the air flow through the channel defined by each sensor wing and its bridge electrode, which is pumped by the oscillating wing, creates a substantial pressure drop across each wing. Therefore, unless a specific damping reduction design is implemented, the tuning fork gyro will be most efficiently operated in a vacuum. The baseline design study shows that a moderate vacuum quality factor of $Q = 200$ will yield reasonable sensitivity and open loop bandwidth.

The baseline design bandwidth of 5 Hz is obviously not adequate for many angular rate sensor applications. This implies that the gyro must be operated with a closed-loop rebalance servo to satisfy the requirements of some possible applications. Then the system designer could choose the closed-loop bandwidth depending on the requirements of the particular application. In this paper, the gyro is studied strictly from an open-loop standpoint. The closed-loop design is left as future research.

In order to put the gyro performance predictions in their proper perspective, comparisons to other angular rate sensors are made. First, the tuning fork configuration is compared to Boxenhorn's double gimbal configuration [1,2]. The gyro is then compared to previously developed tuning fork gyroscopes. The comparison is presented in an attempt to convince the reader that a tuning fork gyroscope on a micromechanical level has success potential, even though many conventional scale tuning fork gyroscope development efforts have failed.

6.1 Comparison with Current Micromechanical Gyro Configuration

Table 6.1 lists various characteristics of the current double gimbal micromechanical configuration next to the corresponding tuning fork characteristics. The original goal of the

118

tuning fork study was to determine if the configuration can give performance levels competitive with the current configuration. The unique property of the tuning fork configuration is that the input axis is in the same plane as the gyro chip. Therefore, if a competitive performance level is obtained, the two micromechanical configurations can be combined for various system applications.

As seen from the table, the two configurations have similar characteristics. Yet, it is seen that in a few regards the tuning fork configuration has properties which are more favorable than the current configuration. The observed favorable and unfavorable comparisons are listed and described below:

Favorable Properties of Tuning Fork Configuration:

1) More gyroscopic torque is possible. The gyroscopic torque of the current configuration is a function of the driver angle which is limited to very small values.

2) Motor-sensor coupling is reduced. No electric flux from the tuning fork motor crosses the resonator gap.

3) Only one set of flexures is needed. This increases the reliability. Also, the second set of flexures can lead to high stress levels and buckling from boron diffusion deflections.

4) No sticking from a rotational motor. The lateral motor of the tuning fork eliminates the problem of sticking from motor startup instability.

119

<u>Unfavorable Properties of Tuning Fork Configuration:</u>

1)   The motor is nonlinear. For an effective device, the motor deflection must be sensed and driven simultaneously in an appropriate scheme to linearize the relationship between the mechanical gain and the driving voltage.

2)   Difficult fabrication of vertical tines. Unique fabrication processes are required to make the tines vertical with a high aspect ratio.

3)   Smaller sensor area. A gimballed structure has more available area for the sensor plates.

4)   The tuning fork configuration is unproven. No testing has been performed.

It is possible that further research could eliminate the unfavorable characteristics. The most important favorable characteristic is the high gyroscopic torque. As seen from Table 6.1 the tuning fork gyroscopic torque is more than one order of magnitude greater than the current configuration. This is an advantage of the lateral electorstatic motor which was extensively modeled in Chapter 4.1. High gyroscopic torque is essential to increase the output signal-to-noise ratio.

6.2   Comparison with Previously Developed Tuning Fork Gyros

Table 6.2 lists the characteristics of two previously developed tuning fork gyroscopes. The Sperry Gyrotron was introduced more than 30 years ago and is not still available. Its characteristics as listed are obtained from Reference [3]. The other tuning fork gyroscope listed is the Watson Angular Rate Sensor (ARS). The ARS is a solid state

device which is currently commercially available, and its characteristics are obtained from a manufacturer specification sheet.

The primary differences between these two devices and the micromechanical tuning fork gyro are size and power. Also, it must be noted that both of these devices require that the tine natural frequency is tuned to the torsional natural frequency. This requires precision testing on each individual device. A list of favorable and unfavorable comparisons between the micromechanical tuning fork gyro and the other tuning fork gyros is shown below:

<u>Favorable Properties of Micromechanical Tuning Fork</u> :

1)   High frequency. The micromechanical tuning fork gyro is routinely driven at frequencies between 1 and 5 khz which subdues zero rate errors.

2)   Constant damping and temperature packaging more feasible due to small size. The system characteristics are more easily controlled in a small package.

3)   Torsional to lateral tuning not necessary. Tuning the tine frequency to the torsional frequency increases the cost and manufacturing complexity. The micromechanical configuration does not require this.

4)   No joints or bearings. This reduces hysterises effects, structural damping, and stress concentration areas.

5)   Small fabrication tolerances. Microfabrication techniques produce precise dimensions. Symmetrical devices are easily produced, and unbalance and misalignment effects are minimized.

6)   Low cost / small size. The bottom line is that the large scale tuning fork gyroscope is not successful because it cannot compete with high accuracy,

121

conventional gyroscopes. However, the micromechanical tuning fork gyroscope attacks a different market. The unique qualities of a micromechanical instrument open up applications where only moderate accuracy is needed.

6.3   Future Research

The author hopes that this paper will inspire a continued study into the design of a micromechanical tuning fork gyroscope. A long road lies ahead, but it is the resounding conclusion that a micromechanical tuning fork gyroscope could be extremely successful. Throughout the world, micromechanical engineering is an active research topic. The efficiency of micromechanical fabrication and testing procedures is increasing continuously. It is possible to forecast that soon into the next century the sensor field will be dominated by micromechanical instruments.

A few areas that would make interesting research topics in a continued study of the micromechanical tuning fork gyroscope are mentioned here. First, it is necessary to linearize the motor. This would require an extensive model of the electrostatics and a design scheme that would sense the tine deflection while simultaneously driving the tines. Another possible research area is a fluid mechanics study to model the quality factor of the resonator. Because the system Q is an important design parameter, it would be helpful to develop methods to predict and regulate the damping. The mechanical properties of the device are also largely unexplored. The stiffness properties of the flexures could be investigated in terms of thermal effects, fatigue effects, and residual stresses from the fabrication processes.

A continued design study could lead to prototype fabrication and testing. Then, further down the road, a closed loop design for the device could be investigated followed by a complete inertial system study.

COMPARISON OF MICROMECHANICAL TUNING FORK
GYRO DESIGN TO CURRENT MICROGYRO

	TUNING FORK	CURRENT MICROGYRO
CONFIGURATION	single gimbal, closed fork	double gimbal, vibratory
MOTOR	electrostatic, lateral (nonlinear)	electrostatic, rotational
SENSOR	variable capacitance	variable capacitance
INPUT AXIS	in-plane, fork stem	normal to plane
MATERIAL	silicon chip	silicon chip
PACKAGING	temp. controlled, vacuum	temp. controlled, vacuum
SIZE	4.9 E-12 m^3	8.6 E-12 m^3
MASS	2.8 E-9 kg	9.41 E-9 kg
POWER	order of 1.0 E-12 W	order of 1.0 E-12 W
FREQUENCY	2 kHz	2.5 kHz
Q	200	780
RESONANCE GAIN	4.63	3.55
SYSTEM BANDWIDTH	5 Hz	3.2 Hz
SENSITIVITY	0.474 mV per rad/sec	0.288 mV per rad/sec
DRIVING VOLTAGE	20 V	20 V
FLEXURE THICKNESS	0.61 microns	0.48, 0.95 microns
% MAX PRINC. STRESS	0.19%	0.15%
RMS NOISE	0.5 microvolts	31 microvolts
ERROR RATE	218 deg/hr (predicted)	22,000 deg/hr (demonstrated)
GYRO TORQUE	1.3 E-4 dyne-micron	8.2 E-6 dyne-micron
STABILITY RATIO	0.91	0.007
SENSOR CAPACITANCE	9.3 E-15 farads	1.8 E-14 farads

Table 6.1

CHARACTERISTICS OF PREVIOUSLY DEVELOPED
TUNING FORK GYROSCOPES

	SPERRY GYROTRON	WATSON ARS
CONFIGURATION	single gimbal, open fork	no gimbal, open fork
MOTOR	electrostatic plates (linear)	piezoelectric beams
SENSOR	electromagnetic pickoffs	piezoelectric beams
INPUT AXIS	in-plane, fork stem	in-plane, fork stem
MATERIAL	machined 1% carbon steel	solid state
PACKAGING	controlled damping vanes	solid state packaging, air
SIZE	1.58 E-3 m^3	6.27 E-5 m^3
MASS	7.0 kg	0.11 kg
POWER	0.5 W	0.6 W
FREQUENCY	940 Hz	360 Hz
Q	variable	not specified
RESONANCE GAIN	tuned to resonance	tuned to resonance
SYSTEM BANDWIDTH	11.76 Hz (closed loop)	50 Hz (closed loop)
SENSITIVITY	433.16 mV per rad/sec	19.1 V per rad/sec
MAX RMS NOISE	50 microvolts	15 millivolts
DRIVING VOLTAGE	unspecified	unspecified
ERROR RATE	23.8 deg/hr	162 deg/hr
STABILITY RATIO	none indicated	none indicated

Table 6.2

REFERENCES

[1]   Boxenhorn, B. , *The Micromechanical Planar Gyroscope Summary Report* , Fiscal 83-84, IR&D Project #193, Publication CSDL-D-5734, 1984.

[2]   Boxenhorn, B. & Greiff, P. ," A Vibratory Micromechanical Gyroscope ", *AIAA Guidance, Navigation, & Control Conference*, Minneapolis, MN, Aug. 1988.

[3]   Barnaby, R.E., Chatterton, J.B., Gerring, F.H. , " General Theory and Operational Characteristics of the Gyrotron Angular Rate Tachometer" , *Aeronautical Engineering Review,* Nov. 1953.

[4]   Hunt, G., & Hobbs, O. , " Development of an Accurate Tuning Fork Gyroscope", *Proceedings of Instrumentation and Mechanical Engr. ,*Vol. 179, Pt 3E, 1964.

[5]   Fearnside, K., & Briggs, B. , " The Mathematical Theory of Vibratory Angular Rate Tachometers", *The Institute of Electrical Engineering,* Monograph No. 264M, Nov. 1957.

[6]   Lyman, J. , " A New Space Rate Rate Sensing Instrument" , *Aeronautical Engineering Review,* Nov. 1953.

[7]   Roark, R.J. & Young, W.C., *Formulas for Stress and Strain,* McGraw-Hill Book Co, New York, 1975,

[8]   Lang, H.L, & Bart, S.F. , " Toward the Design of Successful Electric Mocromotors", *Proceedings of the IEEE Workshop on Microrobots and Teleoperators,* 1988.

[9]   Thomson, W. T., *Theory of Vibration with Applications,* Prentice-Hall, Inc. , Englewood Cliffs, NJ, 1981.

[10]   Crandall, S., Karnopp, D., Kurtz, E., & Pridmore-Brown, D., *Dynamics of Mechanical and Electromechanical Systems,* D. E. Krueger Publishing Company, New York, 1984.

[11]   Richards, J.A., *Analysis of Periodically Time-Varying Systems* , Springer-Verlag, New York, 1983.

[12]   McLachlan, W., *Theory & Application of Mathieu Functions* , Clarendom Press, Oxford, 1947.

[13]   Porter, B., *Stability Criteria of Linear Dynamical Systems* , Oliver & Boyd, London, 1967.

[14]   Battin, R.H. , *An Introduction to the Mathematics and Methods of Astrodynamics* , AIAA Education Series, 1987.

[15]   Smythe, W.R., *Static & Dynamic Electricity* , McGraw-Hill Book Co., New York, 1968.

[16]   Gibbs, W.J., *Conformal Transformations in Electrical Engineering* , Chapman & Hall, London, 1958.

[17]   Bowman, F., *Introduction to Elliptic Functions with Applications* , Dover, New York, 1961.

[18]   Churchill, R.V., *Operational Mathematics* , McGraw-Hill Book Co., 1972.

[19]   Press, W.H., Flannery, B.P., Teukolsky, S.A., & Vetterling, W.T., *Numerical Recipes - The Art of Scientific Computing* , Cambridge University Press, New York, 1986.

[20]   Shigley, J.E., & Mitchell, L.D., *Mechanical Engineering Design* , McGraw-Hill Book Co., New York, 1983.

[21]   Timoshenko, S.P., & Goodier, J.N., *Theory of Elasticity* , McGraw-Hill Book Co., New York, 1970.

[22]   Kaminsky, G., " Micromachining of Silicon Mechanical Structures ", *Journal of Vacuum Science Technology* , July/August 1985.

[23]   Peterson, K.E., " Silicon as a Mechanical Material ", *Proceedings of the IEEE* , Vol. 70, No. 5, May 1982.

[24]   Connally, J.A., " Torsion of a Thin Rectangular Beam with Axial Prestress and Ends Constrained from Warping " , Master of Science in Mechanical Engineering Thesis, MIT, 1987.

[25]   Wolf, H. , *Silicon Semiconductor Technology* , John Wiley & Sons, Inc., New York, 1971.

[26]   Potter, M.C. , & Foss, J.F., *Fluid Mechanics* , Great Lakes Press, Inc., Okemos, MI , 1982.

[27]   Happel, J., *Low Reynold's Number Hydrodynamics with Special Applications to Particulate Media* , Prentice-Hall, Englewood Cliffs, NJ, 1965.

[28]   Brown, R.G., *Random Signal Analysis and Kalman Filtering* , John Wiley & Sons, Inc., New York, 1983.

[29]   Newton, G., " Comparison of Vibratory & Rotating Wheel Gyroscopic Rate Indicators ", *Proceedings of the AIEE*, July 1960.

[30]   Terry, S., Angell, J., & Barth, P., " Silicon Micromechanical Devices ", *Scientific American* , April 1983.

[31]   Findlay, W., & Watt, D., *PASCAL: An Introduction to Methodical Programming*, Computer Science Press, Inc., Rockville, MD, 1978.

[32]   Morrow, C.T., " Zero Signals in the Sperry Tuning Fork Gyrotron ", *Journal of the Acoustical Society of America* , Vol. 27, No. 3, May 1955.

[33]   Ogata, K., *Modern Control Engineering* , Prentice-Hall ,Inc., Englewood Cliffs, NJ, 1970.

APPENDIX

```pascal
[$N+}                    (Enable 8087 coprocessor)
[$I+}                    (Turn on user interrupt)

program simulation;

(This is a PASCAL program which uses fourth order Runge-Kutta integration
 with error monitored adaptive step size that solves the tuning fork gyro
 periodically forced time-variant equation of motion.  The second order
 differential equation used assumes a tuned device so that the driving
 frequency is equal to the torsional resonant frequency.  The oscillatory
 output is calculated,and values greater than a specified transient time
 are stored and printed in tabular and graphical form.  The system
 parameters are inputted interactively.)

CONST
      n = 2;                         (# of states)
      nstep = 200;                   (max # of stored steps)

TYPE
      glnarray = ARRAY[1..n] of DOUBLE;      (dep. variable array)
      glarray  = glnarray;

VAR
      xp   : ARRAY[1..nstep] of DOUBLE;
      ystart,dydx,yout: glnarray;
      yp : ARRAY[1..n,1..nstep] of DOUBLE;
      wo,Q,ep,rate: DOUBLE;                  (gyro inputted parameters)
      x1,x2,xtrans: DOUBLE;
      thmax,per,nper,ypmax,ratio: DOUBLE;
      eps,h1,hmin,dxsav: DOUBLE;             (adaptive algorithm parameters)
      i,kmax,kount,nbad,nok:INTEGER;         (counters)

(-------------------------------------------------------------------------)
                                   (this procedure defines the system
                                    parameters)


PROCEDURE start;
      Begin
        writeln('input drive frequency in rad/sec');
        readln(wo);
        writeln('input ep, inertia ratio times drive angle in rad');
        readln(ep);
        writeln('input quality factor, Q');
        readln(Q);
        writeln('input applied rate in rad/sec');
        readln(rate);
        writeln('input # of periods for stored values');
        readln(nper);
        writeln('input allowed transient time in seconds');
        readln(xtrans);
      End;

(-------------------------------------------------------------------------)
                                   (this procedure defines the state
                                    space equations integrated by RK4)
```

128

```
PROCEDURE derivs(x:double; y:glnarray;
                 VAR    dydx:glnarray);

    Begin
        dydx[1] := y[2];
        dydx[2] := ((-wo/Q -ep*wo*COS(wo*x))*y[2] -wo*wo*y[1]
                    -rate*ep*wo*COS(wo*x))/(1+ep*SIN(wo*x));
    End;
```

<-->
                                (this procedure computes the numerical
                                 integration using 4th order Runge-Kutta
                                 (rk4) and the given state equations
                                 (derivs) for a given step size.)

```
PROCEDURE rk4(y,dydx: glnarray; n: integer; x,h: real; VAR yout: glnarray);

VAR
    i: integer;
    xh,hh,h6: real;
    dym,dyt,yt: glnarray;

BEGIN
    hh := h*0.5;
    h6 := h/6.0;
    xh := x+hh;
    FOR i := 1 to n DO BEGIN
        yt[i] := y[i]+hh*dydx[i]              (first Euler step @ midpoint)
    END;
    derivs(xh,yt,dyt);
    FOR i := 1 to n DO BEGIN
        yt[i] := y[i]+hh*dyt[i]               (2nd Euler step @ midpoint w/ new deriv.)
    END;
    derivs(xh,yt,dym);
    FOR i := 1 to n DO BEGIN                  (Euler step @ endpoint)
        yt[i] := y[i]+h*dym[i];
        dym[i] := dyt[i]+dym[i]
    END;
    derivs(x+h,yt,dyt);
    FOR i := 1 to n DO BEGIN                  (final integr. estimate over interval
                                               from Runge-Kutta algorithm)

        yout[i] := y[i]+h6*(dydx[i]+dyt[i]+2.0*dym[i])
    END
END;
```

<-->
                                (This Procedure calculates the stepsize
                                 bounded by the error criterion given a trial
                                 value and the current values of the
                                 arrays)

```
PROCEDURE rkqc(VAR y,dydx: glarray; n: integer; VAR x: real;
```

```pascal
                htry,eps: real; yscal: glarray; VAR hdid,hnext: real);
LABEL 1;
CONST
    pgrow=-0.20;                         ( exp. if desired accuracy < calculated )
    pshrnk=-0.25;                        ( exp. if desired accuracy > calculated )
    fcor=0.06666666;                     ( 1.0/15.0 )
    one=1.0;
    safety=0.9;
    errcon=6.0e-4;                       ( 4/safety  *  1/pgrow )
VAR
    i: integer;
    xsav,hh,h,temp,errmax: real;
    dysav,ysav,ytemp: glarray;
BEGIN
    xsav := x;                           ( save initial values )
    FOR i := 1 to n DO BEGIN
        ysav[i] := y[i];
        dysav[i] := dydx[i]
    END;
    h := htry;                           ( initialize stepsize @ trial value )
1:  hh := 0.5*h;                         ( take 2 half steps and comp. num. estimate )
    rk4(ysav,dysav,n,xsav,hh,ytemp);
    x := xsav+hh;
    derivs(x,ytemp,dydx);
    rk4(ytemp,dydx,n,x,hh,y);            ( take 1 large step and comp. num. estimate )
    x := xsav+h;
    IF (x = xsav) THEN BEGIN             ( check that stepsize is not infinitesimal )
        writeln('pause in routine RKQC');
        writeln('stepsize too small'); readln
    END;
    rk4(ysav,dysav,n,xsav,h,ytemp);
    errmax := 0.0;
    FOR i := 1 to n DO BEGIN             ( truncation error is comparison of 2 estims.)
        ytemp[i] := y[i]-ytemp[i];
                                         ( error is scaled by estimated output value )
        temp := abs(ytemp[i]/yscal[i]);
        IF (errmax < temp) THEN errmax := temp
    END;
    errmax := errmax/eps;                ( error relative to tolerance, eps )
    IF (errmax > one) THEN BEGIN ( too large - shrink stepsize )
        h := safety*h*exp(pshrnk*ln(errmax));
        GOTO 1 END                       ( try again with new stepsize )
    ELSE BEGIN
        hdid := h;
        IF (errmax > errcon) THEN BEGIN
                                         ( error below tolerance - increase stepsize )
            hnext := safety*h*exp(pgrow*ln(errmax))
        END ELSE BEGIN
            hnext := 4.0*h
        END
    END;
    FOR i := 1 to n DO BEGIN             ( add fifth order truncation error )
        y[i] := y[i]+ytemp[i]*fcor
    END
END;
```

```
(---------------------------------------------------------------------)
                                       ( This procedure steps the numerical
                                         integration storing values of the
                                         output array as specified  )


PROCEDURE odeint(VAR ystart: glnarray; nvar: integer;
        x1,x2,eps,h1,hmin: real; VAR nok,nbad: integer);
LABEL 99;
CONST
   maxstp=10000;                        ( max allowable steps for computer time )
   two=2.0;
   zero=0.0;
   tiny=1.0e-30;
VAR
   nstp,i: integer;
   xsav,x,hnext,hdid,h: real;
   yscal,y,dydx: glnarray;
BEGIN
   x := x1;                             ( initialize time variable )
   IF (x2 > x1) THEN h := abs(h1) ELSE h := -abs(h1);
   nok := 0;                            ( initialize counters )
   nbad := 0;
   kount := 0;
   FOR i := 1 to nvar DO BEGIN
      y[i] := ystart[i]
   END;
   xsav := x-dxsav*two;
   FOR nstp := 1 to maxstp DO BEGIN
      derivs(x,y,dydx);
      FOR i := 1 to nvar DO BEGIN
                                        ( estim. output val. used to scale error )
         yscal[i] := abs(y[i])+abs(dydx[i]*h)+tiny
      END;
      IF (x > xtrans) THEN BEGIN ( only store after transient )
                                        ( only store if interval>dxsav )
         IF (abs(x-xsav) > abs(dxsav)) THEN BEGIN
                                        ( only store if #steps < kmax )
            IF (kount < kmax-1) THEN BEGIN
               kount := kount+1;
               xp[kount] := x;
               FOR i := 1 to nvar DO BEGIN
                  yp[i,kount] := y[i]
               END;
               xsav := x
            END
         END
      END;
                                        ( if remaining time < stepsize )
      IF (((x+h-x2)*(x+h-x1)) > zero) THEN h := x2-x;
      rkqc(y,dydx,nvar,x,h,eps,yscal,hdid,hnext);
      IF (hdid = h) THEN BEGIN  ( count successful steps )
         nok := nok+1
```

```
      END ELSE BEGIN
         nbad := nbad+1                    ( count retried steps )
      END;
                                          ( check if integration interval completed )
      IF (((x-x2)*(x2-x1)) >= zero) THEN BEGIN
         FOR i := 1 to nvar DO BEGIN
            ystart[i] := y[i]
         END;
         IF (kmax <> 0) THEN BEGIN
            kount := kount+1;
            xp[kount] := x;                ( save final step )
            FOR i := 1 to nvar DO BEGIN
               yp[i,kount] := y[i]
            END
         END;
         GOTO 99                           ( go to end )
      END;
      h := hnext;                          ( return stepsize )
   END;
99:   END;


(----------------------------------------------------------------)
                                ( This procedure writes the system parameters
                                  and tabulated stored output angles to the
                                  file OUTPT )

PROCEDURE writeout;

   VAR
       outpt: TEXT;
        i,j: INTEGER;
   Begin
      assign(outpt,'prn');
      rewrite(outpt);
      writeln(outpt,'                              TUNING FORK MICROGYRO SIMULATION
RESULTS ');
      writeln(outpt);
      writeln(outpt);
      writeln(outpt,'                  Inputted Parameter Values');
      writeln(outpt,'                  --------------------------');
      writeln(outpt,'           w = ',wo:9:4,' rad/sec ','     Q = ',Q:9:2,
                  ' ep*Q = ',ep*Q:8:2);
      writeln(outpt,'input rate = ',rate:9:2,' rad/sec','     ep  = ',ep:9:6);
      writeln(outpt,'       nper = ',nper:9:2,'           ',' xtrans = ',
                  xtrans:9:2,' seconds');
      writeln(outpt);

      writeln(outpt,'  time (sec)','           ','output angle (rad)',
                  '  angular velocity (rad/sec)');
      writeln(outpt,'  ----------','        ','------------------',
                  '  ------------------------');
      writeln(outpt);
      for i := 1 to kount do
        begin
           writeln(outpt,xp[i]:12:6,'           ',yp[1,i]:14:6,'
```

132

```
,yp[2,i]:16:6);
      end;
    writeln(outpt);
    writeln(outpt,' estimated max output angle = ',thmax:14:6,' radians');
    writeln(outpt,'period of each output cycle = ',per:14:5,' seconds');
    writeln(outpt,'  # of successful steps     = ',nok:14);
    writeln(outpt,'        # of bad steps       = ',nbad:14);
    writeln(outpt,' simulated max output angle = ',ypmax:14:6,' radians');
    writeln(outpt,' ratio simulated/estimated  = ',ratio:14:5);
    writeln(outpt);
    close(outpt);
  End;


-----------------------------------------------------------------}


  BEGIN              (Main Program)

    ystart[1] := 0.0;                    (initial values)
    ystart[2] := 0.0;

    start;                               (input parameters)

    per := 6.28/wo;                      (cycle period)
    x1 := 0.0;                           (start at time zero)
    x2 := nper*per+xtrans;               (integrate until inputted transient plus
                                          desired number of stored periods)

    thmax := Q*ep*rate/wo;               (predicted maximum output angle)

    dxsav := (x2-xtrans)/(20.0*nper);    (store 20 values per period)
    eps := 1.0e-3;                       (comp. values accurate within 0.1%)
    kmax := 120;                         (max # of values that can be stored)
    hmin := 0.0;                         (minimum allowable stepsize)
    h1 := per/15;                        (initial stepsize 15 per period)

    odeint(ystart,n,x1,x2,eps,h1,hmin,nok,nbad);  (drive num. integration)
    ypmax := ABS(yp[1,1]);               (scan stored output for max)

    FOR i := 2 to kount DO BEGIN
        IF(ABS(yp[1,i]) > ABS(ypmax)) THEN ypmax:=ABS(yp[1,i]);
    END;
    ratio := ypmax/thmax;
    writeout;

  END.              (Main Program)
```

TUNING FORK MICROGYRO SIMULATION RESULTS

Inputted Parameter Values
----

w = 6280.0000 rad/sec   Q =   200.00 ep*Q =   16.00

input rate =   1.00 rad/sec   ep =   0.080000

nper =   4.00   xtrans =   0.60 seconds

time (sec)	output angle (rad)	angular velocity (rad/sec)
0.600073	0.002091	-7.883974
0.600161	0.001106	-13.806398
0.600260	-0.000363	-14.742356
0.600352	-0.001552	-10.611256
0.600443	-0.002218	-3.653795
0.600547	-0.002147	4.929047
0.600640	-0.001376	11.206867
0.600735	-0.000129	14.400010
0.600824	0.001136	13.219787
0.600916	0.002113	7.474279
0.601009	0.002402	-1.552215
0.601105	0.001803	-10.453149
0.601194	0.000639	-14.819492
0.601289	-0.000770	-13.894013
0.601378	-0.001805	-8.825099
0.601477	-0.002293	-0.874646
0.601565	-0.002051	6.246314
0.601653	-0.001236	11.830887
0.601750	0.000074	14.506721
0.601837	0.001296	12.701519
0.601927	0.002187	6.565329
0.602020	0.002378	-2.699352
0.602115	0.001695	-11.178645
0.602206	0.000463	-15.014945
0.602301	-0.000919	-13.454859
0.602389	-0.001890	-8.088356
0.602490	-0.002297	0.206513
0.602576	-0.001976	7.077917
0.602663	-0.001117	12.294250
0.602762	0.000239	14.515240
0.602851	0.001454	12.078335
0.602941	0.002267	5.346603
0.603035	0.002328	-4.160377
0.603129	0.001544	-12.038132
0.603222	0.000233	-15.131368
0.603315	-0.001106	-12.793577
0.603402	-0.001988	-7.098503
0.603508	-0.002282	1.613911
0.603606	-0.001739	9.091112
0.603696	-0.000705	13.515865
0.603799	0.000765	14.054310
0.603898	0.001951	9.052120
0.603990	0.002412	0.569516
0.604000	0.002412	-0.494348

estimated max output angle =   0.002548 radians
period of each output cycle =   0.00100 seconds
    # of successful steps   =   5461
       # of bad steps   =   1061
simulated max output angle =   0.002412 radians

TUNING FORK MICROGYRO SIMULATION RESULTS

Inputted Parameter Values
----

w = 6280.0000 rad/sec   Q =   200.00 ep*Q =   4.00

put rate =   1.00 rad/sec   ep = 0.020000

nper =   4.00   xtrans =   0.60 seconds

time (sec)	output angle (rad)	angular velocity (rad/sec)
0.600088	0.000627	-0.954790
0.600182	0.000432	-3.022520
0.600275	0.000099	-3.989034
0.600374	-0.000289	-3.556727
0.600465	-0.000548	-2.022114
0.600564	-0.000634	0.325526
0.600662	-0.000490	2.532851
0.600750	-0.000203	3.790011
0.600853	0.000203	3.839891
0.600948	0.000512	2.478833
0.601041	0.000644	0.264849
0.601129	0.000568	-1.933476
0.601217	0.000321	-3.523502
0.601315	-0.000060	-3.999616
0.601411	-0.000410	-3.045972
0.601501	-0.000605	-1.222964
0.601605	-0.000601	1.302022
0.601699	-0.000385	3.172200
0.601793	-0.000035	4.012027
0.601881	0.000304	3.577275
0.601969	0.000559	2.042057
0.602065	0.000643	-0.340796
0.602162	0.000494	-2.623704
0.602250	0.000199	-3.851034
0.602352	-0.000205	-3.788681
0.602446	-0.000503	-2.429728
0.602541	-0.000635	-0.249349
0.602629	-0.000564	1.839262
0.602717	-0.000326	3.423731
0.602815	0.000047	4.017464
0.602902	0.000377	3.299185
0.602990	0.000596	1.557704
0.603089	0.000627	-0.954794
0.603184	0.000432	-3.022532
0.603276	0.000099	-3.989050
0.603376	-0.000289	-3.556740
0.603466	-0.000548	-2.022122
0.603565	-0.000634	0.325527
0.603663	-0.000490	2.532860
0.603752	-0.000203	3.790025
0.603855	0.000203	3.839906
0.603949	0.000512	2.478843
0.604000	0.000610	1.333530

stimated max output angle =   0.000637 radians
riod of each output cycle =   0.00100 seconds
# of successful steps   =   5640
    # of bad steps   =   812
imulated max output angle =   0.000644 radians
atio simulated/estimated =   1.01054

TUNING FORK MICROGYRO SIMULATION RESULTS

Inputted Parameter Values
----

w = 6280.0000 rad/sec		Q =	200.00	ep*Q =	1.00
nput rate =	1.00 rad/sec	ep =	0.005000		
nper =	4.00	xtrans =	0.60 seconds		

time (sec)	output angle (rad)	angular velocity (rad/sec)
0.600047	0.000160	0.047323
0.600134	0.000141	-0.486915
0.600222	0.000079	-0.877212
0.600320	-0.000016	-1.000792
0.600417	-0.000104	-0.761647
0.600506	-0.000153	-0.299180
0.600610	-0.000150	0.342234
0.600704	-0.000095	0.808772
0.600799	-0.000006	1.005337
0.600886	0.000078	0.881311
0.600973	0.000140	0.495664
0.601071	0.000160	-0.101241
0.601168	0.000122	-0.659535
0.601257	0.000047	-0.962838
0.601360	-0.000055	-0.943603
0.601454	-0.000129	-0.592941
0.601549	-0.000160	-0.036354
0.601636	-0.000140	0.488220
0.601724	-0.000079	0.874454
0.601822	0.000016	1.001545
0.601919	0.000105	0.762074
0.602008	0.000153	0.295211
0.602111	0.000151	-0.348116
0.602205	0.000095	-0.815172
0.602300	0.000005	-1.005825
0.602387	-0.000078	-0.874823
0.602474	-0.000140	-0.489044
0.602573	-0.000159	0.107688
0.602670	-0.000121	0.659254
0.602759	-0.000046	0.961853
0.602863	0.000056	0.943964
0.602957	0.000130	0.589314
0.603051	0.000160	0.027827
0.603138	0.000139	-0.500638
0.603225	0.000077	-0.883193
0.603324	-0.000018	-0.999205
0.603421	-0.000106	-0.753023
0.603510	-0.000153	-0.284482
0.603614	-0.000150	0.354912
0.603707	-0.000093	0.815535
0.603803	-0.000004	1.005831
0.603889	0.000079	0.876112
0.603976	0.000140	0.488425
0.604000	0.000150	0.350944

estimated max output angle =	0.000159	radians
eriod of each output cycle =	0.00100	seconds
# of successful steps =	5507	
# of bad steps =	958	
simulated max output angle =	0.000160	radians
ratio simulated/estimated =	1.00754	